

Design of Gages for Direct Skin Friction Measurements in Complex Turbulent Flows with Shock Impingement Compensation

by

August J. Rolling

Dissertation submitted to the Faculty of the
Virginia Polytechnic Institute and State University
In partial fulfillment of the requirements for the degree of

Doctor of Philosophy
in
Aerospace Engineering

APPROVED:

Dr. Joseph A. Schetz, Chairman

Dr. William L. Hallauer

Lt Col Keith M. Boyer, PhD

Dr. Rakesh K. Kapania

Dr. Matthew MacLean

June 7, 2007
Blacksburg, VA

Keyword: skin friction, wall shear, shock impingement,
complex turbulent flow

Report Documentation Page

Form Approved
OMB No. 0704-0188

Public reporting burden for the collection of information is estimated to average 1 hour per response, including the time for reviewing instructions, searching existing data sources, gathering and maintaining the data needed, and completing and reviewing the collection of information. Send comments regarding this burden estimate or any other aspect of this collection of information, including suggestions for reducing this burden, to Washington Headquarters Services, Directorate for Information Operations and Reports, 1215 Jefferson Davis Highway, Suite 1204, Arlington VA 22202-4302. Respondents should be aware that notwithstanding any other provision of law, no person shall be subject to a penalty for failing to comply with a collection of information if it does not display a currently valid OMB control number.

1. REPORT DATE 31 JUL 2007		2. REPORT TYPE N/A		3. DATES COVERED -	
4. TITLE AND SUBTITLE Design of Gages for Direct Skin Friction Measurements in Complex Turbulent Flows with Shock Impingement Compensation				5a. CONTRACT NUMBER	
				5b. GRANT NUMBER	
				5c. PROGRAM ELEMENT NUMBER	
6. AUTHOR(S)				5d. PROJECT NUMBER	
				5e. TASK NUMBER	
				5f. WORK UNIT NUMBER	
7. PERFORMING ORGANIZATION NAME(S) AND ADDRESS(ES) Virginia Polytechnic Institute and State University				8. PERFORMING ORGANIZATION REPORT NUMBER	
9. SPONSORING/MONITORING AGENCY NAME(S) AND ADDRESS(ES) The Department of the Air Force AFIT/ENEL WPAFB, OH 45433				10. SPONSOR/MONITOR'S ACRONYM(S)	
				11. SPONSOR/MONITOR'S REPORT NUMBER(S) CI07-0062	
12. DISTRIBUTION/AVAILABILITY STATEMENT Approved for public release, distribution unlimited					
13. SUPPLEMENTARY NOTES					
14. ABSTRACT					
15. SUBJECT TERMS					
16. SECURITY CLASSIFICATION OF:			17. LIMITATION OF ABSTRACT	18. NUMBER OF PAGES	19a. NAME OF RESPONSIBLE PERSON
a. REPORT unclassified	b. ABSTRACT unclassified	c. THIS PAGE unclassified			

Design of Gages for Direct Skin Friction Measurements in Complex Turbulent Flows with Shock Impingement Compensation

August J. Rolling

Dr. Joseph A. Schetz, Chairman

Aerospace Engineering

Abstract

This research produced a new class of skin friction gages that measures wall shear even in shock environments. One test specimen separately measured wall shear and variable-pressure induced moment. Through the investigation of available computational modeling methods, techniques for accurately predicting gage physical responses were developed. The culmination of these model combinations was a design optimization procedure. This procedure was applied to three disparate test conditions: 1) short-duration, high-enthalpy testing, 2) blow-down testing, and 3) flight testing. The resulting optimized gage designs were virtually tested against each set of nominal load conditions. The finalized designs each successfully met their respective test condition constraints while maximizing strain output due to wall shear.

These gages limit sources of apparent strain: inertia, temperature gradient, and uniform pressure. A unique use of bellows provided a protective shroud for surface strain gages. Oil fill provided thermal and dynamic damping while eliminating uniform pressure as a source of output voltage. Two Wheatstone bridge configurations were developed to minimize temperature effects first from temperature gradient and then from spatially varying heat flux induced gradient. An inertia limiting technique was developed that parametrically investigated mass and center of gravity impact on strain output.

Multiple disciplinary computational simulations of thermal, dynamic, shear, moment, inertia, and instrumentation interaction were developed. Examinations of instrumentation error, settling time, filtering, multiple input dynamic response, and strain gage placement to avoid thermal gradient were conducted. Detailed mechanical drawings for several gages were produced for fabrication and future testing.

Acknowledgements

First of all I would like to thank God for this incredible opportunity! Thanks my family for helping see me through this three year adventure. Thanks Dr. Schetz for bringing me on board with such a great team. Your consistent leadership kept things moving at a fast pace I didn't previously think possible.

Thanks to each member of the scramjet team who made this work fun, especially the meetings! Special thanks goes to Luca for checking over my work, helping me on the tougher problems, and being the tiger-man.

I really appreciate the guys who put these gages together. Steve, James, and Bruce put together a concerted effort that produced professional quality gages. I also thank Alex Sang whose innovative use of bellows and oil fill techniques were key.

I would like to thank my committee members who were selected because of their contributions to this effort. Dr. Hallauer helped me work through several subjects including dynamic response and Wheatstone bridge design. Dr. Matthew MacLean and Dr. Holden at LENS provided needed support and timely information on facility requirements. Dr. Kapania helped with finite element modeling and thermal strain. And of course Lt Col Boyer gave me the necessary motivation to complete this research to become part of the renowned propulsion mafia.

The views expressed in this article are those of the author and do not reflect the official policy or position of the United States Air Force, Department of Defense, or the U.S. Government.

Contents	
Abstract	i
Acknowledgements	iii
List of Figures	vi
List of Tables	ix
Nomenclature	x
1 Introduction/Motivation	1
1.1 Scramjet Performance	2
1.2 Estimating Skin Friction	7
1.3 Measuring Skin Friction	9
1.4 Skin Friction Gage Design	11
2 Theoretical Approach	16
2.1 2-D Steady Flow Model	16
2.2 Cantilever Beam Gage Model	17
2.3 Ideal Wheatstone Bridge Model	20
2.4 Ideal Simulation	21
3 Separately Measure τ_w and M_o	25
3.1 CF1 Gage Design	25
3.2 CF1 Results	28
3.2.1 CF1 Calibration	28
3.2.2 CF1 Virginia Tech Supersonic Tunnel Wall Shear Test	31
3.2.3 CF1 Post Experiment Investigation	32
3.3 CF2 Gage Design	36
3.4 CF2 Results	37
3.4.1 CF2 Calibration	38
3.4.2 CF2 Virginia Tech Supersonic Tunnel Wall Shear Test	43
3.4.3 CF2 Virginia Tech Supersonic Tunnel Shock Impingement Test	46
4 Gage Characterization	49
4.1 Model Results	49
4.2 Static Response	51
4.2.1 Static Wall Shear	52
4.2.2 Static Moment	54
4.2.3 Inertia Loading	55
4.2.4 Static Pressure	55
4.3 Dynamic Response	56
4.3.1 Vibrational Frequency	56
4.3.2 Step Load	58
4.4 Thermal Response	60
4.5 Combined Response	63
4.6 Gage Characterization Techniques	65
5 Optimization	68
5.1 Optimization for Short Duration High Enthalpy Testing	69
5.1.1 CF3 Gage Design	69
5.1.2 CF4 Gage Design	81
5.2 Optimization for Blow Down Facility Testing	84
5.3 Optimization for a Typical Flight Test	86

5.4	Optimization Summary	87
6	Simulations	88
6.1	Instrumentation	88
6.2	Dynamic Response.....	89
6.2.1	Minimum Natural Frequency.....	90
6.2.2	Filter Setting.....	90
6.2.3	Gage Reaction to Heaviside load.....	91
6.2.4	Base Acceleration Response.....	93
6.3	Thermal response	96
6.3.1	Step Temperature Boundary Condition	96
6.3.2	Step Heat Flux Boundary Condition.....	97
6.3.3	Thermal Distribution 2-D FDM.....	101
6.3.4	2D FDM Result with Instrumentation Error.....	102
6.3.5	Thermal Distribution Axisymmetric FEM $\dot{q}_w(t)$	103
6.3.6	Thermal Distribution 3-D $\dot{q}_w(x,t)$	104
7	Conclusions and Recommendations	107
7.1	Short-term recommendations.....	110
7.2	Mid-term recommendations.....	111
7.3	Long-term recommendations	112
	References.....	113
	Appendix A	115

List of Figures

Figure 1-1. Shadowgraph in Virginia Tech’s supersonic tunnel with Mach 4 nozzle.....	1
Figure 1-2. Scramjet cross-section.....	2
Figure 1-3. Flight regimes of various propulsion systems burning H2.	3
Figure 1-4. NASA’s Aerospace Plane concept art.....	4
Figure 1-5. Dynamic pressure profile through typical scramjet engine.....	5
Figure 1-6. Scramjet engine design matrix and T-s diagram: 1) Ideal 2) Low drag 3) High drag.	6
Figure 1-7. Boundary layer profile Virginia Tech supersonic tunnel.	7
Figure 1-8. Skin Friction measurement technique classification hierarchy.....	10
Figure 1-9. Idealized skin friction gage cut-away.	11
Figure 1-10. Assembly of oil-filled bellows skin friction gage.	12
Figure 1-11. Skin friction gages from this research to scale.....	13
Figure 2-1. Cut-away view of tunnel test section with flow-field coordinate system.	16
Figure 2-2. 2-D shock impingement diagram.	17
Figure 2-3. Cantilever beam with surface flow loads.	18
Figure 2-4. Load configuration for simple cantilever beam.	20
Figure 2-5. First order simulation of load, gage, and measurement interaction.	21
Figure 2-6. Theoretical output: uniform pressure and 1-D temperature distribution.	22
Figure 2-7. Thermal distribution where temperature varies through beam thickness.	23
Figure 2-8. Two full Wheatstone bridge thermal compensation configuration.....	24
Figure 3-1. Strain and frequency as a function of material and cross-section.	26
Figure 3-2. CF1 frequency sweep as a function of beam cross section.....	27
Figure 3-3. Static wall shear calibration technique.....	29
Figure 3-4. CF1 static wall shear calibration results.....	30
Figure 3-5. Static moment calibration technique.....	30
Figure 3-6. CF1 static moment calibration.	31
Figure 3-7. Virginia Tech supersonic tunnel diagram.	32
Figure 3-8. Vacuum test technique.	33
Figure 3-9. CF1 post experiment vacuum test.	34
Figure 3-10. CF1 post experiment thermal test.	35
Figure 3-11. CF1 wire truss stiffening.....	36
Figure 3-12. CF2 baseline static wall shear calibration setup.	38
Figure 3-13. CF2 static wall shear calibration results.....	39
Figure 3-14. CF2 baseline static moment calibration setup.....	39
Figure 3-15. CF2 static moment calibration results.....	40
Figure 3-16. CF2 vacuum test calibration.....	41
Figure 3-17. Dynamic response calibration setup.....	42
Figure 3-18. String test calibration data. Top row shows calculated ω_n and ζ . Bottom row shows measured rise and settling times for +10% load.....	42
Figure 3-19. Pure wall shear results voltage output vs. time.	44
Figure 3-20. Comparison of CF2 head voltage and static temperature during M4 run.	45
Figure 3-21. CF2 pure wall shear bound solution.....	46
Figure 3-22. CF2 shock validation shadowgraph.	46
Figure 3-23. CF2 shock validation voltage output versus time.	47

Figure 3-24. CF2 bound shock impingement solution.....	48
Figure 4-1. Geometric parameters.	50
Figure 4-2. CF2 3-D FEM result for 2000 Pa wall shear.....	53
Figure 4-3. CF2 3-D FEM result for impinging Mach 10 normal shock.....	54
Figure 4-4. Calculation for equivalent inertial shear.	55
Figure 4-5. CF2 step load response. Comparison between calibration data and transformation solutions.....	59
Figure 4-6. Dynamic response to step load.....	60
Figure 4-7. 5% spatially varying heat flux, nominal 100 kW/m ²	61
Figure 4-8. Temperature distribution 100 kW/m ² for 0.1 s.	62
Figure 4-9. Strain magnitudes due to nominal wall shear.	63
Figure 4-10. Expected output for nominal conditions.	64
Figure 5-1. Thermal analysis for temperature gradient at LENS. FEM using 100 kW/m ² for 0.1 s.	69
Figure 5-2. CF3 geometrically constrained design space.	72
Figure 5-3. 8.5 ms settling time for 1000 Hz gage for 10 ms test run.	73
Figure 5-4. CF3 first mode natural frequency.	76
Figure 5-5. CF3 strain output due to 1000 Pa wall shear.....	77
Figure 5-6. CF3 displacement due to 2000 Pa load.....	78
Figure 5-7. CF3 equivalent acceleration shear.	79
Figure 5-8. CF3 state variable constraints on design space.....	80
Figure 5-9. CF3 fully constrained design space with expected strain output.	80
Figure 5-10. CF4 frequency impact on design space, aluminum vs. invar.....	82
Figure 5-11. CF4 strain response to wall shear.....	82
Figure 5-12. CF4 equivalent acceleration shear as percentage of wall shear.	83
Figure 5-13. CF4 constrained design space.	84
Figure 5-14. Blow down facility constraints on design space.	85
Figure 5-15. Blow down facility expected wall shear strain output.	85
Figure 5-16 Flight test constraints on design space.	86
Figure 5-17 Flight condition expected wall shear strain output.	86
Figure 5-18. Optimization overview.....	87
Figure 6-1. Expected signal output using several cut-off frequencies.....	90
Figure 6-2. Heaviside approximation to Virginia Tech time varying wall shear.	91
Figure 6-3. Simulation of Virginia Tech pure wall shear case.	92
Figure 6-4. Acceleration, velocity, and displacement of base in LENS.	93
Figure 6-5. 1-D kinetics diagram.	93
Figure 6-6. Simulated 1-D gage response to multiple inputs.....	95
Figure 6-7. Gaussian analytic and 1-D FTCS thermal step solution at 9.0 s.....	97
Figure 6-8. Gaussian analytic and 1-D FTCS heat flux step solution at 9.0 s.....	98
Figure 6-9. Heat flux development for Virginia Tech supersonic tunnel using thermocouple data.	99
Figure 6-10. Validation of Axisymmetric FEM and approximated heat flux.....	100
Figure 6-11. Load deck for Virginia Tech supersonic tunnel.....	101
Figure 6-12. 2-D FDM temperature distribution.	102
Figure 6-13. Thermal investigation of strain gage offset.....	103
Figure 6-14. Axisymmetric FEM temperature distribution.	104

Figure 6-15. Time and space varying heat flux for Virginia Tech supersonic tunnel pure wall shear.	105
Figure 6-16. Planar slices of 3-D FEM.	105
Figure 6-17. 3-D FEM time and space varying heat flux.	106
Figure 7-1. Expected strain output due to nominal load conditions.	108
Figure 7-2. Design drivers and effective design space.	110

List of Tables

Table 1-1. Engine performance parameters for 3 air-breathing engines burning H ₂ .	4
Table 1-2. Performance parameters for 3 scramjet engines.	6
Table 1-3. Estimates for the Virginia Tech supersonic tunnel.	8
Table 1-4. Nominal design specifications.	13
Table 2-1. 2-D steady flow conditions.	17
Table 2-2. Strain distributions for typical beam loads.	19
Table 3-1. CF1 design approach.	26
Table 3-2. CF1 gage in stages.	28
Table 3-3. CF2 state variables, objective functions, and design variables.	37
Table 3-4. CF2 gage in stages.	37
Table 3-5. CF2 vibration frequency calibration results.	43
Table 4-1. CF1, CF2, CF3, and CF4 expected output to nominal loading.	49
Table 4-2. Geometric quick reference.	50
Table 4-3. Structural material properties reference.	50
Table 4-4. Thermal material properties reference.	51
Table 4-5. Solid mechanics equations.	51
Table 4-6. Gage components and instrumentation.	51
Table 4-7. Cantilever beam static load solutions.	52
Table 4-8. Expected CF2 output to 200 Pa wall shear.	53
Table 4-9. Expected CF2 output to a Mach 10 normal shock.	54
Table 4-10. Cantilever beam solution for 1 st mode bending response.	57
Table 4-11. Comparison of several FEMs to cantilever theory for 1 st mode bending.	57
Table 4-12. Natural frequency output for each gage.	58
Table 4-13. CF2 Validation data.	60
Table 4-14. Expected strain output at ‘head’ due to nominal heat flux.	62
Table 4-15. Nominal design loads.	63
Table 4-16. Relative magnitude of strain output.	64
Table 4-17. Output measurements to nominal load case.	65
Table 4-18. Accelerometer employment with direct measure gages.	65
Table 4-19. Gage characterization summary.	66
Table 5-1. Test regimes for gage optimization.	68
Table 5-2. Design feature impact on size. Comparison between CF2 and CF3.	70
Table 5-3. Test conditions for consideration for CF3.	71
Table 5-4. CF3 design variable constraints.	71
Table 5-5. CF3 constrained state variables.	75
Table 6-1. Instrumentation error sources.	88
Table 6-2. Thermal step equations.	97
Table 6-3. Analytic solution for sudden heat flux.	98
Table 7-1. Optimized design space for INVAR gages.	109
Table 7-2. Gages currently being fabricated.	111

Nomenclature

A	= area
a	= acceleration
C_f	= skin friction coefficient
CF	= skin friction gage
CTE	= coefficient of thermal expansion
c	= coefficient of viscous damping
cp	= specific heat
cg	= center of gravity
E	= modulus of elasticity
e	= voltage
erf	= Gaussian error function
FDM	= finite difference model
FEM	= finite element model
f	= frequency
F/\dot{m}_o	= specific thrust
GF	= gauge factor (strain gauge)
I	= moment of inertia
Isp	= specific impulse
k	= thermal conductivity
k	= spring constant
L	= Length
M	= Mach number
M_o	= moment
m	= mass
NS	= normal shock
P	= pressure force (equivalent axial point load)
\dot{q}	= heat flux
q	= dynamic pressure
r	= radius
R	= resistance
S	= thrust specific fuel consumption
S(t)	= wall shear forcing function
s	= Laplace transform domain variable
T	= temperature
t	= time
th	= thickness
u	= displacement
V	= velocity
V_o	= output voltage
V_{in}	= input voltage
w	= width
x	= Cartesian mean flow direction

y = Cartesian vertical up
z = Cartesian spanwise perpendicular

Greek

α = thermal diffusivity
 γ = ratio of specific heats
 δ = beam displacement
 δ = wedge angle
 ε = strain
 ζ = damping coefficient
 η_o = overall efficiency
 η_p = propulsive efficiency
 η_{th} = thermal efficiency
 θ_i = shock incidence angle
 θ_r = shock reflected angle
 λ = Eigen value first mode bending
 μ = laminar coefficient of viscosity
 $\mu\varepsilon$ = microstrain
 ν = kinematic viscosity
 ν = Poisson's ratio
 ρ = density
 σ = stress
 τ = shear
 ω_n = natural frequency (rad/s)

Subscripts

c = compression
c = cross section
eq = equivalent
H = head
h = head
i = spatial index
n = temporal index
 o, ∞ = free stream condition
R = root
t = tension
tot = total
w = wall
x = mean flow direction

1 Introduction/Motivation

Why develop a skin friction gage? Aeronautical engineers since the time of Sir George Cayley have sought to take advantage of the interaction between flow and structure to permit flight. The British engineer proposed separate aerodynamic lift and drag forces acting on an aircraft.¹ Over the past 100 years, designers have successfully balanced these forces against thrust and weight to achieve ever increasing performance growth. Skin friction, also called wall shear (τ_w), is one critical piece of this design puzzle. The accurate measurement of this parameter can literally mean the difference between a design that can and cannot fly. Unfortunately, the complex flows often encountered in high-speed vehicles, such as in the isolator section of a scramjet, produce shock and turbulent effects that make wall shear difficult to measure. The dramatic possibilities of such complicated flows are evidenced in Figure 1-1. In fact, this image is from a test conducted to determine the capabilities of the new class of gage built through this research.

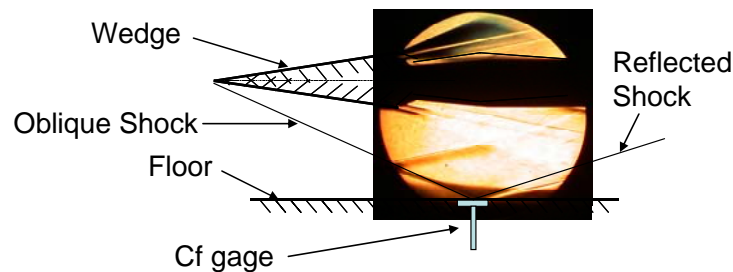


Figure 1-1. Shadowgraph in Virginia Tech's supersonic tunnel with Mach 4 nozzle.

At relatively low speeds, the only means of imposing flow force to the body is through two surface loads: a normal force and a tangential force. Respectively, these forces are pressure at the wall (P_w) and wall shear.² Even at supersonic speeds where wave drag and shock impingement become dominant, the flow effects are still translated to the structure through these surface loads. At hypersonic speeds, flow ionization produces a magnetic field that can affect ferrous structures. This additional force is currently being researched for flow control.³ Finally, heat flux can produce thermal loading that must be considered in thermal-mechanical systems.

Of these loads, what impact does skin friction have on overall system performance? The answer depends on the flow regime being considered. The focus of this research is hypersonic flight and specifically measuring skin friction in supersonic-combustion ramjet or scramjet engines. Although the skin friction coefficient (C_f) is typically a low value, around 0.002-0.005, the high dynamic pressure (q) experienced in hypersonic flight makes this parameter extremely important.⁴ This occurs through the relation $\tau_w = C_f q$. Additionally, the shock-rich environment can make measuring wall shear difficult. Therefore, let's examine the specific impact of just the wall shear component of drag on scramjet performance.

1.1 Scramjet Performance

First let's delve into the scramjet engine to see how it works. The scramjet is a mechanically simple system. A sample cut-away view is shown in Figure 1-2. This shows a cross-section of a convergent-divergent nozzle with a combustor in the middle. This profile can be rotated about an axis of rotation or extended into the page. In Figure 1-2 separate sections of the engine are labeled. We will follow the flow path from left to right. First, the unavoidable fore body shock precedes the inlet. The flow then forms an oblique shock train in the isolator section. This allows a desired static pressure rise without as grave a total pressure loss as with a normal shock. This maintains a supersonic flow throughout the engine allowing for higher ram pressure than a ramjet. The fuel is injected in the isolator section for mixing. The mixture is then combusted and expanded through the aft-body nozzle.

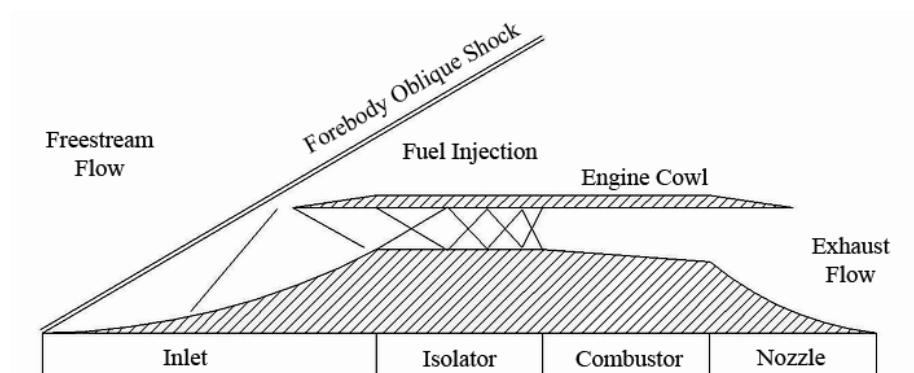


Figure 1-2. Scramjet cross-section.

To gain a better appreciation of skin friction impact on scramjets, it's useful to examine this engine type against other engines. Figure 1-3 shows the flight regimes of several classic engine types burning molecular hydrogen as fuel. The colored diamonds portray the performance of a typical engine for each class using respective cycle analysis for verification. The engine performance characteristics for each of these representative engines are detailed in Table 1-1.^{5,6} Figure 1-3 clearly illustrates the trade-off between fuel consumption and velocity. Additionally, the higher velocity air-breathing engines cannot function in lower-speed flight. The chemical rocket has the advantage of being able to fly across a broad spectrum of velocities, but at the expense of additional oxidizer and correspondingly higher take-off weight.

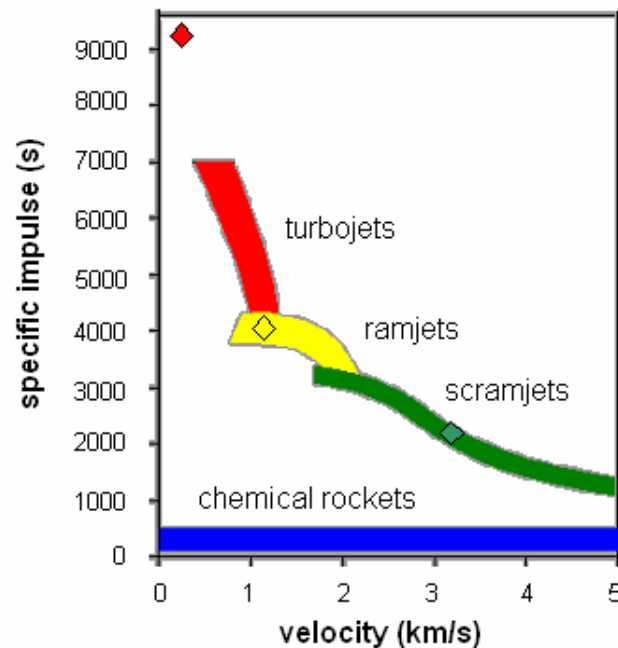


Figure 1-3. Flight regimes of various propulsion systems burning H₂.

The data from Table 1-1 provides the propulsion engineer with an apples-to-apples comparison of system performance. These values are the same as quoted in industry by engine manufacturers. Each engine color in the table corresponds to the same diamond color in the plot. Again the clear trade-off is between speed and fuel consumption. If you want to go fast, you have to burn more fuel. Fortunately with a scramjet, you can go really fast without burning as much fuel as with a rocket motor.

Table 1-1. Engine performance parameters for 3 air-breathing engines burning H₂.

H ₂	Turbojet	Ramjet	Scramjet
F/mo(lbf-s/lb)	72.354	111.2	63.35
S (lb/(lbf-s))	1.09E-04	2.52E-04	4.59E-04
Isp (s)	9191	3971	2177
Vo (km/s)	0.443	1.15	3.05
η_o	0.333	0.495	0.545
η_{th}	0.594	0.762	0.545
η_p	0.56	0.65	0.999

The performance capabilities of the scramjet make it suitable for many applications. One such use led to design work on NASA's single stage to orbit Aerospace Plane shown in Figure 1-4. Along with staging for low-earth orbit, the scramjet's high velocities make it a strong contender for long range missiles that absolutely, positively must destroy a target within seconds, guaranteed. Because these engines do not carry an oxidizer, the payload can be greatly increased over a similarly classed rocket. Hopefully, these arguments have shown that scramjets are not only intriguing and worthy of study, they actually have a market niche that is currently untapped.



Figure 1-4. NASA's Aerospace Plane concept art.⁷

At this point we have a general understanding of how the flow moves through the scramjet. In order to understand how skin friction affects performance, we must apply some rough numbers to design. The dynamic pressure profile through the engine can be approximated using the stream thrust analysis method.⁸ Figure 1-5 shows this dynamic pressure variation through a low-drag engine. We will examine three engines: 1) Ideal 2) Low Drag and 3) High Drag. Therefore, Figure 1-5 shows the dynamic pressure profile through Engine 2. The key point to take away from this figure is the high dynamic

pressure achieved just prior to the combustor. Even with a low skin friction coefficient, this large dynamic pressure produces tremendous drag.

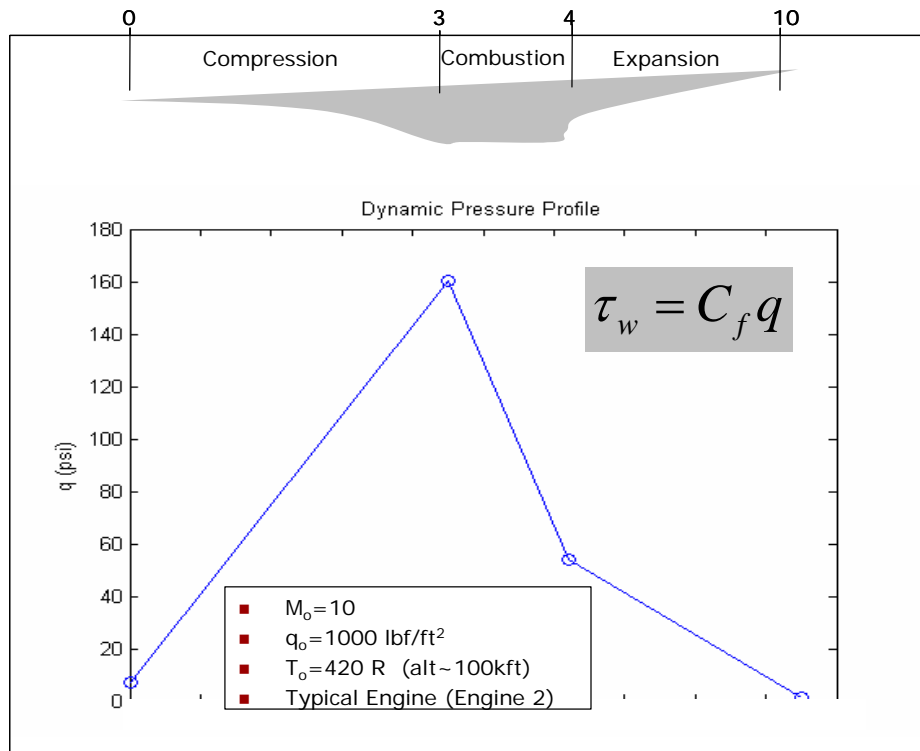


Figure 1-5. Dynamic pressure profile through typical scramjet engine.

Now let's examine the performance of the three hypothetical scramjet engines. Engine 1 is an ideal case, where skin friction is assumed to be negligible. Engine 2 is the low drag engine of our dynamic pressure profile where the wall shear in the isolator and combustor are both low, but reasonable values. Finally, Engine 3 is a high drag case where both isolator and combustor produce large wall shear, again with reasonable values. A real engine design will have drag characteristics that fall between the Engine 2 and Engine 3 cases. Figure 1-6 indicates the drag coefficients for the isolator against the combustor. The shaded area represents a bound design space of realistic component wall shear values.⁹ This broad envelope is beyond normal expected limits, but provides a reasonable starting point.

We analyze each engine under the same flight conditions for comparison. Realistic free-stream conditions for on-design analysis are set to $M_\infty = 10$, $q_\infty = 1000 \text{ lbf/ft}^2$, and $T_\infty = 420 \text{ R}$. Figure 1-6 shows the corresponding T-s diagram for each engine. The

relatively high entropies reached by the drag engines clearly indicate performance losses. The same performance parameters used to compare engines of different type delineate the performance of each of our scramjet engines. Table 1-2 provides the necessary data to determine the impact of wall shear on engine performance. The thrust going from an ideal to a low drag case shows a 6 % reduction. Even more severe, the high drag engine causes a 31% reduction in thrust from the ideal case.

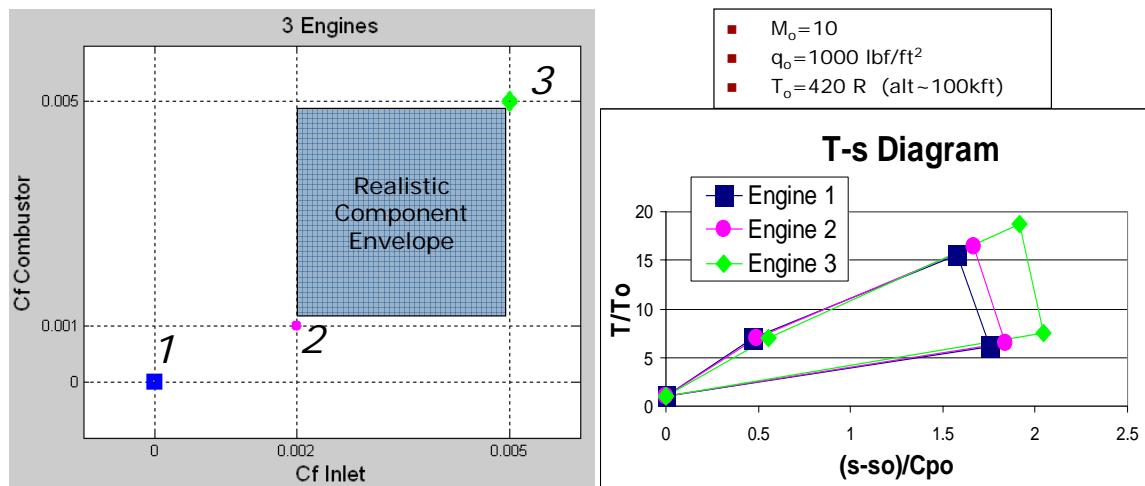


Figure 1-6. Scramjet engine design matrix and T-s diagram: 1) Ideal 2) Low drag 3) High drag.

Table 1-2. Performance parameters for 3 scramjet engines.

	Engine 1	Engine 2	Engine 3
F/mo (lbf-s/lb)	63.35	59.65	48.39
S (lb/(lbf-s))	4.59E-04	4.88E-04	6.01E-04
Isp (s)	2176.99	2049.81	1662.85
η_0	0.545	0.513	0.416
η_{th}	0.545	0.508	0.398
η_p	0.999	1.009	1.046

This investigation into scramjet performance has partially answered our initial question. Why develop a skin friction gage? Clearly skin friction has a tremendous impact on overall engine performance. We have seen that for the engine type we are interested in, the scramjet, wall shear can cause between a 6% and 31% reduction in thrust from ideal. The designer cannot afford to guess on the amount of drag with this

range of thrust. Even taking the conservative route by assuming a 31% reduction in thrust requires huge structural weight increases that lead to other problems. But why can't we just estimate the drag from computational fluid dynamics (CFD) or some other method? This is the topic of discussion for the next section.

1.2 Estimating Skin Friction

We've seen that skin friction is important, but can't we just estimate it? Unfortunately, a CFD turbulence model indirectly relies on an estimate of the wall shear. Other techniques exist for predicting skin friction in compressible turbulent flows. The bad news is that for each technique we try we get a different predicted value. Not only is this frustrating, but the only way to resolve the issue is to make a measurement. With a measured value, a more complicated model can be validated. You may wonder why we even make a model if we have to make a measurement. Actually, one only need measure the wall shear at a point as an anchor for a complicated model where the wall shear varies across the surface.

As an example of how estimated values of wall shear can range with technique, let's examine the flow field in the Virginia Tech supersonic tunnel with Mach 4 nozzle. Figure 1-7 shows the measured boundary layer using a triple-rake survey. The triple-rake is located 0.046 m downstream of the C_f gage center location. This boundary layer information is used directly in each method to determine skin friction.

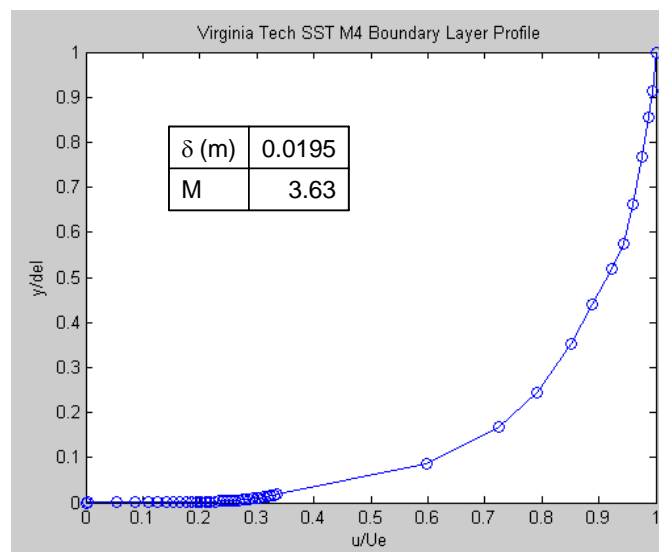


Figure 1-7. Boundary layer profile Virginia Tech supersonic tunnel.

Three separate techniques of estimating wall shear are employed: Van Driest II, Schlichting, and Eckert.^{10,11,12} The Virginia Tech supersonic tunnel conditions can be modeled as steady flat plate flow. The only added complications come from compressibility effects and high Reynolds number, i.e. turbulence. Both of these complications are considered in each of the three models employed. Table 1-3 shows the different estimates for wall shear for the Virginia Tech supersonic tunnel.

Table 1-3. Estimates for the Virginia Tech supersonic tunnel.

	Van Driest II	Schlichting	Eckert
Cf	0.712E-3	0.641E-3	0.503E-3
τ_w (Pa)	74.2	66.8	52.4
\dot{q}_w (W/m ²)	1856.3	1671.5	2198

This table clearly illustrates the problem with wall shear estimation. Even using the exact same flow conditions, for a rather simple high-speed flow, the techniques produce results that at the extreme vary over 40%. Additionally, the flow measurements were taken approximately 0.046 m behind the location of the skin friction gage. Even in this short space, boundary layer growth would suggest that the wall shear drops from the skin friction gage location to the location where we measure boundary layer height.

The relatively straight forward flow in the supersonic tunnel is easier to model than in real scramjets or high enthalpy facilities like the Large Enthalpy National Shock (LENS) facilities.¹³ In these hot reacting flows, simpler transformation models break down due to dissociation. We can no longer apply the perfect gas model. Fortunately, the Eckert reference enthalpy method can apply to these flows.¹⁴ This technique is applied to the conditions expected at LENS and produces a reasonable estimate of 2000 Pa during testing.

The preceding arguments have been based on two assumptions that could be completely wrong depending on the location of interest in a scramjet. The first is that there is a skin friction to measure. This assumption could be completely invalidated in an isolator section with shock-impingement that has caused boundary layer separation. In such a location, the wall shear might be zero, or the flow may have reversed direction in a small recirculation zone so that the wall shear would be negative. The second

assumption is that the wall shear has some steady value. In the turbulent flows we're examining, the flow field is by definition unsteady, and this translates to a time varying wall shear. As followers of the law of the wall, we expect that any variance would be minimal within the laminar sub layer, but the possibility of time varying wall shear exists. As proof of the relation between wall shear changes and turbulence, consider the success of Van Driest's oscillating wall model in representing turbulence.

Through evaluation, we can select a location to measure the wall shear that is relatively constant, positive, and away from shocks. Using this location as an anchor for a complicated CFD model, we may still capture much of the complicated flow physics with the believability that in at least the relatively calm region we are able to successfully match a measured wall shear value.

The problem arises when we have placed a gage in an isolator that sees off-design parameters. This is the reality of a gage used in flight test. Such off-design characteristics will shift the shock train in unavoidable ways that might manage to place an oblique shock on or near our measurement device. If we mistakenly ignored such potential problems, we could report wall shear values that are completely wrong. This is the case when employing a robust gage incorrectly. The gage designs of this research provide a clear method of avoiding such an error.

We've answered why wall shear is important and why we want to measure it. We need to decide how to measure it and how we know whether or not the measurements are reasonable. This is the subject of the next section.

1.3 Measuring Skin Friction

How can one measure just the wall shear in a flow field with complex turbulence, shock-impingement, and varying heat-flux? What if we could actually separate out pressure variances due to shocks from wall shear and give reasonable measures of both the shock effect and the wall shear? We've jumped a little bit ahead, but this is exactly the concept that is proposed and proven through this research. Before going too far, consider methodologies for measuring wall shear.

There are a variety of methods for measuring skin friction. Each of these has advantages and disadvantages which normally have to do with the flow to be measured. Figure 1-8 provides a classification hierarchy for methods of measuring skin friction.

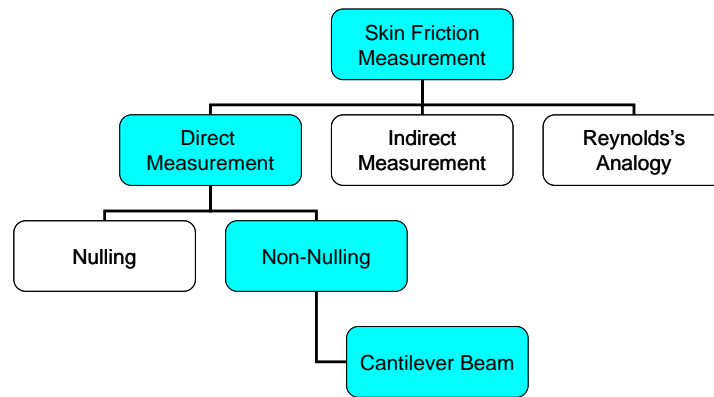


Figure 1-8. Skin Friction measurement technique classification hierarchy.

Orr provides an excellent overview of many methods for measuring skin friction.¹⁵ Of these, the direct measure method is desired for these high speed high heat flux environments. A tabulation of direct measure methods to date is available at http://www.aoe.vt.edu/~jschetz/Skin_Friction/Cf_Gage_Table&Refs.pdf. None of these previous gages provide a method of separating wall shear and pressure variation effect except for those written by the author. This is a new area of research.

The initial concept for this new kind of gage has its basis in previously built cantilever beam type gages. A non-nulling gage is preferred for simplicity and faster time response. Figure 1-9 shows an idealized version of a cantilever beam direct measure gage on the left. In this gage design, the flow moves across the head surface causing a deflection. This deflection can either be measured directly, or the resulting strain can be measured, as is our case. One advantage to this design is its ability to have little motion due to the relatively strong wall pressure loading while producing a relatively large output due to the small wall shear.

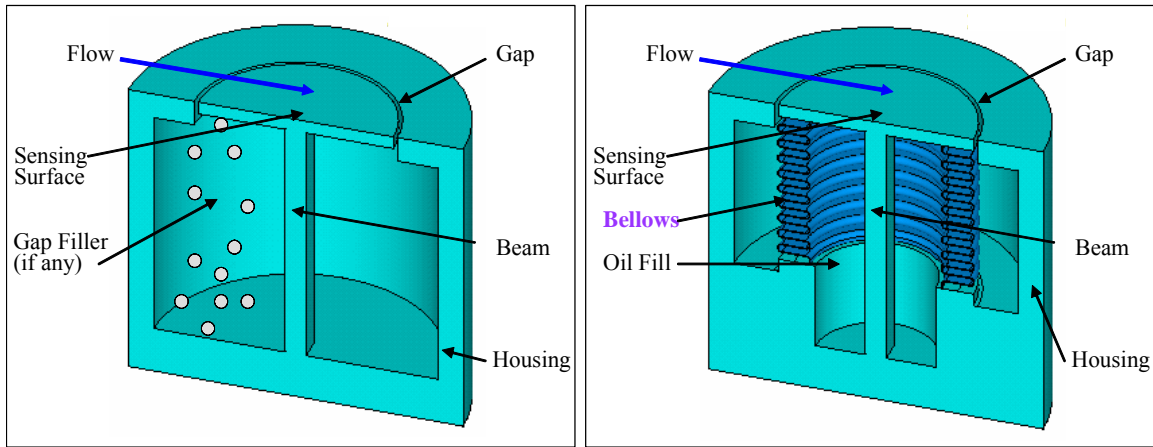


Figure 1-9. Idealized skin friction gage cut-away.

The right side of Figure 1-9 shows a 3-D rendering of the bellows type gage developed through this research. It contains many of the same features as the idealized skin friction gage. The main similarity is the exposed surface that is influenced by the flow and the beam that flexes to the load. The main difference is that the bellows forms a cavity that traps the oil filler and keeps it free from air bubbles. As will be described in this paper, the oil fill provides thermal and damping characteristics, but more importantly, it helps to eliminate uniform wall pressure as a variable.

1.4 Skin Friction Gage Design

A general assembly cartoon for the oil-filled bellows skin friction gage is shown in Figure 1-10. Here we see the main components that make up this gage. The first image shows the element, and the sensing surface is highlighted. The head and root strain gages are applied at the locations on the beam as shown. The stem provides a surface for solder tabs, strain relief, and a handle for proper alignment. In the next image we see how the bellows slides up and around the element. The base follows suit, and all three components are epoxied together. The bellows cavity is filled with oil, and a plug is inserted to prevent leaks. Finally, this entire assemblage is placed in a housing with a small gap at the head for motion.

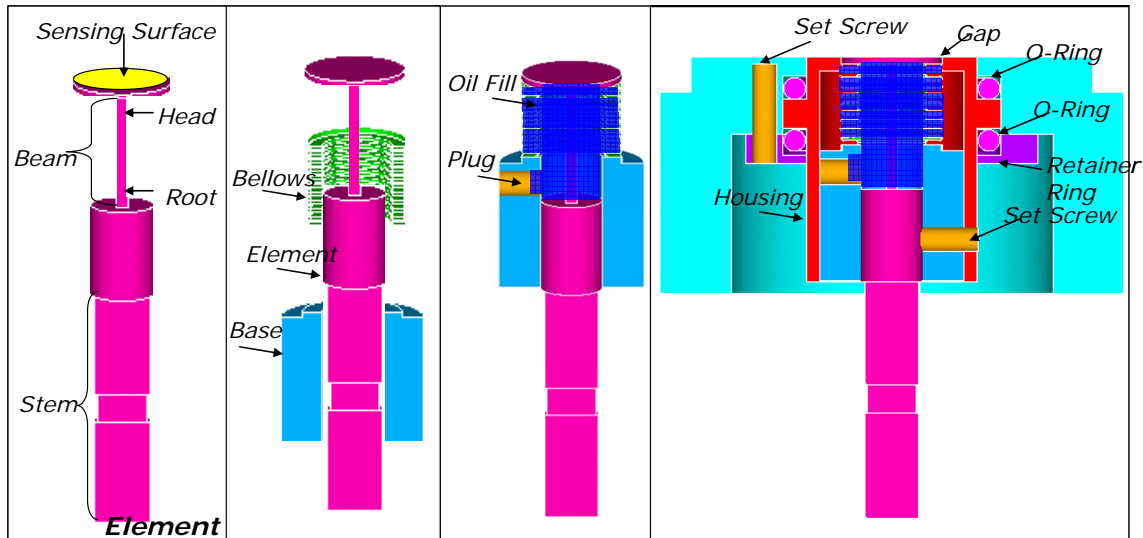


Figure 1-10. Assembly of oil-filled bellows skin friction gage.

Through this research, we have designed four separate gages for fabrication, CF1 through CF4. These gages are shown in Figure 1-11. Each gage is made with an element which is green, a base which is grey, and a housing which is pink. Each gage also has a bellows shown in blue. The critical component that determines how the gage functions is the element. This component has the exposed sensing surface that is affected by the flow and the beam whose strain distribution is used to measure wall shear. All of these gages share the general head and beam of the idealized gage in Figure 1-9, even though the dimensions are different. These gages vary in geometry and material. CF2 through CF4 use a FC8 bellows and Lee-plug for oil fill. CF1 uses a small FC3 bellows without oil fill. CF1 also lacks a stem. All gages are made of aluminum except CF3, which is made of INVAR.

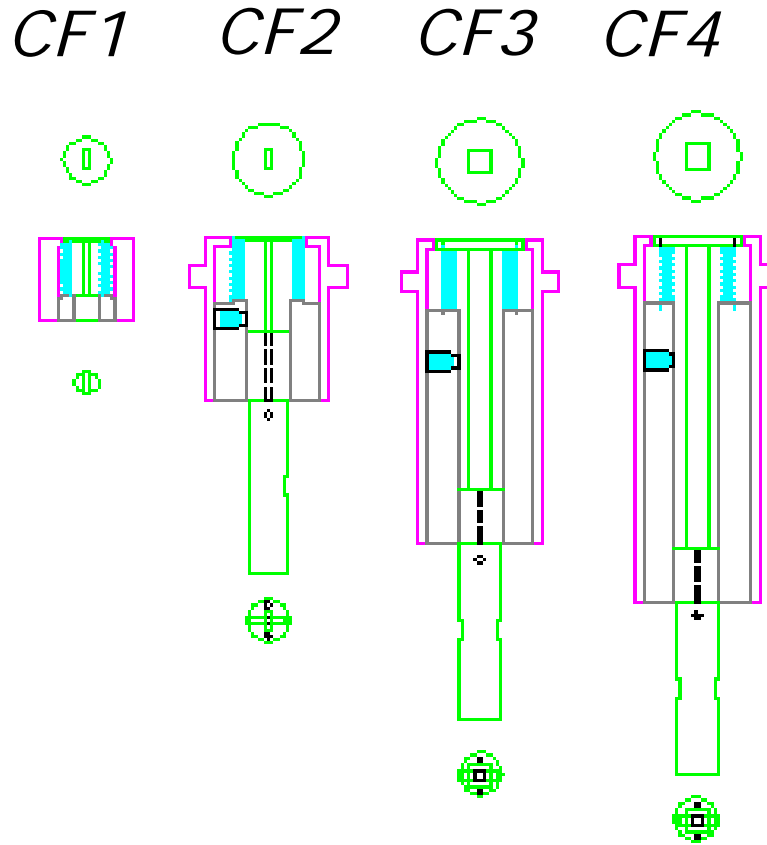


Figure 1-11. Skin friction gages from this research to scale.

These gages are design solutions to measure wall shear while exposed to the nominal set of load conditions shown in Table 1-4. These conditions represent a simplified steady state for a high-enthalpy, short-duration test. The steady state for a test of this type is about 10 ms. The wall shear is assumed to act mainly in the direction of the mean flow path and spanwise shear is neglected. The acceleration, a_x , is caused by the motion of the test model being measured. This motion is also dominant in the mean flow direction. Finally, the heat flux, \dot{q}_w , acts perpendicular to the sensing surface.

Table 1-4. Nominal design specifications.

	Time (ms)	τ_{wx} (Pa)	a_x (m/s ²)	\dot{q}_w (kW/m ²)
Load	10	2000	9.8	100

Each gage should accurately measure wall shear and be insensitive to pressure, temperature, and shock impingement. Since all of the gages of this research were designed to these nominal specifications, a good question is ‘why are they so different?’ These gages have evolved with our understanding of the problem. Though each gage has successfully met our requirements at each step along the way, those requirements have been finely tuned. The culmination of these efforts is a design optimization methodology that can take high fidelity requirements and provide the best solution to meet them. In fact CF3 and CF4 designs are optimizations to the highly evolved requirements developed through this research.

The overall objectives of this research follow:

1. Design, build, and test a gage that separately measures wall shear and moment.
2. Determine the best gage characterization techniques.
3. Develop an optimization method for gage design.
4. Use the optimization technique to design gages for three disparate test conditions:
 - 1) short-duration, high-enthalpy testing, 2) blow-down testing, and 3) flight testing
5. Develop simulations for complicated physics.

In order to understand the design methodology of the bellows direct measure gage, Chapter 2 presents a complete idealized simulation. This theoretical approach is an overview of load, gage, and instrumentation interaction. It provides the foundation for gage geometry, strain gage placement, and Wheatstone bridge design. It also explains why the gages shown in Figure 1-11 share many common traits. This theoretical approach is directly applied to achieve the first objective.

The first objective, to separately measure wall shear and moment, is addressed through the design, development, and testing of the CF1 and CF2 gages. Chapter 3 presents the evolutionary process and experimental results for CF1 and CF2. The oil-filled bellows of CF2 eliminates uniform pressure as a variable and increases damping. The most important contribution in this section is the experimental proof of the ability of CF2 to separately measure wall shear and moment when impinged with a shock.

Chapter 4 examines the performance of each gage to the nominal load conditions. Through this process, objective 2 is met. The best method for accurately predicting gage response is determined. We select the best model to predict: 1) wall shear induced strain

and displacement 2) shock impingement induced strain and displacement 3) vibrational frequency 4) inertial effects and 5) thermal strain.

Once the modeling techniques to characterize gages have been built, they can be used to develop an optimization procedure for a specific set of load conditions. Chapter 5 presents the development of this procedure meeting the 3rd objective. It also provides optimized solutions for the three test conditions listed in the 4th objective. This is accomplished through the development of the CF3 and CF4 gages. First, initial decisions bound the geometric design space. This space is then discretized so that we can examine hundreds of possible gages. The imposed constraints on state variables further collapse the possible solution set. Finally, our desired performance parameters are applied to select the best design for application.

Chapter 6 uses simulations to answer the tough physical questions that developed during this research. These higher tiered models look at flow, gage, and instrumentation interaction. This final objective allows us to answer the following questions: What filter should be applied? How will the gage respond to a time varying load? How about time varying inertia? Then, we look at the thermal effects on measurement. Could errors in strain gage placement cause a voltage output due to temperature? What kind of error can be expected from instrumentation? Could a spatially varying heat flux cause apparent strain?

Finally, Chapter 7 presents conclusions and recommendations. This chapter details the contributions from this research. It also discusses how well we met our objectives. Finally it provides short and long term recommendations.

2 Theoretical Approach

The gage development is iterative, but must start with a theoretical model. A good model is as simple as possible, captures the essence of the physics, and produces useful results. In our case, we are interested in accurately modeling the flow, the gage response, and the instrumentation output. Though we will examine complex physical simulations and optimization later, this chapter presents the first iteration in the modeling process. This idealized simulation assumes 2-D steady flow, a cantilever beam gage, and ideal instrumentation. This low-fidelity combination provides the most elegant means for understanding the design features of this new class of skin friction gage. It unveils the fundamental means for separating out pressure variations from wall shear.

2.1 2-D Steady Flow Model

The first flow model for simplicity is 2-D steady flow. Figure 2-1 shows a cutaway view of a generic supersonic wind-tunnel cross-section as well as the flow-field coordinate system used throughout this research. The blue arrow represents the mean flow direction which is parallel to the x-axis, and the y-axis is perpendicular to the flat plate. The coordinate system is centered on the top surface of the skin friction gage.

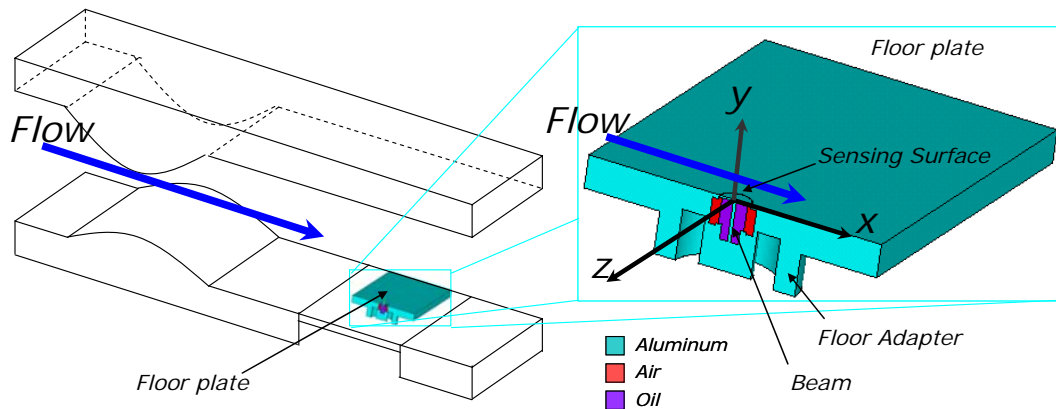


Figure 2-1. Cut-away view of tunnel test section with flow-field coordinate system.

In this 2-D steady case, only the mean turbulent flow is considered. The two surface loads, pressure and wall shear, act on the structure. Should a shock impinge on the surface, the wall pressure distribution varies with axial length. This particular situation will be explored in greater detail in the next section. The heat flux and

acceleration are assumed constant. In summary, we are interested in four simplified load conditions shown in Table 2-1. Notice that wall shear and inertial loads are assumed axial.

Table 2-1. 2-D steady flow conditions.

Wall Shear	Pressure	Heat Flux	Acceleration
τ_{wx}	$P_w(x)$	\dot{q}_w	a_x

2.2 Cantilever Beam Gage Model

The previous section outlined a simple set of flow load conditions. The simplest gage model available is the cantilever beam. When switching to the gage reference frame, we first focus on the axially varying pressure distribution. This is the case when a 2-D shock impinges on the head of the skin friction gage as shown in Figure 2-2. This critical case is encountered in many high-speed flow situations including the shock train that develops in scramjet isolators. Zooming in on the gage itself, we can begin to examine how this flow condition acts on the gage.

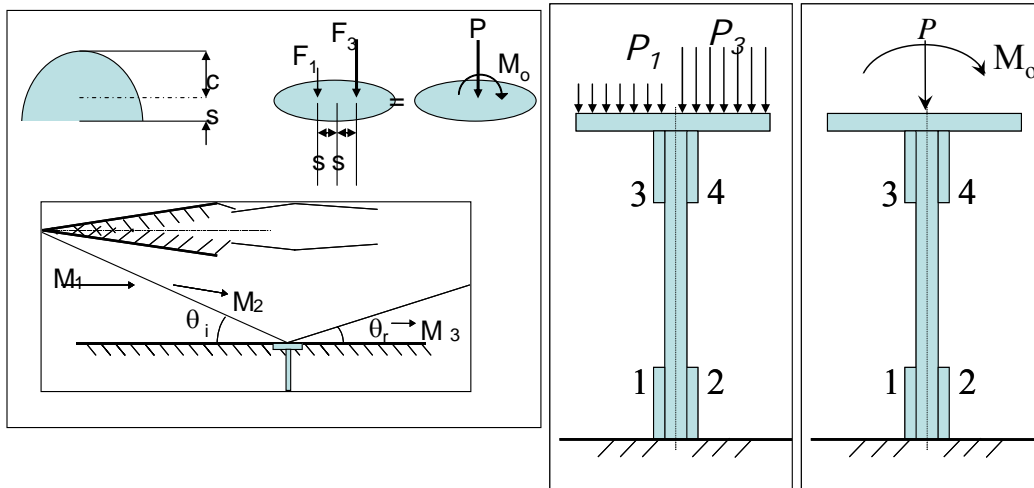


Figure 2-2. 2-D shock impingement diagram.

A simple gas dynamics analysis of the flow situation presented in Figure 2-2 breaks the flow into three separate regions. The flow acting on the front half of the gage surface is at a relatively low static pressure, P_1 . The flow acting on the rear half of the gage surface has traveled through an oblique and reflected shock and is at a higher static

pressure P_3 .¹⁶ This 2-D distribution is shown in the second figure. From the gage perspective, this pressure distribution has an equivalent moment and pressure load as shown in the third figure. These are $M_o = (P_3 - P_1)2r_h^3/3$ and $P = (P_3 + P_1)A_h/2$ respectively.¹⁷ Since P is simply a uniform wall load, from the beam reference frame, it can be applied as a point load. We will rename this load P_w for the shock impingement case.

Now we can describe any 2-D flow load acting on the gage head as three simple separate loads from the beam perspective. The beam reference load conditions are shown in Figure 2-3. From the beam reference frame a complicated axially varying pressure load, $P_w(x)$, has been broken into two simple equivalent loads, P_w and M_o . The wall shear remains the same. Notice that the x subscripts have been dropped, since the vectors define the direction.

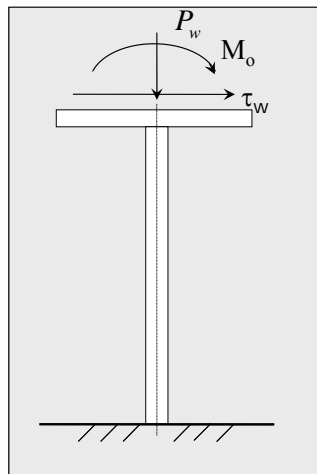
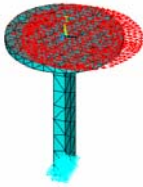
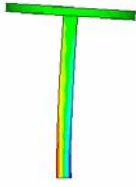
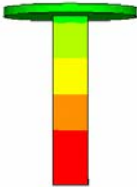
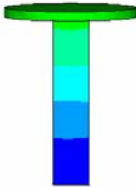
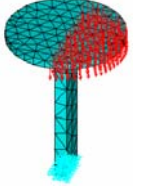
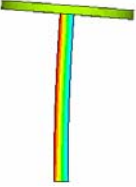
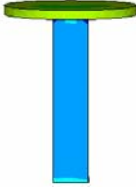
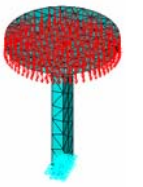
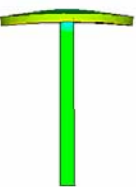
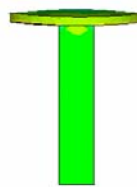
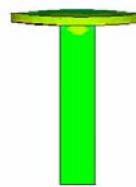


Figure 2-3. Cantilever beam with surface flow loads.

A convenient effect of using the beam reference frame is that each of these loads is well understood in beam theory. For example, the uniform pressure load compresses the beam and provides a constant but relatively small strain along its length. The moment load places the beam front face in tension and the rear in compression. The wall shear also places the beam front in tension and rear in compression. In the case of the moment load, the strain produced is a constant for each side of the beam. However, the strain produced by wall shear is a maximum at the beam root and gradually decreases to zero at the head. The effects of each of these load cases are shown qualitatively in Table 2-2. In this table, the term “Tension” refers to the upstream face of the beam since the beam is in

tension for wall shear or moment loads under these flow conditions. “Compression” describes the downstream beam face. These particular images were developed using finite element modeling which will be covered extensively during gage characterization.

Table 2-2. Strain distributions for typical beam loads.

Model	Load	Side View	Tension	Compression
				
				
				

Although the real inertial and heat flux loads are quite complicated, we can take some simplifications from our simple 2-D steady flow model. Since we have dictated that the inertial load is purely axial, we can calculate an equivalent acceleration shear. Thus, if the strain produced by inertial loading is much smaller than that from wall shear, we can ignore inertia. Since the heat flux is assumed constant, any temperature distribution will be gradual from the head to the root of the beam. Therefore, we expect the temperature on the tension side of the beam to mirror the temperature on the compression side. This is a useful assumption since the strain varies directly with temperature.

The fundamental output we seek for any gage model is the elastic strain along the beam axis at each strain gage location. In other words, our generalized desired output is $\epsilon(x,y,z,t)$. We are interested in the elastic strain in line with beam elongation or shortening, ϵ_y . The y subscript refers to the flow coordinate system y, perpendicular and up from the floor plate and aligned with the strain gages. This particular strain shows changes along the beam length. This strain sums the outputs of five sources of strain: wall shear, ϵ_{τ_w} , pressure, ϵ_{P_w} , thermal gradient, ϵ_T , moment, ϵ_{M_o} , and inertial loading, ϵ_a . These strains correspond to the loads shown in Figure 2-4.

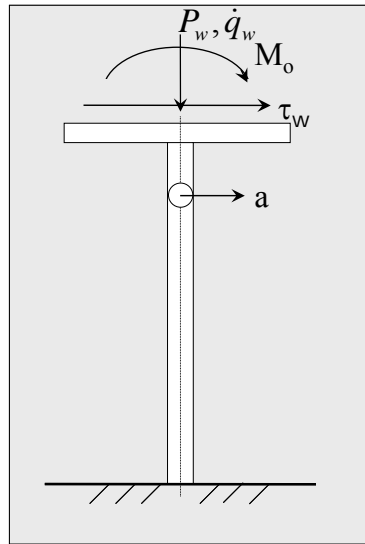


Figure 2-4. Load configuration for simple cantilever beam.

2.3 Ideal Wheatstone Bridge Model

The gage motion produces a voltage output signal through strain gages placed along the beam wired through Wheatstone bridges. As each strain gage elongates or shortens, its resistance changes proportionally through Equation 2-1. By applying a constant excitation voltage, the output voltage provides a direct measure of the strain. Strain gages allow us to determine beam strains at a variety of locations. Wheatstone bridges provide the opportunity to manipulate these outputs in a useful way.

$$\epsilon = \frac{\Delta L}{L} = \frac{1}{GF} \frac{\Delta R}{R} \quad \text{Equation 2-1}^{18}$$

A configuration using two half-bridges consisting of two strain gages per bridge is presented. This configuration provides output results from measurements at the root and head of the gage. The overall ideal Wheatstone bridge equation is presented as Equation 2-2. In this equation for each of the half-bridges, ε_3 and ε_4 are zero.

$$V_o = \frac{V_{in} GF \cdot Gain}{4} (\varepsilon_1 - \varepsilon_2 + \varepsilon_3 - \varepsilon_4) \quad \text{Equation 2-2}^{19}$$

2.4 Ideal Simulation

The lowest fidelity model allows a complete examination of input loading to gage response to expected output signal, and finally to verification of initial load. Figure 2-5 shows a first order simulation of this system. The load conditions acting on the gage cause changes in length of the strain gages attached to the surface. The heat flux causes a temperature variation that is assumed to only vary down the axial length of the beam. With this model, we can examine the expected output due to these load conditions.

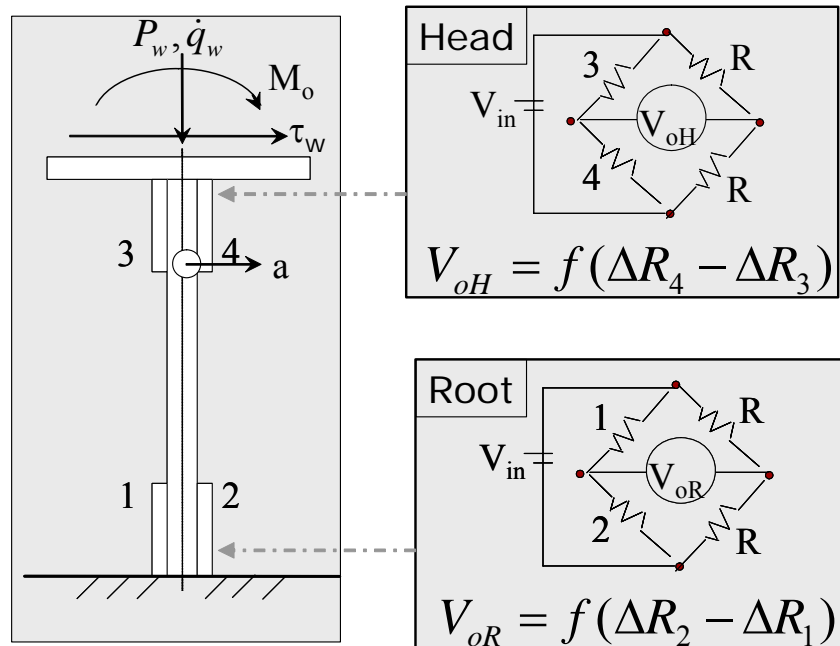


Figure 2-5. First order simulation of load, gage, and measurement interaction.

First let's look at the effect of a uniform wall pressure load. Since both the tension and compression side strain gages see the same compressive strain, we know from Equation 2-1 that we get a net zero voltage output. The same condition occurs due

to a temperature distribution that is only a function of vertical direction. Both of these load conditions are imposed on the system in Figure 2-6.

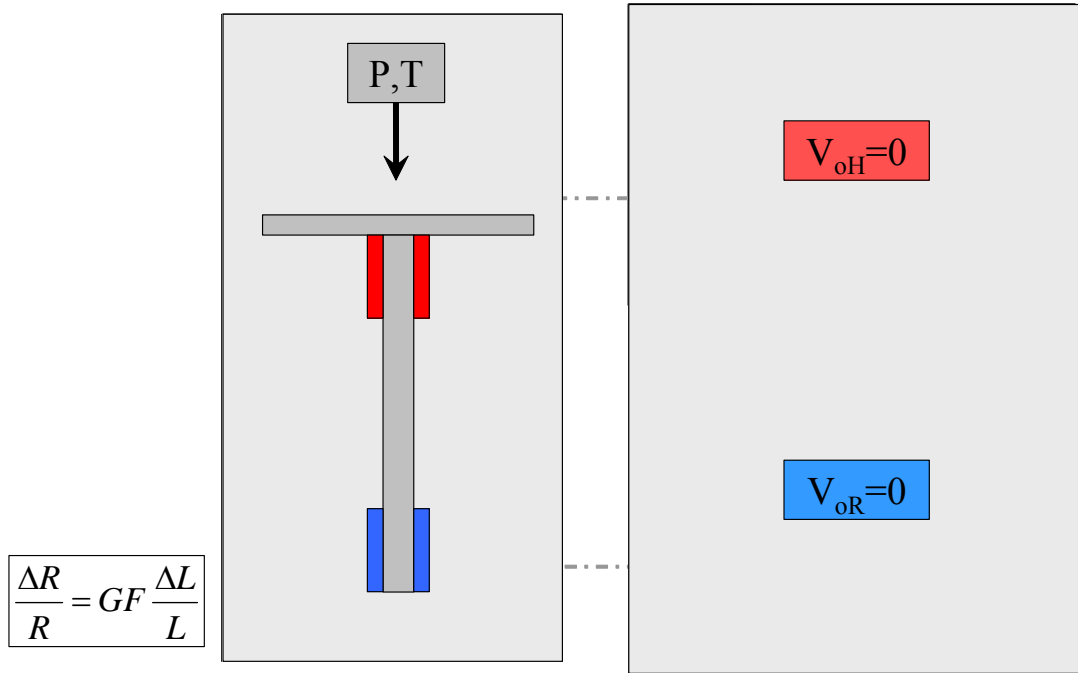


Figure 2-6. Theoretical output: uniform pressure and 1-D temperature distribution.

Since we have eliminated two of the five loads from Figure 2-5, we have reduced our loads of concern to three: wall shear, moment from a non-uniform pressure, and acceleration. If we can design the gage to minimize acceleration effects, the variables can be reduced to two: wall shear and moment. This theoretical result means we have simplified our problem to two equations and two unknowns. Better still, these loads are linearly independent, so we have reduced our problem to the following equations. The four constants are easily found through calibration.

$$V_{oR} = c_{11}\tau_w + c_{12}Mo \quad \text{Equation 2-3}^{20}$$

$$V_{oH} = c_{21}\tau_w + c_{22}Mo \quad \text{Equation 2-4}$$

The previous developed strain gage configuration was applied to CF1 and CF2 and is going to be used for several of the CF3 and CF4 gages. Because CF3 was designed to minimize thermal-mechanical effects, we do not expect to have the same thermal problems that effected CF2. However, there is a theoretical technique to

eliminate the temperature effects even if the temperature varies through the thickness of the beam. This situation is presented graphically in Figure 2-7. This situation might occur if the heat flux varies with axial flow location.

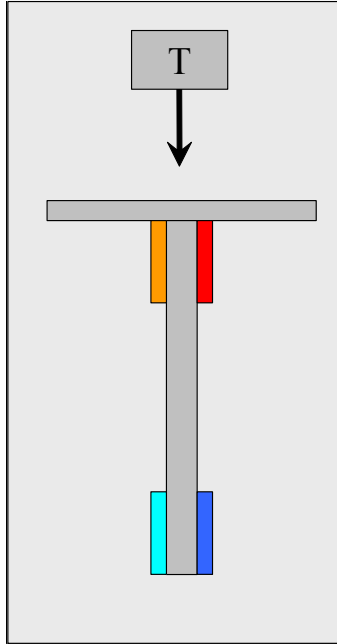


Figure 2-7. Thermal distribution where temperature varies through beam thickness.

The Wheatstone bridge configuration applied to account for this temperature variation is presented in Figure 2-8. This is done by splitting the gage along its centerline and showing the tension side on the left and the compression side on the right. Each side has a strain gage placed horizontally. This horizontal strain gage should provide little response to any load input except temperature. Therefore, the thermal effect will be cancelled by this dummy strain gage. This strain gage configuration will be tested on some of the CF3 and CF4 gages.

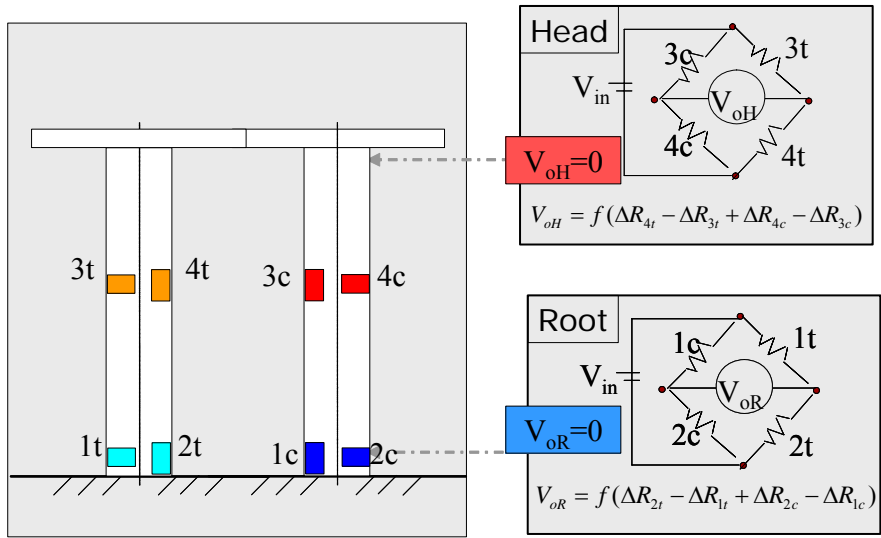


Figure 2-8. Two full Wheatstone bridge thermal compensation configuration.

3 Separately Measure τ_w and M_o

This chapter explains the design, development, and testing of the first documented skin-friction gage to separately measure wall shear and moment. This chronology follows the development of the CF1 gage and the evolutionary changes that made CF2 successful. The CF1 gage provided the first work using the bellows as a thermal barrier. The CF2 gage proved the concept of separately measuring wall shear and shock-induced moment.

3.1 CF1 Gage Design

The number of possible design choices and trade-offs for the first iteration seemed overwhelming. Fortunately, thanks to the theoretical development, we neglected certain state variables, albeit somewhat naively. Table 3-1 summarizes the effects considered and approach taken. From theory, temperature and uniform pressure effects were eliminated. Next, making the gage as light as possible minimized inertial loading. Intuitively, we would like to minimize the gap size. However, under low wall shear conditions, the gage motion was determined to be relatively small. Thus displacement, hence gap size, was left to be checked after design. Moment effects were also left for post design. This limited the design state variables to wall shear strain, frequency, and damping. Structural damping was assumed to be about 0.02 and possible methods for increasing this value were considered for CF1.²¹ These included using grease on the bellows and tape on the beam for viscous damping. Without knowing the total system impact, damping was temporarily shelved as a design variable. Therefore, the goal was to achieve the most strain output and highest frequency possible. Unfortunately, these two characteristics oppose each other.

Even though strain and frequency have become the focus of optimization, temperature and acceleration considerations really drove CF1 design. In order to protect the strain gages from convective heat transfer while allowing nearly unconstrained motion of the overall system, we wanted to use a bellows. Working with commercially available bellows we wanted the smallest bellows available to minimize weight. Thus we chose Servometer ® FC-3. This decision greatly constrained the amorphous design by

limiting the geometric design space. Immediately, the head thickness and head radius were set. Additionally, the maximum beam radial dimension was constrained and the beam length was set. It also made optimization of strain and frequency manageable. Thus, our design variables have been limited to material choice and beam cross-section.

Table 3-1. CF1 design approach.

Physics	State Variables	Approach	Optimize
Temperature	$\epsilon_{\Delta T}$	Neglect (Theory)	N/A
Pressure	ϵ_{P_w}	Neglect (Theory)	N/A
Acceleration	ϵ_a	Lightweight	Minimize m(mass)
Displacement	δ	Post-Design Check	N/A
Moment	ϵ_{M_0}	Post-Design Check	N/A
Wall Shear	ϵ_{τ_w}	FEM	Maximize ϵ_{τ_w}
Frequency	f	FEM	Maximize f

In order to maintain a reasonable design space, the materials were limited to aluminum, copper, and polyethersulfone, a high-temperature plastic. These materials had been used in building previous gages. Copper is a typical skin for scramjets, aluminum is easy to manufacture, and polyethersulfone shows little thermal response. The beam cross-sections were limited to circular, rectangular, and annular. Each potential design was built as a 3-D Baseline FEM. Figure 3-1 shows the resulting response data as a function of material and cross-section.

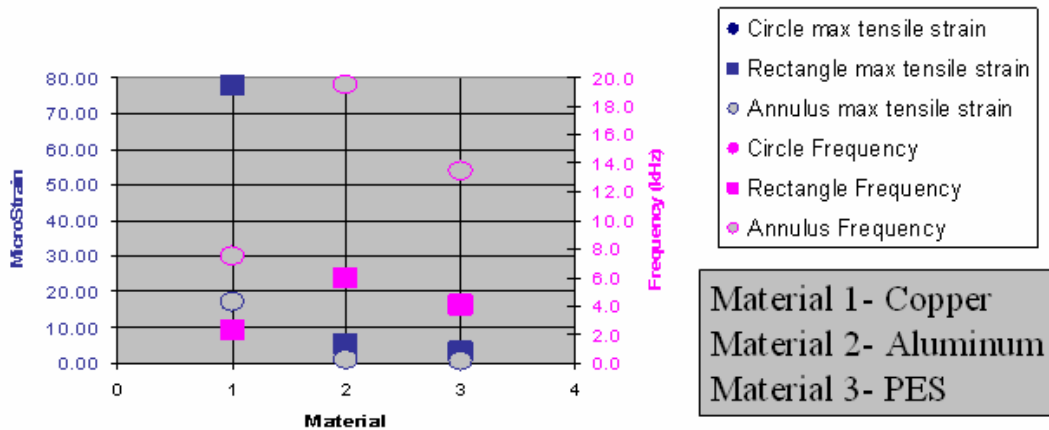


Figure 3-1. Strain and frequency as a function of material and cross-section.

This figure emphasizes the trade-off between vibration frequency and strain. The annular design posed too many manufacturing difficulties to achieve an exact mass distribution. In other words, drilling a hole exactly at the center is difficult. Also, in order to apply the strain gages on a flat surface, the circular cross-section was discarded in favor of the rectangular one. After selecting a workable cross-section, we needed to choose the best material. Because the structural damping coefficient was expected to be low, we decided that aluminum provided a reasonable balance between vibration frequency and strain.

Once an aluminum rectangular design was selected, the exact cross-section area needed specifying. This was partially limited by the strain gage selection. The strain gages were selected to have the minimum design length, aluminum self-temperature compensation, and a minimum 350 Ω gage resistance, R_G . A commercially available Vishay® EA-13-031CE-350, met the requirements with a gage length of 0.076 in. and width of 0.062 in. This set a minimum beam width for gage placement. Now the beam width was constrained to a strain gage minimum and bellows maximum. Then a sweep was made of design cross-section effect on frequency output. Figure 3-2 shows the non-linear relationship. The thinnest tested design provided a reasonably high vibration frequency. This became the design configuration that was built for CF1.

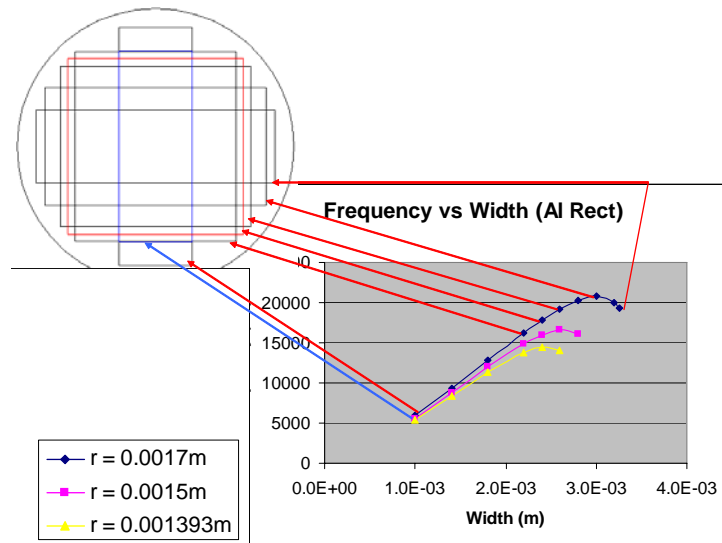


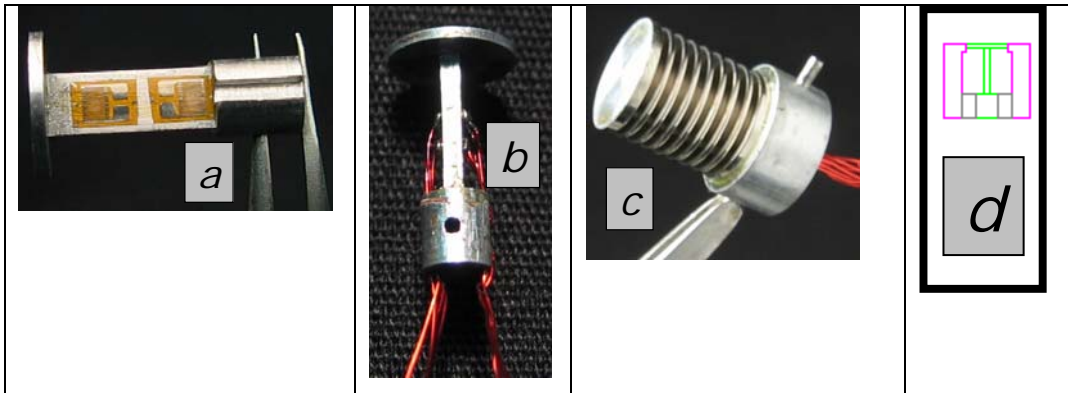
Figure 3-2. CF1 frequency sweep as a function of beam cross section.

3.2 CF1 Results

Each CF1 Wheatstone half-bridge was completed with a Vishay® Model 2310 signal conditioner. These amplifiers were set using the 10 Hz low-pass Butterworth filter, a 5 V input voltage, and 10k gain. A National Instruments® data acquisition system was controlled by programs written in LabVIEW®. The sample rate was 500 Hz. Prior to each test set, both 2310's were zeroed.

The CF1 gage met many of our design criteria requirements during static calibration. Both the static wall shear and static moment calibration had high linearity between load and voltage output. CF1 also exhibited the expected difference between wall shear induced and moment induced strain distribution. Table 3-2 shows pictures of the gage in several of its assembly stages. In (a) the element with attached strain gages is shown. Next (b) shows the wires attached. The picture in (c) shows the element shrouded with bellows and base attached. Finally (d) shows a scaled drawing of the assembled housing, element, and base.

Table 3-2. CF1 gage in stages.



3.2.1 CF1 Calibration

The CF1 gage underwent static wall shear and moment calibrations. A shaker-test to determine vibration frequency was attempted, but broke one of the two CF1 gages. After tunnel run testing, thermal, pressure, and wire stiffness sensitivity tests were conducted. These will be presented after experimental test results. Once the pressure

issue was uncovered, attempts at further CF1 frequency characterization were discarded in favor of redesign.

CF1 Static Wall Shear Calibration

The static wall shear calibration was conducted by placing the CF1 beam perpendicular to earth's gravity and applying weights to simulate wall shear. This process is sketched in Figure 3-3. A string was taped to the top surface with an attached low weight "bucket". The string, bucket, and tape provided minimal weight, but were accounted for through zeroing of the signal conditioners prior to adding weights.

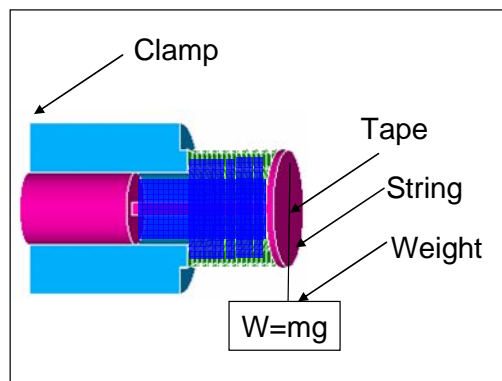


Figure 3-3. Static wall shear calibration technique.

The completely fabricated CF1 gage was calibrated using this technique. Several tests were conducted varying the weight and order of weight placement. No hysteresis effect was detected. The resulting relationship between wall shear and output voltage was highly linear as evidenced in Figure 3-4.

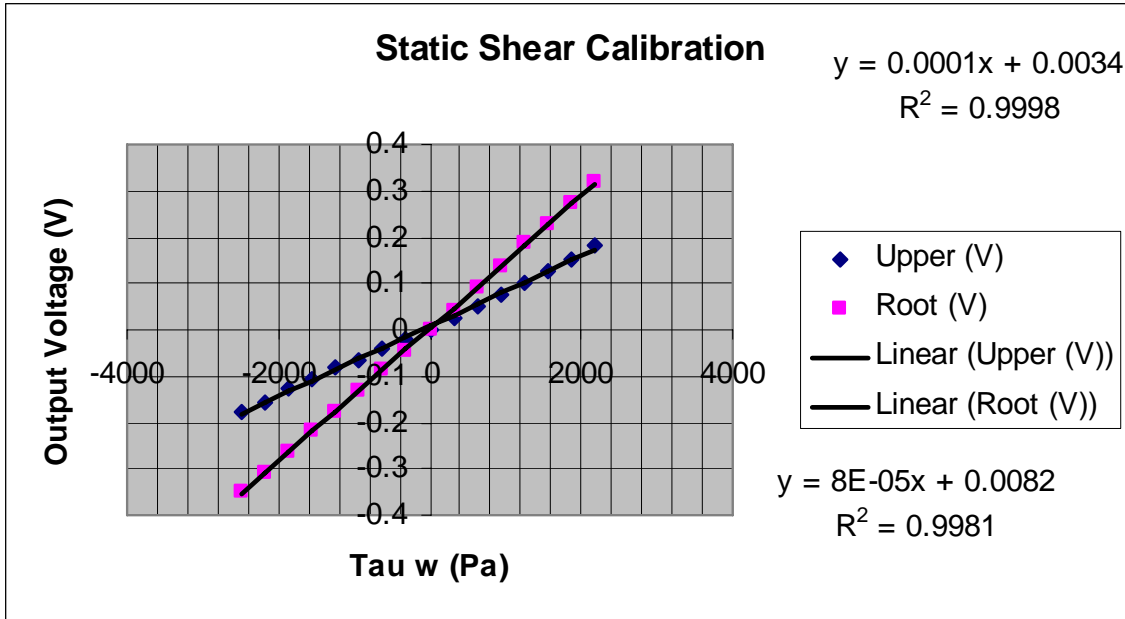


Figure 3-4. CF1 static wall shear calibration results.

CF1 Static Moment Calibration

The static moment calibration was conducted by placing the CF1 beam parallel with gravity, taping a lever arm to the gage top surface, and applying weights to produce moment. This technique is sketched in Figure 3-5. The lever arm was a long thin cylindrical bar that was centered on the head to produce zero moment without weight. Additionally, the bar was placed in line with axial flow to produce a direct moment. Weights were then added at a constant distance from the head center.

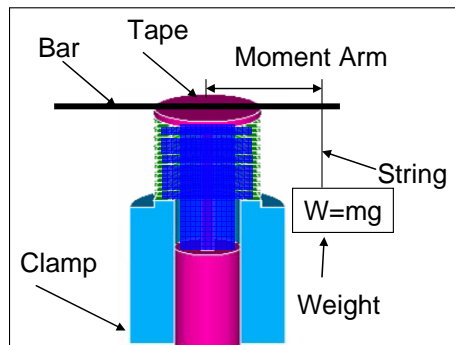


Figure 3-5. Static moment calibration technique.

A fully fabricated CF1 gage was calibrated using this technique. As with the wall shear calibration, no hysteresis effect was noticed despite varying weight loading and unloading order. The high linearity between loading and voltage output is shown in Figure 3-6.

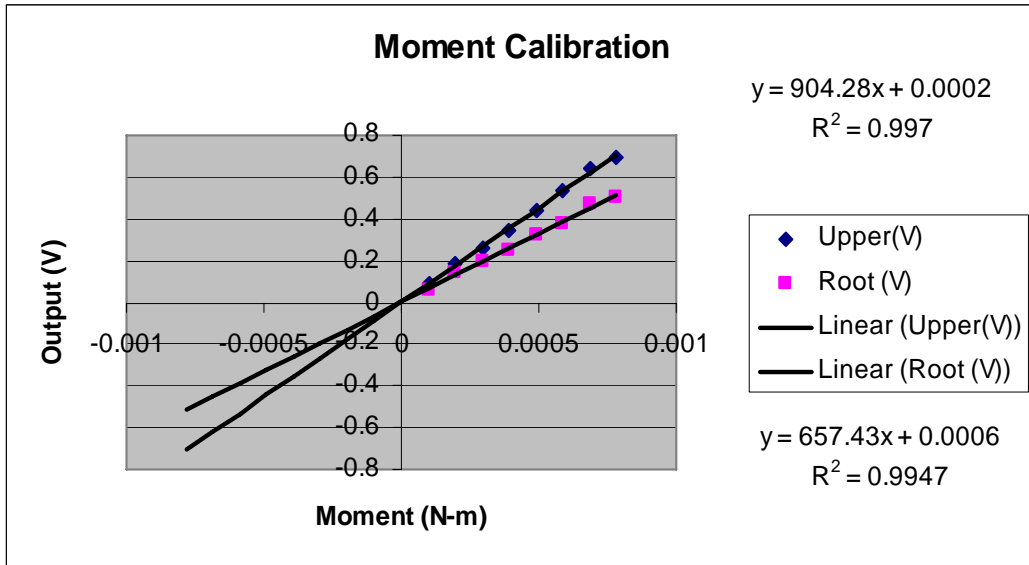


Figure 3-6. CF1 static moment calibration.

3.2.2 CF1 Virginia Tech Supersonic Tunnel Wall Shear Test

The validation experiment for CF1 was conducted in the Virginia Tech supersonic test facility with the Mach 4 nozzle installed. This is the blow-down facility shown in Figure 3-7. The test section has windows located on either side of the tunnel for taking shadowgraphs. Accelerometer measurements confirmed that this tunnel experiences negligible acceleration.

Unfortunately, the CF1 experimental test results could not be correlated to wall shear, static temperature, or static pressure. With so many possible sources of apparent strain and the possibility of instrumentation error, an investigation of CF1 behavior was conducted post experiment.

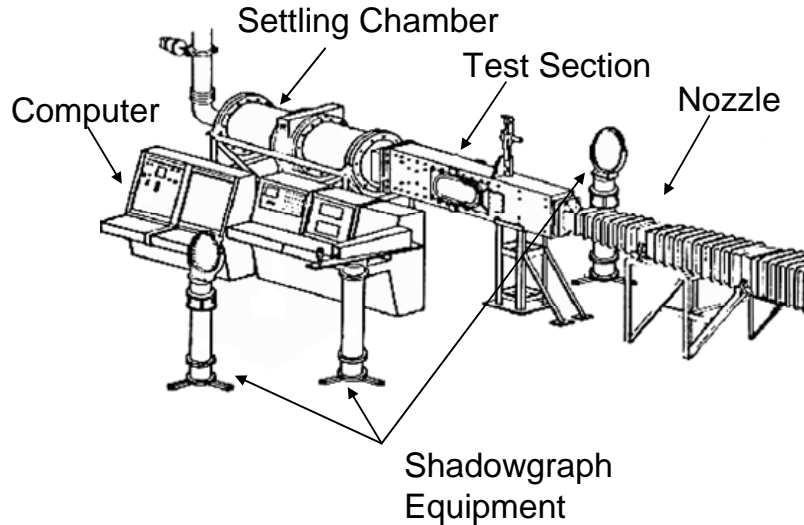


Figure 3-7. Virginia Tech supersonic tunnel diagram.²²

3.2.3 CF1 Post Experiment Investigation

During validation testing, the gage exhibited voltage output error that led to an investigation of sources of apparent strain. Each of these possible sources, thermal, pressure, and wire-stiffening, were investigated. All of these provided design inputs for CF2. The pressure issue was dealt with by using incompressible oil in the bellows. The manufacturing concerns were the need for a hold, strain relief, and solder pad surface. All of these were solved by adding a handle and securing the wires to the handle. The thermal issue was approached by using the oil as an insulator for the strain gages. Finally, wire-stiffening was solved by moving the wire holes in-line rather than perpendicular to the beam.

After the first set of test runs in the Virginia Tech supersonic tunnel facility, it was clear that some source of apparent strain was affecting the voltage output for CF1. In order to either account for this error, or eliminate it through design, several possible physical sources were examined. Static pressure, static temperature, and wire stiffening all proved to be possible sources of apparent strain.

CF1 Vacuum Test

The possibility that static pressure was a source of apparent strain required investigation. Figure 3-8 shows the vacuum test setup. The CF1 gage was connected to a

vacuum pump with a vacuum hose secured to the housing. A tee was used to connect to a 50 psi pressure transducer to measure static pressure. Additionally, a Type-T thermocouple was placed near the head of the CF1 gage to measure temperature. The other leg of the tee connected to a valve and vacuum pump.

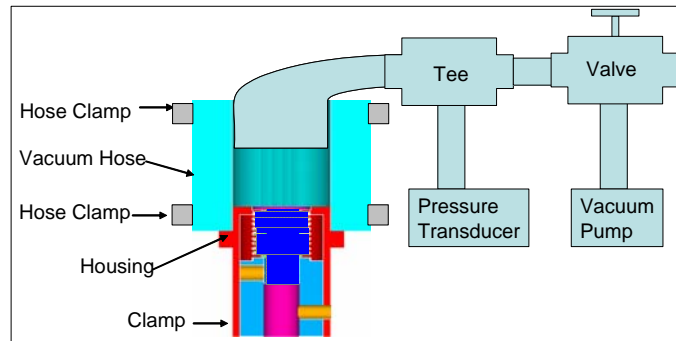


Figure 3-8. Vacuum test technique.

This test was conducted with CF1 at multiple angles to gravity. The vacuum was applied and valve closed to check for leaks. The gage reaction at the head and the root is shown in Figure 3-9. Here, the white trace shows the changing static pressure measurement. Both the head output voltage in red and the root output voltage in green trend very closely with pressure. The temperature changed less than 1 deg C during this test.

The observed pressure effect on CF1 measurements was intolerable. A possible solution to this source of apparent strain was to fill the bellows cavity with incompressible fluid. By doing so, the volume inside the bellows would remain constant. This would negate the beam's ability to expand or contract due to changes in uniform static pressure. This design solution was applied to the CF2 gage.

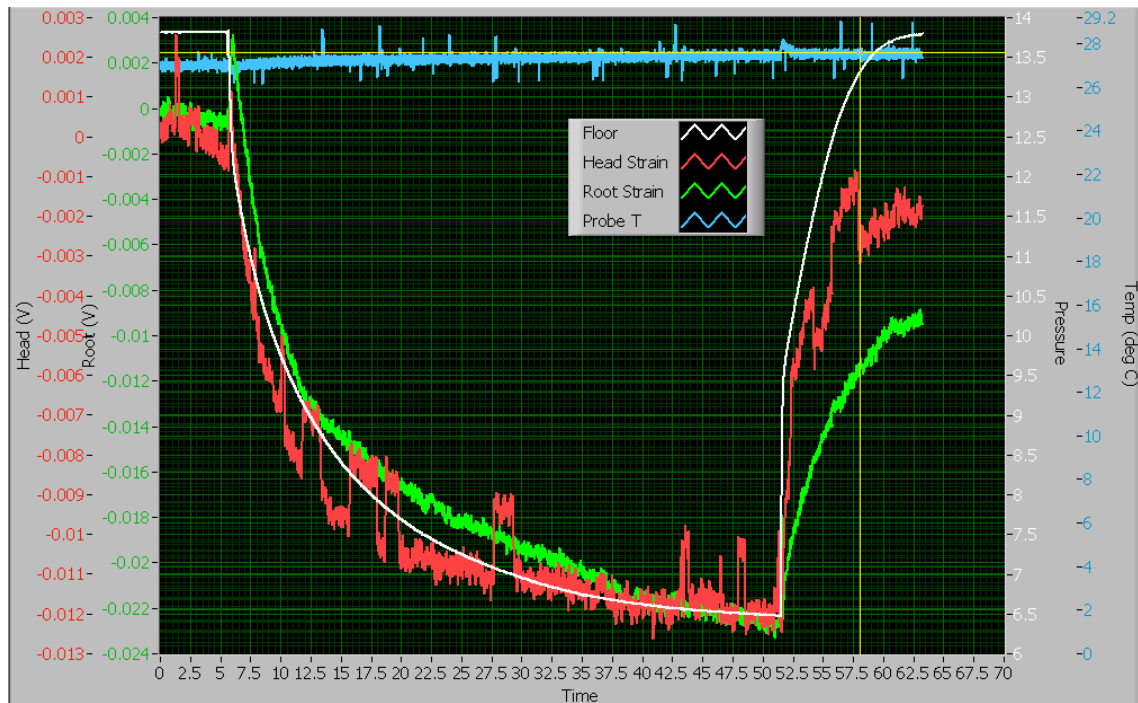


Figure 3-9. CF1 post experiment vacuum test.

CF1 Thermal Test

The changing static temperature measured during the experiment required examination. A temperature test was conducted with the CF1 and a thermocouple placed in a small oven where temperature conditions were well controlled. Both instruments were packed in ice and allowed to warm throughout the full test. Both the head and root voltages varied inversely with increasing temperature as shown in Figure 3-10. This is shown by the decreasing red and green traces represented by CF1 voltages. The thermocouple output is shown in blue. The high-lighted region of interest represents the temperature range encountered to the tunnel experiments.

This thermal test proved temperature was a source of apparent strain. The solution of the pressure problem by oil-fill posed a possible solution to the thermal issue. By filling the bellows cavity with oil, it was hoped that the temperature effect could be significantly reduced. This was the approach taken in developing CF2.

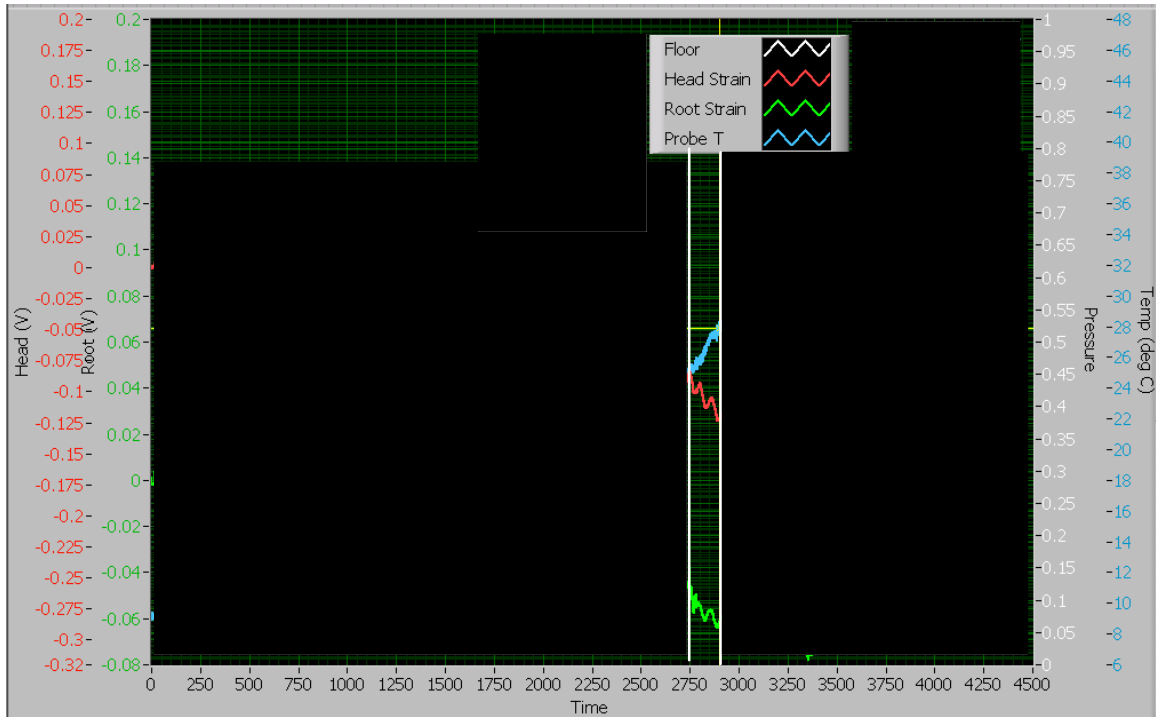


Figure 3-10. CF1 post experiment thermal test.

CF1 Wire Stiffening FEM

To illustrate the impact of wire placement on the overall strain output, examine Figure 3-11. The tension side shows high strain at the wire attachment points indicated by the gray and red contours. On the compression side figure, high compression strain develops at the wire attachment points indicated by the blue contours. Though the wires were small diameter, they were also short and stiff. The wire stiffness reduced the amount of strain that would normally be produced by τ_w . Calibration can reduce this as an issue in a small wall shear regime, where the wires act elastically. However, we want as much strain produced as possible at the strain gage location. Therefore, by moving the wires to the sides of the beam, they do not counteract the wall shear.

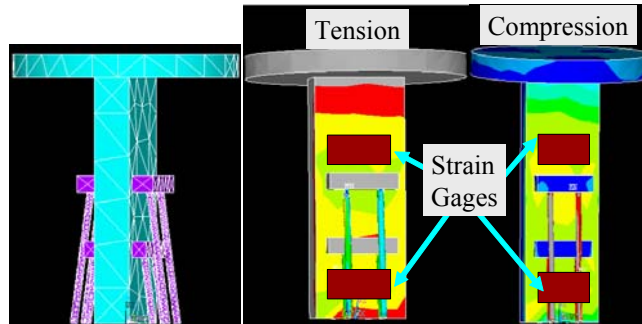


Figure 3-11. CF1 wire truss stiffening.

3.3 CF2 Gage Design

The CF2 design scheme was nearly identical to that of CF1. Several design changes were implemented. The focus was to eliminate strain due to uniform wall pressure. Application of an incompressible fluid within the bellows would not permit the beam to contract or elongate under uniform pressure load. Additionally, the oil benefit in diffusing thermal flux and increased damping were seen as side benefits. Therefore, oil-fill became the priority. Because of the geometry required to accommodate the needed Lee Plug®, a larger bellows, Servometer® FC-8, was chosen. This was the smallest bellows available for the oil configuration. Keeping the gage small was aimed to minimize inertial effects. As an aside, another technique for smaller bellows implementation with oil fill is proposed in the recommendations chapter. Returning to this discussion, the FC-8 bellows froze the head geometry. From the arguments presented for CF1, we stuck with the rectangular aluminum cross-section.

By using the same strain gages as the previous design, we removed R_G as a variable. As with the previous optimization, gap size, δ , and acceleration output, ϵ_a , and moment output, ϵ_{M_0} , were left for verification after optimization. Therefore we have narrowed our optimization variables to those in Table 3-3. The biggest difference between the CF1 optimization and this was the realization that the beam length could be varied below the limit of the bellows. This additional design variable meant we could vary the beam length, L , width, w , and thickness, th .

Table 3-3. CF2 state variables, objective functions, and design variables.

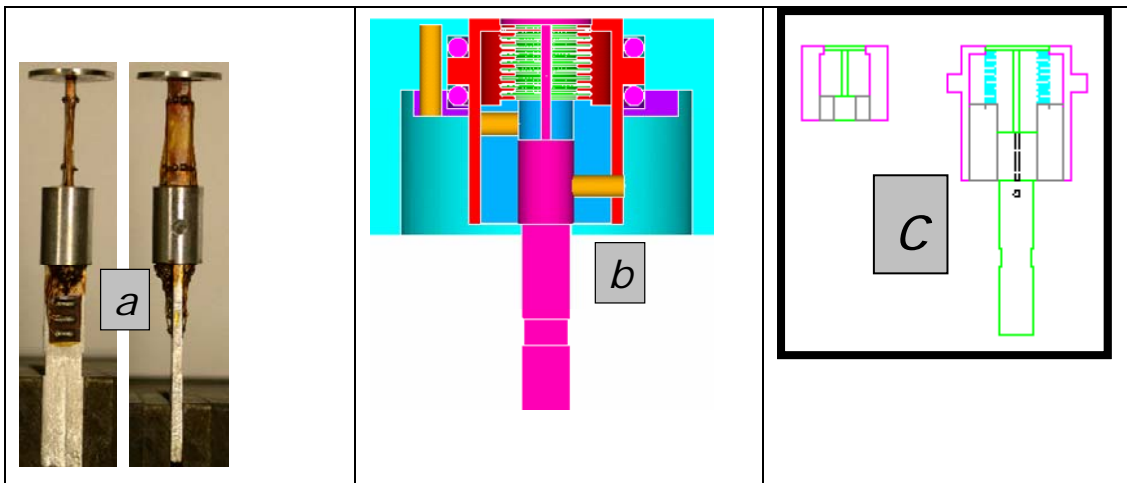
State Variables	Maximize	Minimize	Design
Strain due to Wall	ϵ_S	N/A	A_C, L
Frequency	ω_n	N/A	A_C, L

To limit the beam length and thickness, we recognized manufacturing limitations. After discussions with the shop, the beam length was set to 0.475 in. and the minimum thickness for the beam was set to 0.040 in. With these geometric constraints in place, we could vary the thickness to find the most strain output that still provided a minimal natural frequency. This turned out to be the minimum allowable thickness.

3.4 CF2 Results

The CF1 apparent strain investigation provided several design improvements to CF2. Once these design characteristics were applied, the gage was built, calibrated, and had separate test verifications in the Virginia Tech Supersonic Tunnel. Table 3-4 shows several stages of the CF2 assembly: a) element with strain gages b) 3-D rendered assembly and c) scaled drawing comparison against CF1.

Table 3-4. CF2 gage in stages.



Each CF2 Wheatstone half-bridge was completed with a Vishay® Model 2310 signal conditioner. These amplifiers were set using the 10 Hz low-pass Butterworth filter, a 5 V input voltage, and a 10k gain. A National Instruments® data acquisition

system was controlled by programs written in LabVIEW ®. The sample rate was 500 Hz. Prior to each test set, both 2310's were zeroed.

3.4.1 CF2 Calibration

The gage characterization required several calibration tests. After the testing calibration results from CF1, a calibration matrix was developed to determine sensitivity of gage performance to configuration. The three tested gage configurations were designated Baseline, Bellows, and Oil. Respectively, these configurations consist of the unshrouded element, element with base and bellows attached, and finally the oil-filled complete gage. The reason for calibrating the gage under these different configurations was to determine the effect of the bellows and oil on gage performance. As expected, there was little or no effect on static calibrations through the different configurations, but a significant effect during frequency characterization.

CF2 Static Wall Shear Calibration

The static wall shear calibration of CF2 was conducted exactly as with CF1. An example of such testing is shown in Figure 3-12. This particular photograph shows the calibration as conducted for the Baseline configuration. However, the results for the Oil or assembled configuration are presented in Figure 3-13. The results for both the head and root voltage output show high linearity with wall shear.

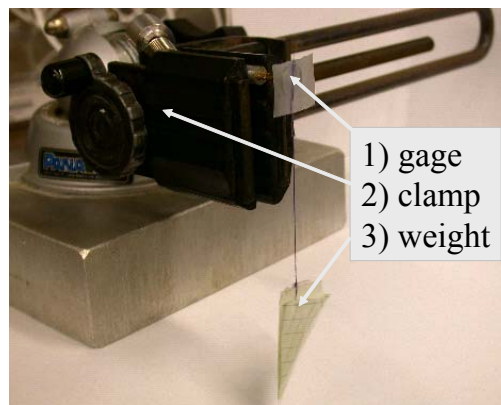


Figure 3-12. CF2 baseline static wall shear calibration setup.

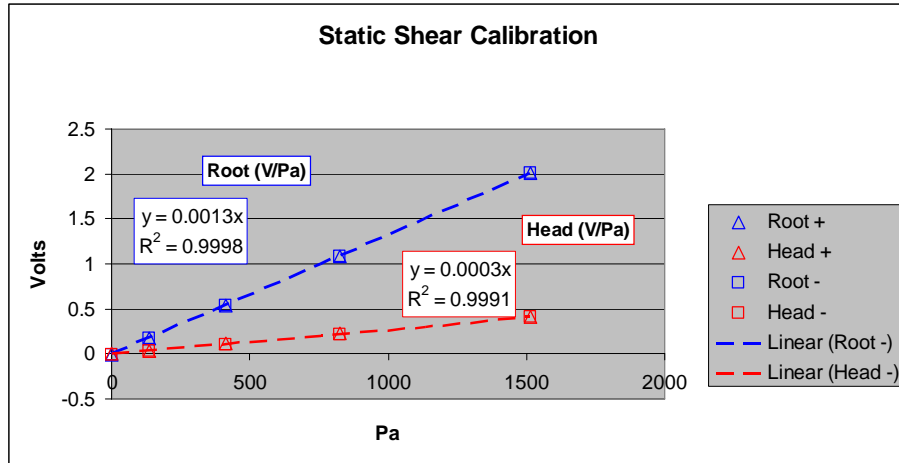


Figure 3-13. CF2 static wall shear calibration results.

CF2 Static Moment Calibration

The static moment calibration was conducted as presented for CF1. Figure 3-14 shows the set-up for the Baseline configuration calibration. The calibration curves for the head and root shown in Figure 3-15, meet expectations. Both curves are highly linear. Additionally, the proportionality constant for the head and root are nearly the same, within 7%, as expected with the constant strain distribution expected for a pure moment load.

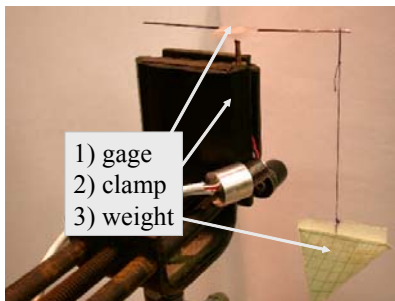


Figure 3-14. CF2 baseline static moment calibration setup.

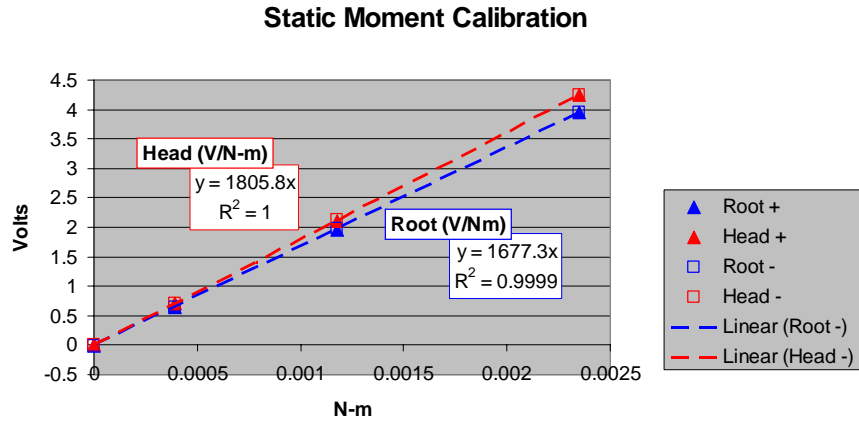


Figure 3-15. CF2 static moment calibration results.

CF2 Vacuum Test Calibration

The CF2 vacuum test was the most important calibration to ensure that our improved design eliminated the pressure problem of CF1. This particular calibration was only conducted on the assembled Oil configuration. Figure 3-16 shows the result of this calibration test. The white trace is the pressure transducer output throughout the test. The red and green traces are CF2 root and head output during the test. The test order was set with step 4 allowing us to check for leaks. Despite the small amount of noise observed throughout the test, neither set of voltage output shows signs of pressure reaction. This is especially obvious comparing the CF2 results to those of CF1. Therefore, this calibration test has successfully shown that a uniformly distributed pressure on the top surface of CF2 will not affect voltage output. This satisfied our most important design criteria in moving from CF1 to CF2.

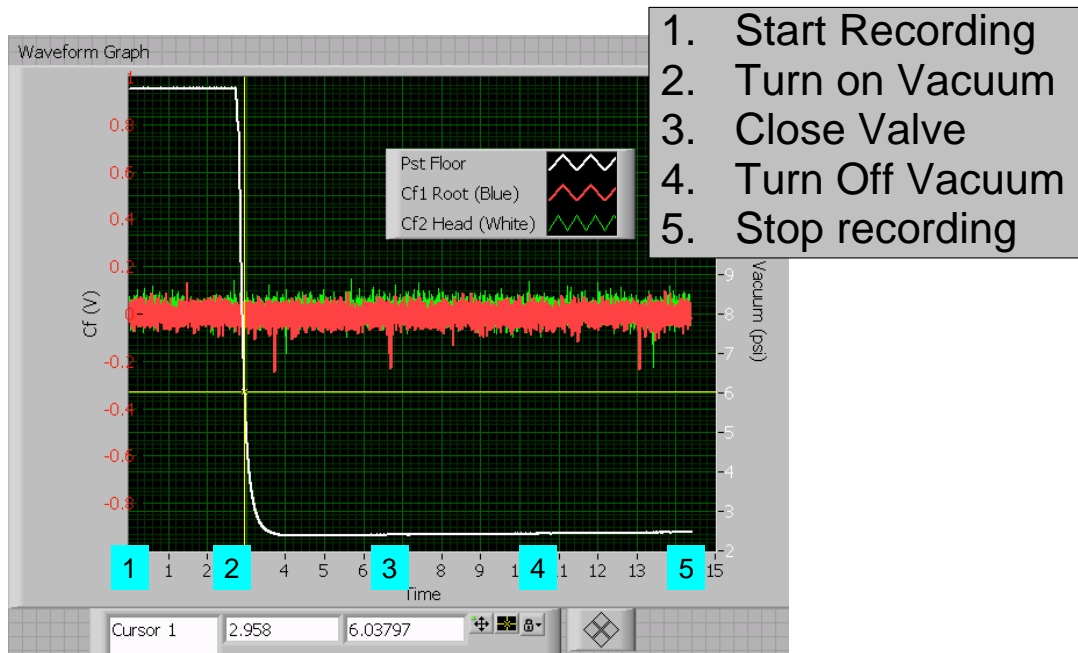


Figure 3-16. CF2 vacuum test calibration.

CF2 Thermal calibration

Several tests for thermal calibration were conducted. Cold and hot soaks as well as gradually varying temperature tests were conducted. Though all tests showed at least some transient periods of apparent thermal strain, no direct relationship between temperature and voltage output could be developed.

CF2 Dynamic response calibration

The dynamic response information we desire is the settling time. The method for test was a step-release. This test was conducted by tying a thread to the head of the gage, imparting a simulated axial wall shear, cutting the string, and measuring the natural response. A sketch of this process is shown in Figure 3-17. The CF2 gage was calibrated under three different configurations. The Baseline configuration is the simply the unshrouded element. The Bellows configuration has the bellows placed on the element, but not glued and without oil-fill. Finally, the Oil configuration is the full test configuration with oil fill.

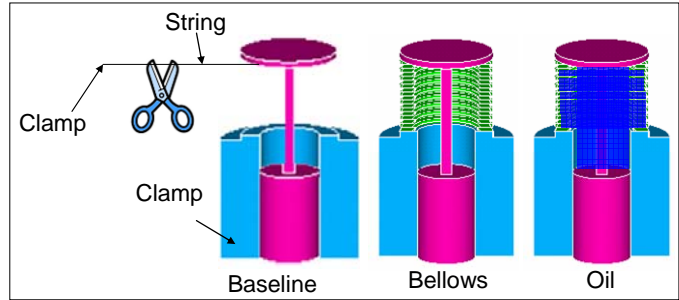


Figure 3-17. Dynamic response calibration setup.

Figure 3-18 shows the results of the string tests. These results are presented for quick reference in Table 3-5. Three configurations were measured for parametric analysis and FEM validation. First, from a parametric point of view, each case completely changes the dynamic response. Perhaps the most important characteristic for short duration testing is the settling time. For example, the CF2 Oil configuration will not settle in time to accurately measure τ_w during a 5 ms test run. The response of the bellows case should not be weighed too heavily since the components were not glued together, so chatter was an issue. The oil configuration also showed signs of second mode excitation. However, this does not present an issue in terms of determining settling time.

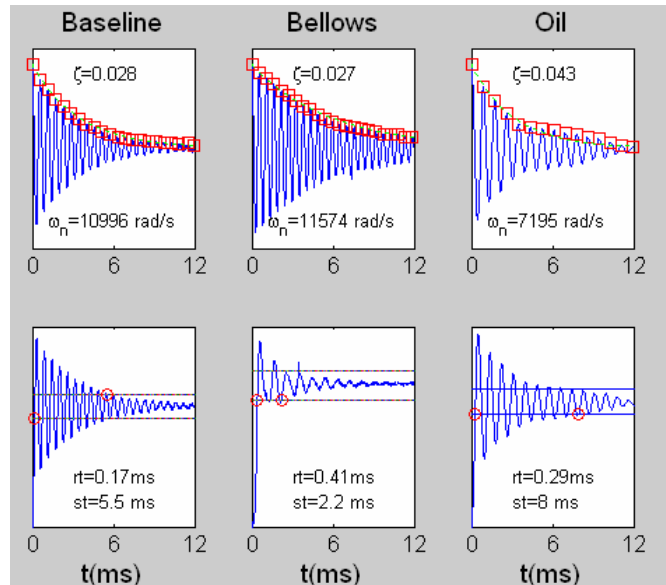


Figure 3-18. String test calibration data. Top row shows calculated ω_n and ζ . Bottom row shows measured rise and settling times for $\pm 10\%$ load.

Along with the presented rise and settling times, an estimation of vibrational frequency and damping coefficient for each configuration is given. These are not necessary in characterizing the CF2 dynamic response. They are critical, however, in providing a means for future modeling. For example, the oil configuration damping coefficient provides a reasonable estimate for future gage designs that use an FC-8 filled bellows. Therefore we can take this coefficient, a FEM determined vibration frequency, and make predictions of new gage settling times.

Table 3-5. CF2 vibration frequency calibration results.

	ω_n (rad/s)	ζ	Rise time(ms)	Settling time (ms)
Baseline	10996	0.028	0.17	5.5
Bellows	11574	0.027	0.41	2.2
Oil	7195	0.043	0.29	8

3.4.2 CF2 Virginia Tech Supersonic Tunnel Wall Shear Test

The CF2 gage validation testing was conducted in the Virginia Tech Supersonic Tunnel. Two test conditions were used: a pure wall shear test and a shock-impingement test. The total pressure set point was 1.03 MPa. The total temperature was atmospheric. Total pressure, (P_o), wall static pressure (P_{st}), and wall static temperature T_{st} , were measured along with the CF2 output.

Each CF2 Wheatstone bridge was completed with a Vishay® Model 2310 signal conditioner. These amplifiers were set using the 10 Hz low-pass Butterworth filter, a 5 V input voltage, and a 10k gain. A National Instruments ® data acquisition system was controlled by programs written in LabVIEW ®. The sample rate was 500 Hz.

Multiple validation tests were conducted for the pure wall shear case. Figure 3-19 shows the voltage output from each half-bridge during one such run. The red traces indicate output from the head half-bridge, near the top of the beam. The blue lines indicate traces from the root half-bridge, near the bottom. Dashed lines show the expected voltage output for the head and root for a pure 85 Pa wall shear, based on calibration. First, let's follow the root trace with time. The run begins without flow,

indicated by zero voltage output. After 5s, the tunnel starts as evidenced by the jump in voltage by the root bridge. Near 17 s, the tunnel pressure starts to drop, until it unstarts at 20s. The root voltage clearly indicates this by returning to zero. Throughout the test, the root output behaves very close to expectations.

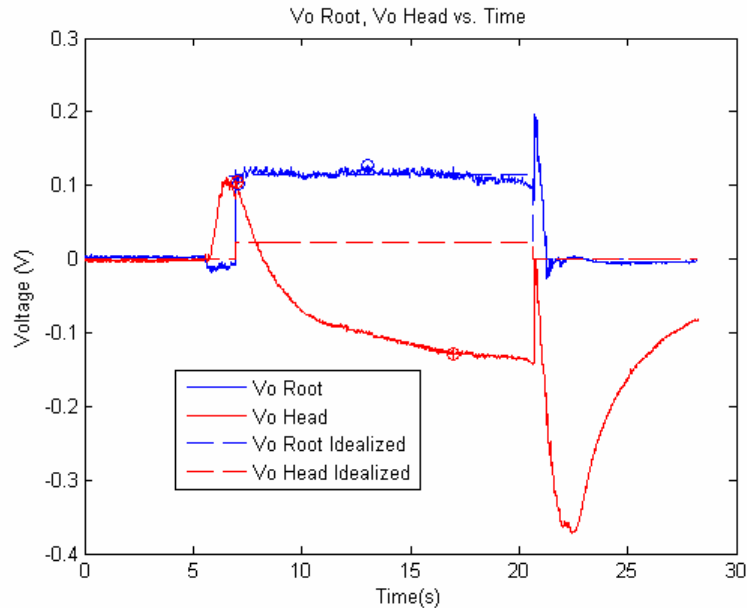


Figure 3-19. Pure wall shear results voltage output vs. time.

Turning our attention to the red, or head trace, we see that the voltage trends do not match our expectations. In fact, this output trends with temperature. This is best shown in Figure 3-20. In this figure, we see a relationship between the measured static temperature and the head bridge output voltage. Obviously, the temperature is a source of apparent strain for these test conditions. The relatively long tunnel start and test times allow for heat transfer through the gage head and down the beam. The first order time constant comparing the peak voltage and temperature is about 0.34 s. With the long test window, the gage has time to react to static temperature changes.

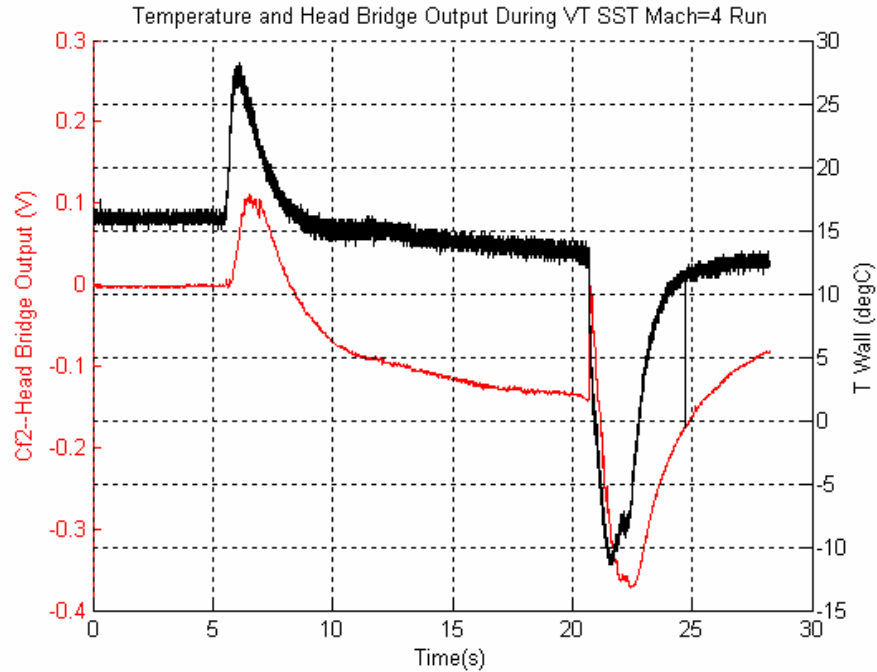


Figure 3-20. Comparison of CF2 head voltage and static temperature during M4 run.

Several methods of post-process temperature correction were considered and discarded. Rather than develop a temperature compensation method, which would require careful temperature measurements and physical considerations for each test case, a bounded solution method is developed. This method considers the full range of possible wall shear and moment solutions comparing test and calibration data. For the test case presented in Figure 3-19, we are only interested in the steady state conditions between 5 and 17 s. This window of interest is bound by the plus ‘+’ symbols. Within this region, the extrema for both root and head voltage are selected as bounds. These extrema are indicated by four circles. The solutions to Equations 2-3 and 2-4 provide corresponding moment and wall shear values for each of these circles. These solutions are shown in Figure 3-21 as points A, B, C, and D.

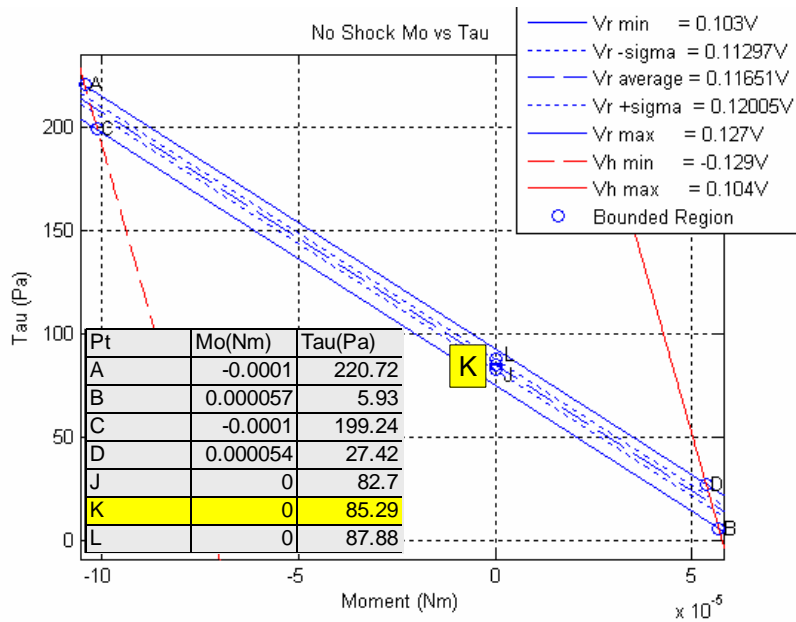


Figure 3-21. CF2 pure wall shear bound solution.

The solutions have been bound. From point A and B, the wall shear lies within the range of 6 to 220 Pa. This is obviously not useful. However, since we know the head output voltage is dominated by temperature effects, we can deduce that moment is minimal. With this knowledge, we can move to the point of the curve where moment is zero. Examining the single standard deviation solution at zero moment provides a very tight estimation for wall shear indicated by point K. This value is 85 Pa \pm 3 Pa. This solution fairly well matches predicted values for wall shear under these tunnel conditions in Table 1-3.

3.4.3 CF2 Virginia Tech Supersonic Tunnel Shock Impingement Test

A wedge validation test shadowgraph is superimposed on the test diagram in Figure 3-22. This image shows how an oblique shock impinges the top of the gage.

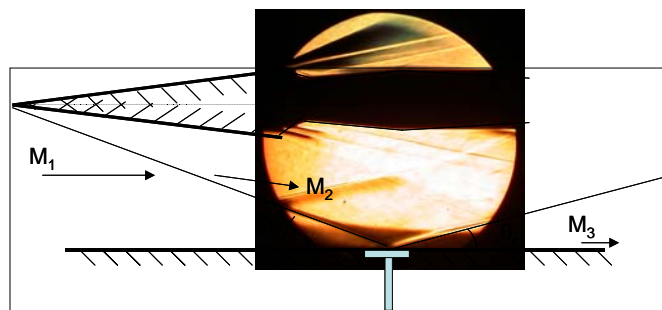


Figure 3-22. CF2 shock validation shadowgraph.

One set of CF2 results for this condition is shown in Figure 3-23. The root voltage output shown in blue exhibits similar behavior to that of the pure wall shear case. Though the head voltage output in red shows some trend with temperature, the signal is now dominated by moment.

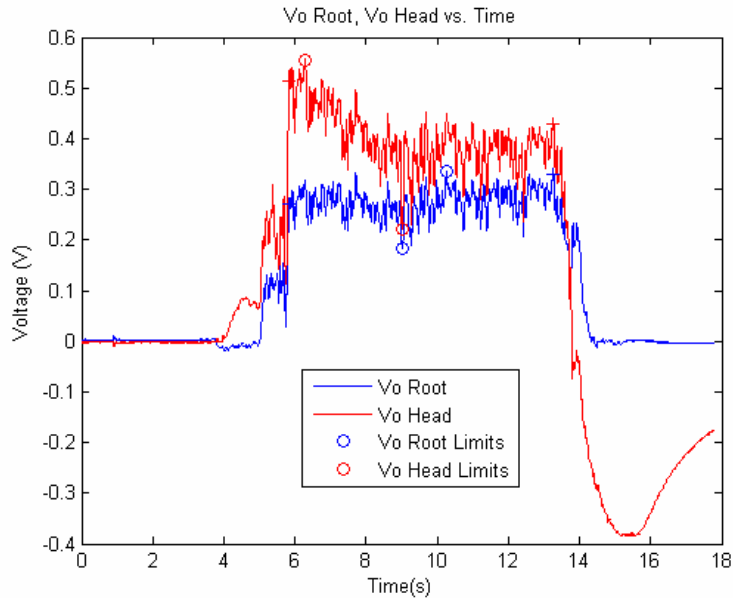


Figure 3-23. CF2 shock validation voltage output versus time.

The bounding applied to these output signals is presented in Figure 3-24. This time, the data was bound to the one-sigma solution. For example, the wall shear between points E and F ranged from -156 Pa to -13 Pa. The average at point I was -84 Pa. This negative range for wall shear suggests separation as might be expected in these conditions.

A significant part of these results is that the moment solution is bound between 0.0002 Nm and 0.0003 Nm. Comparing to our predicted value, this measurement is of the same sign and magnitude. For the first time using this new gage we can accurately state that the gage experienced a significant pressure differential across the head. Now combining this information with the measured negative wall shear, the experimentalist can conclude that a shock-impingement has caused a separation of the flow. No previous skin friction gage could do so. In fact, earlier direct measure gages under these same flow conditions would only indicate a large positive wall shear, exactly the wrong conclusion for these conditions. Therefore, this new gage design using separate half-

bridges to account for moment has proven its unique utility for these difficult flow environments.

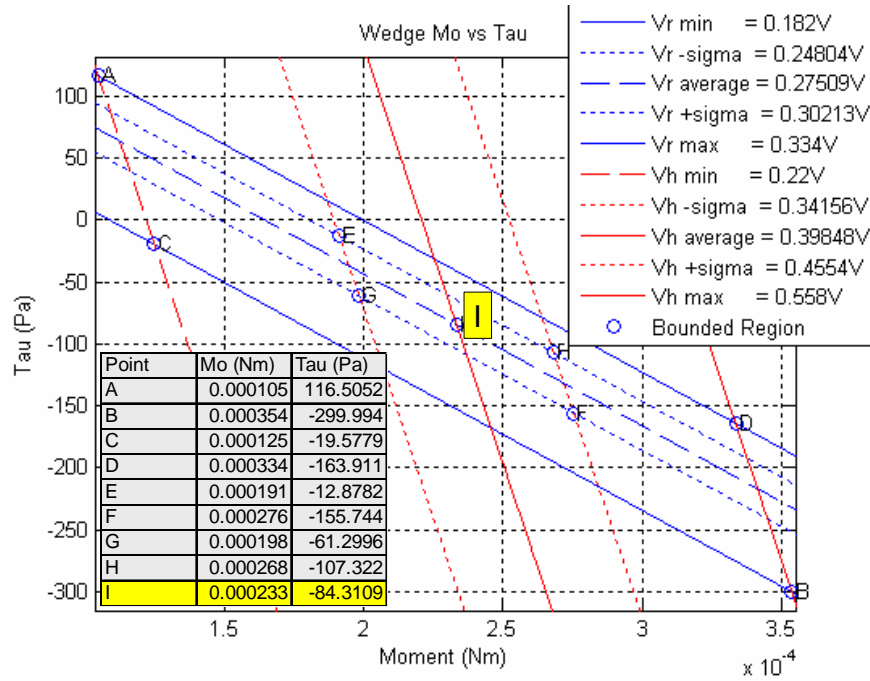


Figure 3-24. CF2 bound shock impingement solution.

4 Gage Characterization

After CF2 testing, we recognized the need to develop an encompassing design methodology. Up to this point, the designs have been developed through piecemeal investigations. This chapter builds the set of design techniques that will be used for optimization.

4.1 Model Results

In the Introduction, we specified a set of nominal load conditions in Table 1-4. This chapter develops the expected response of CF1 through CF4 to those conditions and establishes the fundamental models for optimization. Table 4-1 summarizes the results of this investigation. In the table, the analysis and model type for each load case is presented. For each gage the critical output parameters are listed. We will now examine how each of these parameters was calculated.

Table 4-1. CF1, CF2, CF3, and CF4 expected output to nominal loading.

Analysis Model	Load	Output	CF1	CF2	CF3	CF4
Static 3-D FEM	τ_w 2000 Pa	ε_τ ($\mu\varepsilon$) δ_τ (μm)	13.31 0.6	52.63 6.1	11.85 3.1	25.53 9.5
Static Calibrated	τ_w 2000 Pa	ε_τ ($\mu\varepsilon$)		49.3		
Static 3-D FEM	M=10 NS P1=500 Pa P3=58.25 kPa	M_o (mN-m) ε_{M_o} ($\mu\varepsilon$) δ_{M_o} (μm)	1.23 42.69 2.6	4.16 143.17 23.9	7.22 13.45 6.0	7.22 26.34 15.7
Static Calibrated	M=10 NS	ε_{M_o} ($\mu\varepsilon$)		132.7		
Static Calibrated	P_w 500 Pa	ε_p ($\mu\varepsilon$)	FAIL	0	0 Est.	0 Est.
Static Solid Mechanics	Acc 1g	τ_a (Pa) ε_a ($\mu\varepsilon$) τ_a / τ_w (%)	21.4 0.1 1.1	20.6 0.6 1.0	181.1 0.8 9.1	75.0 0.5 3.7
Thermal 3-D FEM	\dot{q}_w 100 (kW/m ²)	ΔT (K) ε_T ($\mu\varepsilon$)	4 96	3 72	<1 1.3	1 24
Dynamic Axi FEM	f (Hz)	f (Hz) ω_n (rad/s) Est. ζ	3569.9 22430 0.027	1133.4 7121 0.043	1052.8 6615 0.043	1030.1 6472 0.043
Dynamic Laplace	Step Load	Rise (ms) Settle (ms)	0.2 3.6	0.2 7.5	0.2 7.9	0.2 8.0
Dynamic Calibrated	Step Load	Rise (ms) Settle (ms)		0.29 8.0		

The response of each gage depends on its geometry and material. A generalized sketch of the fundamental geometries is shown in Figure 4-1. Table 4-2 lists each gage's corresponding fundamental measurements. Critical structural material properties are listed in Table 4-3. Critical thermal material properties are listed in Table 4-4. A quick reference for important solid mechanics equations is provided in Table 4-5. Finally, the relevant instrumentation for each gage is shown in Table 4-6.

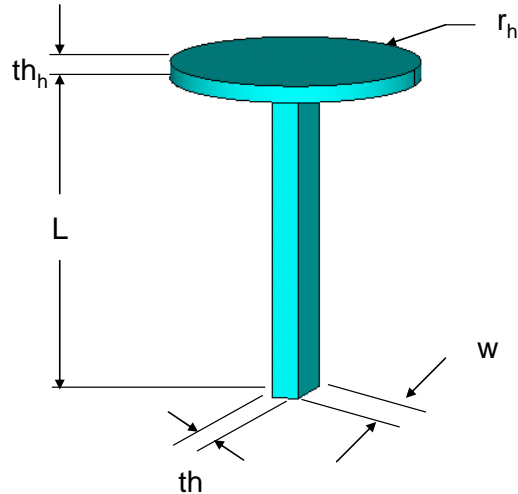


Figure 4-1. Geometric parameters.

Table 4-2. Geometric quick reference.

		CF1	CF2	CF3	CF4
Material		Aluminum	Aluminum	INVAR	Aluminum
Head	r_h	3.175E-3 m	4.7625E-3 m	5.725E-3 m	5.725E-3 m
	th_h	6.35E-4 m	6.35E-4 m	1.27E-3 m	1.27E-3 m
Beam	w	2.54E-3 m	2.54E-3 m	3.048E-3 m	3.048E-3 m
	th	1.016E-3 m	1.016E-3 m	2.703E-3 m	3.048E-3 m
	L	6.858E-3 m	1.206E-2 m	3.139E-2 m	3.962E-2 m

Table 4-3. Structural material properties reference.²³

Material Properties	Aluminum	Nickel	INVAR
Tensile Modulus E (Pa)	7.00 E 10	2.07 E 11	1.48 E 11
Density ρ (kg/m ³)	2700	8880	8050
Poisson's Ratio ν (m/m)	0.33	0.31	0.23
Coefficient of Thermal Expansion CTE ($\mu\text{m/mK}$)	24	N/A	1.3

Table 4-4. Thermal material properties reference.²⁴

	Al	Nickel	Invar	Oil	Air
Thermal Conductivity k (W/mK)	210	60.7	10.15	0.138	0.026
Specific Heat c_p (J/kgK)	900	460	515	1670	1000
Thermal Diffusivity α (m^2/s)	8.6 E-5	1.5 E-5	2.4 E-6	1.0 E-7	2.23 E-5

Table 4-5. Solid mechanics equations.²⁵

Geometry	Mass	Equivalent Acceleration Shear
$L_{tot} = L + th_h$ $A_h = \pi \cdot r_h^2$ $A_c = w \cdot th$ $I = w \cdot th^3 / 12$ $arm = \frac{4}{3\pi} r_h$	$m_h = A_h th_h \rho$ $m_b = A_c L_{tot} \rho$	$\tau_a = \frac{\left[m_h \left(L_{tot} - \frac{th}{2} \right) + m_b \frac{L}{2} \right] a}{L_{tot} A_h}$

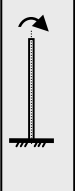
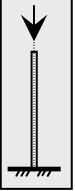
Table 4-6. Gage components and instrumentation.^{26,27}

	CF1	CF2	CF3	CF4
Servometer ® Bellows	FC-3-L	FC-8-L	FC-8-L	FC-8-L
Wheatstone Bridge	2 Half	2 Half	TBD	TBD
Vishay Strain Gage	EA-13-031-CE-350	EA-13-031-CE-350	TBD	TBD
R_G	$350.0 \pm 0.2\%$	$350.0 \pm 0.2\%$	TBD	TBD
GF	$2.11 \pm 1.0\%$	$2.11 \pm 1.0\%$	TBD	TBD
Vishay 2310 Gain	10 k	10 k	TBD	TBD
Filter	10 Hz (VT)	10 Hz (VT)	TBD	TBD
V_{in}	5 V	5 V	TBD	TBD

4.2 Static Response

The first analysis type is static. In this case, we ignore whether the load is stepped, ramped, or time-varying and only treat the steady state case. The loads of interest are wall shear, moment, acceleration, and pressure. Each of these will be addressed in turn. The analytic cantilever beam solutions provide a good sanity check for more complicated models. The cantilever beam static solutions are presented in Table 4-7.

Table 4-7. Cantilever beam static load solutions.

Surface Load	 $\tau_w=2000 \text{ Pa}$	 $P_1=500 \text{ Pa}$ $P_3= 58250 \text{ Pa}$	 $P_w=500 \text{ Pa}$	1g
Equation ²⁸	$M_\tau = \tau_w A_h L_{tot}$ $\sigma_\tau = \frac{M_\tau \cdot th}{2I}$ $\varepsilon_\tau = \frac{\sigma_\tau}{E}$ $\delta = \frac{\tau_w A_h L_{tot}}{3EI}$	$M_o = \frac{2(P_3 - P_1)r_h^3}{3}$ $\sigma_{Mo} = \frac{M_o \cdot th}{2I}$ $\varepsilon_{Mo} = \frac{\sigma_{Mo}}{E}$ $\delta_{Mo} = \frac{M_o L_{tot}^2}{2EI}$	$\sigma_{Pw} = P_w$ $\varepsilon_{Pw} = \frac{\sigma_{Pw}}{E}$	Wall Shear Equations
Output	$\varepsilon_\tau (\mu\varepsilon)$ $\delta_\tau (\mu\text{m})$	$\varepsilon_{Mo} (\mu\varepsilon)$ $\delta_{Mo} (\mu\text{m})$	$\varepsilon_{Pw} (10^{-3} \mu\varepsilon)$	$\tau_a (\text{Pa})$ $\varepsilon_a (\mu\varepsilon)$
CF1	9.9 0.4	25.6 1.4	4.5	22.9 0.1
CF2	59.2 6.3	136.0 21.6	7.1	21.9 0.6
CF3	8.8 2.3	9.4 3.7	2.4	193.6 0.8
CF4	12.1 4.4	10.3 5.7	3.4	79.0 0.5

4.2.1 Static Wall Shear

The first load for consideration is the nominal 2000 Pa static wall shear. Because we are interested in the strain distribution on the surface, a full 3-D finite element model (FEM) is required, and the commercial FEM Code ANSYS[®] was used for this and other purposes.²⁹ We will use CF2 as a case study since calibration data is available. The finite element model uses the Solid 92 element, which is a 3-D, 10-node structural tetrahedral with three degrees of freedom, i.e. displacement in each Cartesian direction: u_x , u_y , and u_z . The beam bottom surface nodes were held to zero displacement. The wall shear was evenly distributed across the top surface. The free mesh was produced using ANSYS smart meshing set to 6, which produced 1,366 nodes. The meshed model and nodal solution are shown in Figure 4-2.

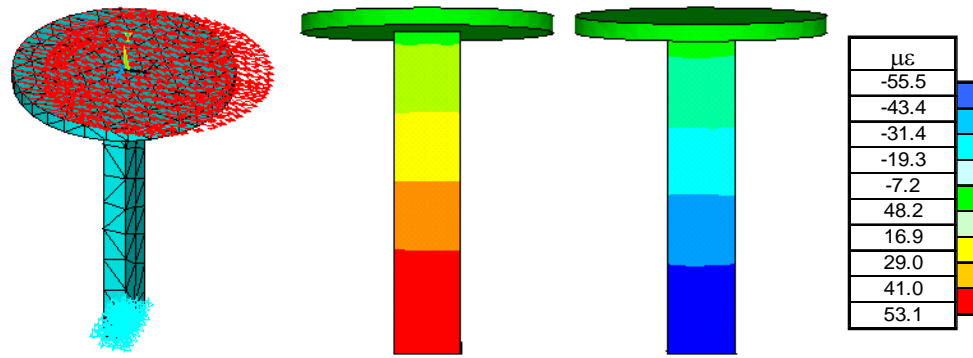


Figure 4-2. CF2 3-D FEM result for 2000 Pa wall shear.

Table 4-8 presents the Voltage-Pascal ratios for the root and head from static wall shear calibration. These are the quantities c_{11} and c_{21} for Equations 2-3 and 2-4. Assuming ideal instrumentation, we can back out the expected microstrain for this load using Equation 3-1. The manufacturer published gage factor is 2.11, and the 2310 Signal conditioner is set with Gain=10,000 and $V_{in}=5$ V. From this we expect to see a strain of 49.3 $\mu\epsilon$ at the root, positive for the tension side and negative for compression side.

$$\epsilon = \frac{2 \cdot V_o}{V_{in} \cdot GF \cdot Gain} \quad \text{Equation 4-1}$$

We expected the maximum strain calculated using ANSYS to be higher than from the actual gage. This is because each strain gage measures the strain over a relative large area compared to the point of maximum strain. The fact that our model is within 10% of the measured strain is good. It shows that strain gages were well placed during fabrication. It also gives confidence in the modeling technique.

Table 4-8. Expected CF2 output to 200 Pa wall shear.

Facility	Root	Head	Variation from Ideal
Calibration Factors	0.0013 V/Pa	0.0003 V/Pa	
Output for 2000 Pa	2.6 V	0.6 V	
Ideal Bridge	49.3 $\mu\epsilon$	11.4 $\mu\epsilon$	0 %
Cantilever Beam	59.2 $\mu\epsilon$	N/A	20 %
3-D FEM	52.6 $\mu\epsilon$	N/A	6.7 %

4.2.2 Static Moment

The next load for consideration is a severe Mach 10 normal shock impinging on the center of the gage head which for CF2 yields a 0.00416 N-m moment. Again, because we are interested in the strain distribution on the strain gage attachment surfaces, we have to use a full 3-D finite element model. We continue with the CF2 as a case study, since calibration data is available. The finite element model uses the same Solid 92 element. The beam bottom surface nodes were held to zero displacement. The moment load was applied as an axially varying pressure load distributed across the top surface. The free mesh was produced using ANSYS smart meshing set to 6, which produced 1,366 nodes. The meshed model and nodal solution are shown in Figure 4-3.

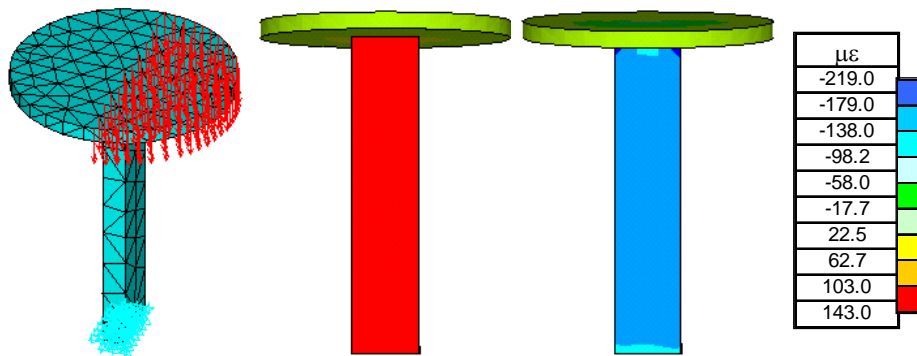


Figure 4-3. CF2 3-D FEM result for impinging Mach 10 normal shock.

Table 4-9. Expected CF2 output to a Mach 10 normal shock.

Facility	Root	Head	Variation
Calibration Factors	1677 V/N-m	1806 V/N-m	
Output due to M10 NS	7.0 V	7.5 V	
Ideal Bridge	132.7 $\mu\epsilon$	142.2 $\mu\epsilon$	0 %
Cantilever Beam	136.0 $\mu\epsilon$		2.5 %
3-D FEM	143.17 $\mu\epsilon$		7.9 %

Table 4-9 presents the resulting Voltage-Pascal ratios for the root and head from static moment calibration. These quantities are c_{12} and c_{22} from Equations 2-3 and 2-4. Assuming ideal instrumentation, we can back out the expected microstrain for this load using Equation 3-1 with previous settings. From this we expect to see a strain of 132.7 $\mu\epsilon$ at the root, positive for the tension side and negative for compression side. The

ANSYS calculated maximum strain should be higher than from the actual gage. Again the strain gage covers more area. Even so, the model is still within 10% of the measured strain.

4.2.3 Inertia Loading

The last load for consideration is inertia. This is accomplished by calculating an equivalent acceleration shear due to inertia, τ_a . The development of this calculation is shown graphically in Figure 4-4. In this equation, a is the measure of acceleration in m/s^2 . Our nominal maximum acceleration is 1-g or $9.8 m/s^2$. By applying τ_a to the beam surface, we achieve the same strain output near the base of the beam as caused by inertia. Because the gage is performing within the elastic region we can simply apply the ratio τ_a/τ_w to the strain output for the pure wall shear case. As an example, should CF2 experience a 1-g acceleration and 2000 Pa wall shear, it would see a relative strain due to inertia of $21.4/2000 \epsilon_{\tau}$, or about $0.1 \mu\epsilon$.

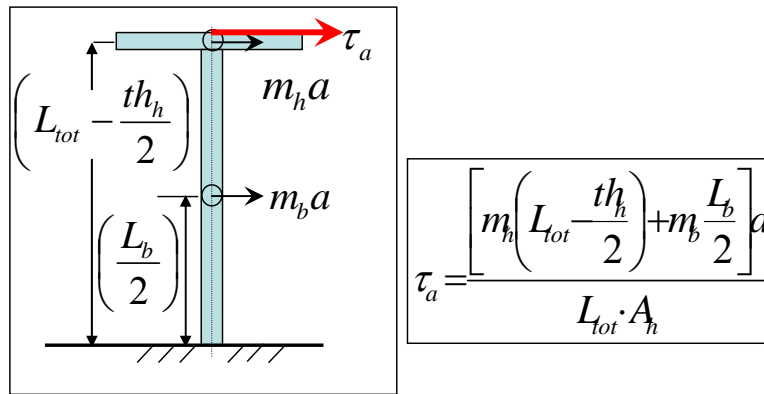


Figure 4-4. Calculation for equivalent inertial shear.

4.2.4 Static Pressure

The gage design using incompressible fluid filler in the bellows eliminates uniform wall pressure as a source of strain. A vacuum test calibration of the oil-filled CF2 proved that there is no voltage output due to changing uniform pressure. Therefore, for our model considerations, uniform pressure loading on CF2, CF3, and CF4 is assumed to produce zero microstrain output. The CF1 case failed to eliminate uniform

wall pressure as a variable. Therefore, pressure is an indeterminate source of apparent strain for CF1.

4.3 Dynamic Response

When you first step on a scale in the bathroom, it bounces around and finally settles on your weight. This under-damped second order system response is similar to what happens with these direct measure gages. They are under-damped, which means they oscillate with an exponential decay toward a steady load value. In order to characterize how these gages respond, we really want to know how long the gage takes to get within $\pm 10\%$ of the steady value. This is called the gage settling time. In order to determine this key gage parameter, we must look at two aspects of dynamic response. First, we need to characterize each gage's dynamic coefficients: natural frequency, ω_n , and damping ratio, ζ . Second we have to develop solutions to the ordinary differential equations for our different expected loads cast as forcing functions.³⁰

4.3.1 Vibrational Frequency

The first model for verification is 1st mode bending response. We continue the trend of employing CF2 due to its available calibration data. However, in this case, we use a poor approximation of just the gage beam without the head. This way we can find some useful relations for finite element modeling. The natural frequency of just the beam is calculated using the analytic solution for a clamp-free simple cantilever beam. Table 4-10 shows the clamp-free response of this simple cantilever beam. Additionally, the table provides a means to calculate dimensions for a cylindrical beam of equivalent natural frequency. Now we can test whether this equivalent cylindrical beam provides reasonable output for a variety of finite element models.

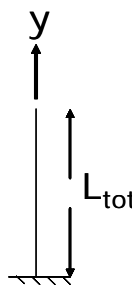
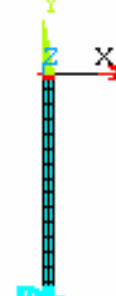
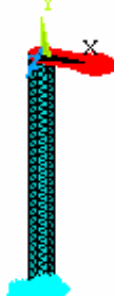
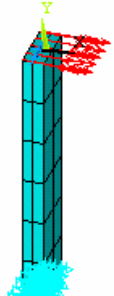
Several finite element models are developed to match the proposed rectangular aluminum beam. These are presented in Table 4-11. Clearly, these models well match the theoretical result. All of the models are within 2% of the theoretical result which verifies the coding technique applied in ANSYS. The axisymmetric case checked well against the 3-D circular model. The axisymmetric model is important because it provides

an accurate solution for vibration frequency with a greatly reduced number of elements compared to the full 3-D case.

Table 4-10. Cantilever beam solution for 1st mode bending response.

Governing Equation ³¹	Axisymmetric Radius ³²	Output
$\omega_i = \frac{\lambda_i^2}{L_{tot}^2} \sqrt{\left(\frac{EI}{\rho A_c}\right)}$ $\lambda_1 = 1.8751047$	$\omega_{block} = \omega_{cylinder}$ $\sqrt{\frac{w \cdot th^3}{12 \cdot w \cdot th}} = \sqrt{\frac{\pi \cdot r^4}{4\pi \cdot r^2}}$ $r_{eq} = \sqrt{1/3th}$	$f = 5182.1 \text{ Hz}$ $\omega_n = 32,560 \text{ rad/s}$ $r_{eq} = 5.87E-4 \text{ m}$

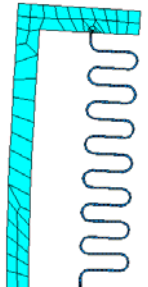
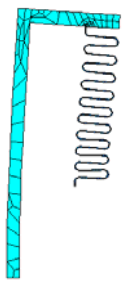
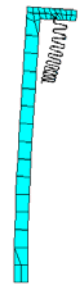
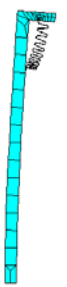
Table 4-11. Comparison of several FEMs to cantilever theory for 1st mode bending.

		1-D FEM	Axi-Harmonic	3-D Cylinder	3-D Block
ANSYS Element Type	Beam Theory	Beam3	Plane83	Solid186 Mopt Pyra	Solid186
Model					
f(Hz)	5,182.1	5,175.3	5183.9	5187.5	5248.6
ω_n (rad/s)	32,560	32,517	32,571	32,594	32,978
Variation		0.1%	-0.0%	-0.1%	-1.3%

Now that we know the axisymmetric finite element model is sufficient to determine natural frequency, we can develop accurate, but computationally small models for the real gages. The axisymmetric model allows us to model the full beam and bellows. The ANSYS element used for this analysis was the Plane 83. This axiharmonic element is simply an axisymmetric element on which non-axisymmetric loads may be applied. For example, to model a surface wall shear, the mode is set to 1,1 and the load is applied as $f_x = \tau_w$ and $f_z = -\tau_w$. The meshed model and first mode bending shape are shown in

Table 4-12. The measured vibration frequency for the CF2 gage is included. We can see that the finite element model performs well, predicting the response to 1.0 %. The damping coefficient for CF2 comes directly from measurement Figure 3-18. This data was used to make assumptions about the damping coefficient for each of the other gages. CF1 has lower damping since it lacks oil-fill.

Table 4-12. Natural frequency output for each gage.

	CF1	CF2	CF3	CF4
Axiharmonic FEM				
Node count	1215	1982	1922	1925
ζ	0.027	0.043	0.043	0.043
f(Hz)	3569.9	1133.4	1052.8	1030.1
ω_n (rad/s)	22,430	7121	6615	6472
Calibration		7195 rad/s		
Variation		1.0 %		

4.3.2 Step Load

We've already stated that this gage exhibits second order system response. Equation 4-2 is the governing 2nd order linear non-homogeneous ODE. This equation shows how the system will move in the x-direction given a time-varying forcing function, $F(t)$, and two separate initial conditions. If we divide through by mass, we get a familiar form with $c=2\zeta\omega_n$ and $k=\omega_n^2$, where ζ is the damping factor and ω_n is the circular frequency in rad/s.³³ In order to verify our models, we use $\omega_n = 7195$ rad/s and $\zeta = 0.043$ for the CF2 gage. For a step wall shear input, a Laplace transform time domain solution is shown in Equation 4-4.

$$M\ddot{x} + C\dot{x} + Kx = F(t)$$

Equation 4-2³⁴

$$\ddot{x} + c\dot{x} + kx = f(t)$$

Equation 4-3

$$x(t) = u - ue^{-\zeta\omega_n t} \left(\frac{\zeta}{\sqrt{1-\zeta^2}} \sin(\omega_n \sqrt{1-\zeta^2} t) + \cos(\omega_n \sqrt{1-\zeta^2} t) \right) \quad \text{Equation 4-4}^{35}$$

The transform solution is compared with the calibration data for the oil-filled CF2 in Figure 4-5. The transformation solution overshoots the peak value achieved during experiment. Since we are using a transformation model for optimization, this allows a conservative estimate for the maximum displacement. In other words, we will automatically design a gap size that will accommodate the overshoot without railing.

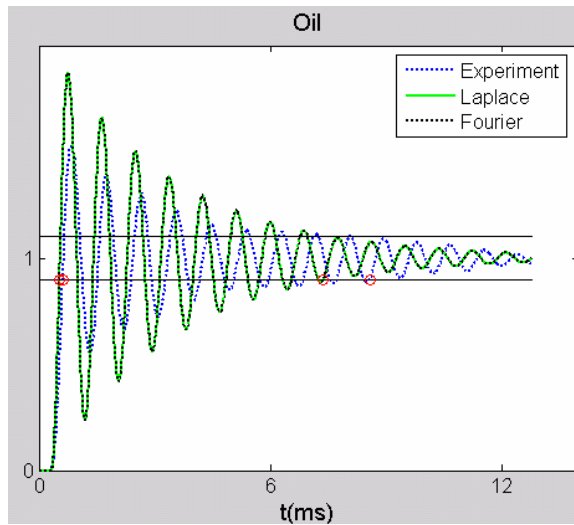


Figure 4-5. CF2 step load response. Comparison between calibration data and transformation solutions.

Unfortunately, the model under predicts the signal rise time, but more critically, the settling time. This must be accounted for when choosing a minimum vibration frequency for settling time. The full parameters are presented in Table 4-13. Conservatively, we can apply an 85% design factor to the total run time to ensure the gage settles as desired.

Now that we have a good method to determine the rise and settling time using the Laplace transform solution, we can characterize the dynamic response of each gage. Figure 4-6 shows the expected dynamic response for each of our gages using the coefficients from Table 4-12. Clearly the CF1 gage settles the quickest just from quick observation. The numerical results for rise and settling time for each gage are listed as well. Clearly all gages will settle sufficiently to make an accurate measurement within 10 ms.

Table 4-13. CF2 Validation data.

	Experiment	Laplace	Variation	Safety Factor
Rise Time	0.000299	0.000208	30.4 %	
Settling Time	0.008268	0.007059	14.6 %	0.85 (min test time)
Peak Value	1.535	1.872	-22 %	2 (max τ_w static)

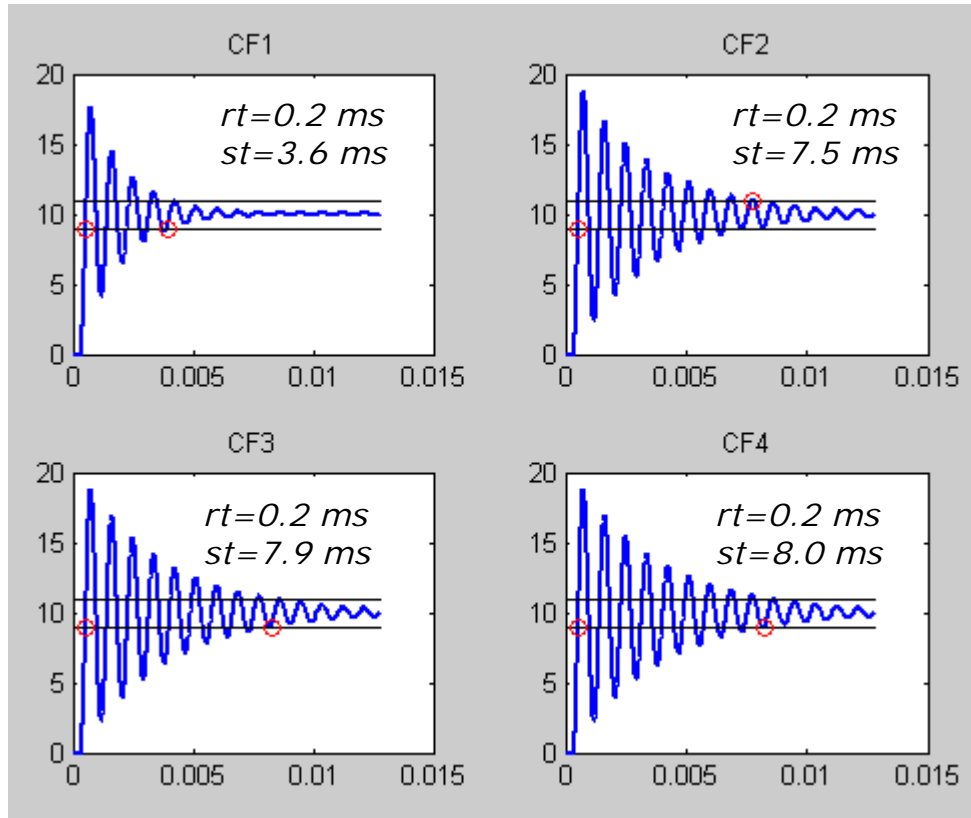


Figure 4-6. Dynamic response to step load.

4.4 Thermal Response

The thermal response requires a transient analysis. Because of the interaction of the gage, oil, and air, a 3-D finite element model is used. Additionally, because of the effect of surrounding material, such as a floor plate, a larger model is developed for each gage. We assume the heat flux load of 100 kW/m^2 acts on the gage prior to achieving steady state during a test run. We must account for these transient effects, such as tunnel start for example. This is done by applying the heat flux for a full 0.1 s instead of just the 10 ms steady state time.

The ANSYS element type for this model is the Solid 98, which is a 3-D, 10-node tetrahedral. The element is set to only allow one degree of freedom, temperature. As an additional check on potential thermal gradients, the heat flux is varied axially across the surface of the model. The nominal load is applied at axial centerline. The leading edge is 2.5% greater, and the trailing edge is 2.5% lower. This variation of 5% across the model surface mimics boundary layer growth and allows us to investigate temperature variations through the beam thickness. Figure 4-7 shows the applied spatially varying heat flux loads for each model.

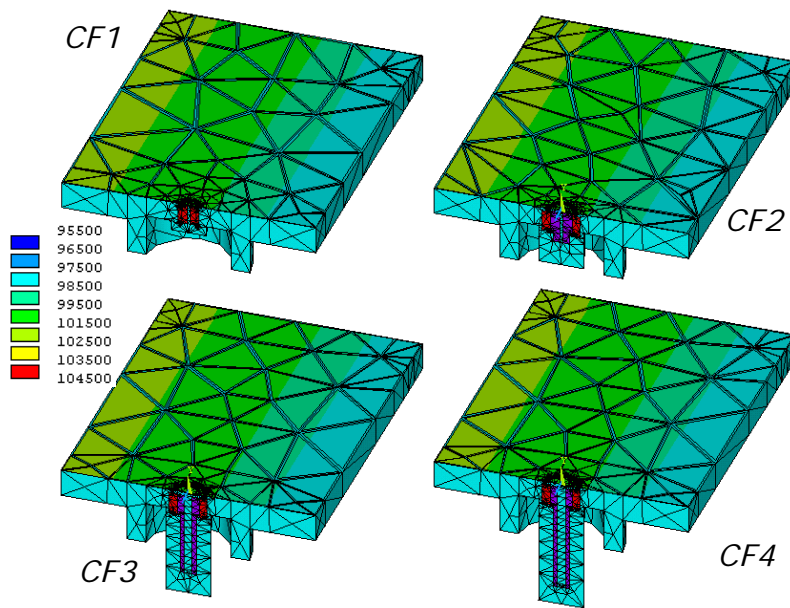


Figure 4-7. 5% spatially varying heat flux, nominal 100 kW/m².

The top left image shows the CF1 model. The smart mesh option of 10 yielded 3512 elements. The top right image shows the CF2 model. The smart mesh 10 option yielded 3906 elements. The bottom left model shows the CF3 gage in an INVAR plate. The smart mesh 9 option for this model produced 9368 elements. Finally, the bottom right image shows the CF4 gage. The smart mesh 9 option produced 14,734 elements. All models had an initial temperature of 289 K.

Performing the transient analysis for 0.1 s produced the thermal distributions shown in Figure 4-8. The arrows for CF1 and CF2 point to the approximate vertical location of the head strain gages. We can see that this particular set of gages experience a relatively high amount of temperature gradient due to this nominal load. Looking at the

CF3 and CF4 gages, we see large regions where little temperature change occurs. Strain gages placed within this region should experience little apparent thermal strain.

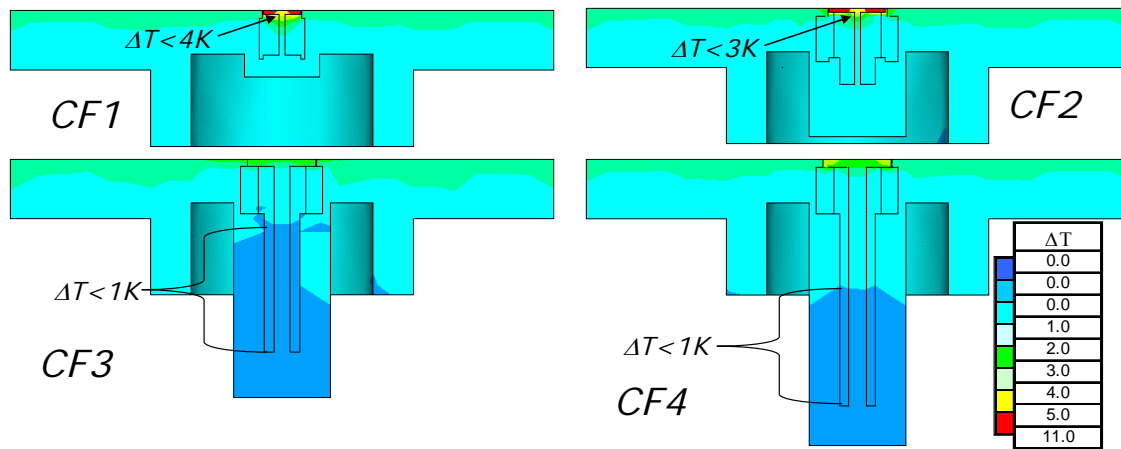


Figure 4-8. Temperature distribution 100 kW/m² for 0.1 s.

In order to quantify the amount of strain experienced at these locations, the simple formula $\epsilon_T = CTE \cdot \Delta T$ is applied.³⁶ The small thermal expansion coefficient for INVAR makes a large impact on expected thermal strain due to temperature. The compiled results for the expected response at the ‘head’ gage are supplied in Table 4-14. The term ‘head’ is placed in quotes to emphasize the new lower location on CF3 and CF4.

Please recall that if both sides of the beam see the same strain output, we should get a net voltage output of 0V. However, for arguments sake, if the beam temperature varies 5% from front to back, this produces a measured 5% $\Delta\epsilon$ across the bridge, and it produces a proportional voltage output. In order to grasp that effect, the amount of thermal strain produced from a 5% variation is also shown in Table 4-14.

Table 4-14. Expected strain output at ‘head’ due to nominal heat flux.

	CF1	CF2	CF3	CF4
ΔT	4K	3K	<1K	<1K
ϵ_T	96 $\mu\epsilon$	72 $\mu\epsilon$	1.3 $\mu\epsilon$	24 $\mu\epsilon$
Assumed 5% $\Delta\epsilon_T$	4.8 $\mu\epsilon$	3.6 $\mu\epsilon$	0.1 $\mu\epsilon$	1.2 $\mu\epsilon$

4.5 Combined Response

The measure of success for CF1 through CF4 is how well each meets specifications. The design load conditions are presented here again in Table 4-15. This time we've added the additional complexity of spatially varying heat flux examined in the last section. Given these load conditions, how close does each of these gages come to measuring the 2000 Pa wall shear?

Table 4-15. Nominal design loads

	Time (ms)	τ_{wx} (Pa)	a_x (g)	$\dot{q}_w(x)$ (kW/m ²)
Load	10	2000	1	100

Figure 4-9 shows the expected magnitude of strain from these nominal loads assuming a 5% thermal strain output. In general we see that in all cases, the signal is dominated by shear strain, which is a good thing. Though CF1 has been removed from contention due to pressure effects, we see that it would have suffered due to thermal strain. The other gages have relatively small amounts of thermal strain. As expected the INVAR, CF3 gage, performs exceptionally in limiting apparent strain due to thermal gradient. CF2-CF4 experience relatively small amounts of apparent strain. Even in the case of CF3, which has a proportionately large amount of inertial strain, it produces less than 10% of the total strain output.

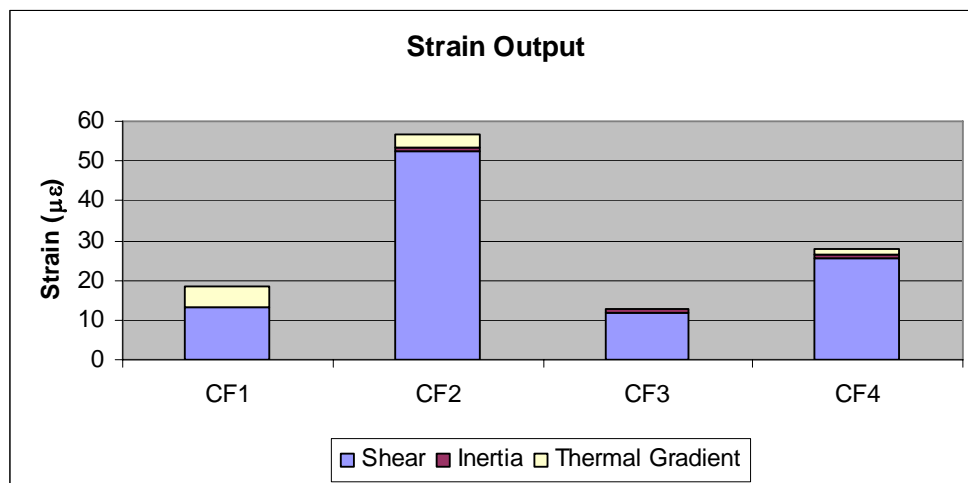


Figure 4-9. Strain magnitudes due to nominal wall shear.

In order to quantify these sources of strain, we look at the relative magnitude percentage of strain over the strain from just wall shear. This is shown in Table 4-16. This table shows that CF2, CF3, and CF4 should have reasonably small apparent strain under our nominal load. CF1 clearly would have had significant thermal issues. For the optimized gages, apparent strain provides less than 10 % of signal output.

Table 4-16. Relative magnitude of strain output.

	$ \epsilon_a/\epsilon_\tau $	$ \epsilon_T/\epsilon_\tau $	$ \epsilon_a/\epsilon_{tot} $	$ \epsilon_T/\epsilon_{tot} $
CF1	1%	36%	1%	26%
CF2	1%	7%	1%	6%
CF3	9%	1%	8%	1%
CF4	4%	5%	3%	4%

In order to understand how these sources of strain affect the output signal, we have to consider whether the strain is positive or negative. In the case of inertia, we know that it opposes the motion induced by wall shear. Therefore for simplicity if we consider the tension side of the beam, we expect to have a positive strain from wall shear and a negative strain from inertia. The apparent thermal strain could be positive or negative. Now we can band our expected output signal for each gage due to the nominal load conditions. This is done in Figure 4-10.

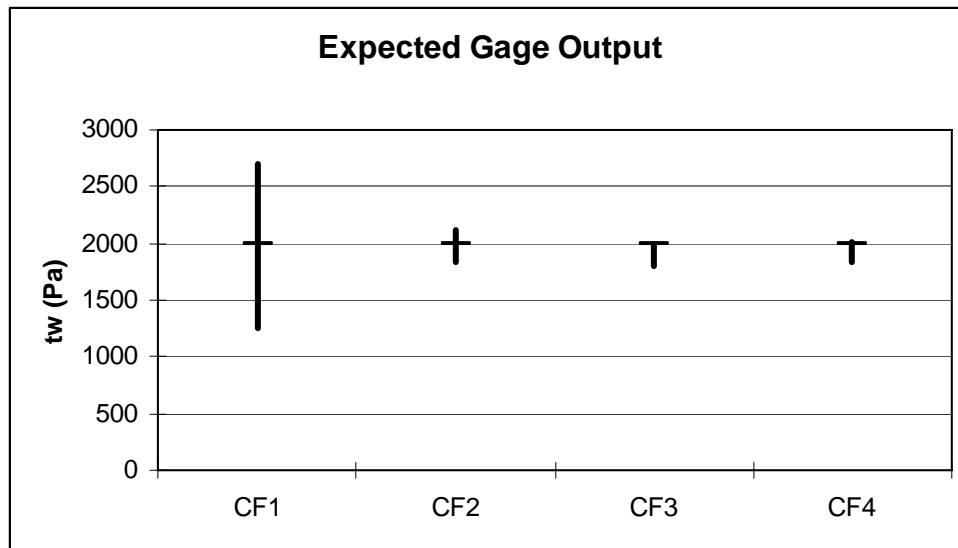


Figure 4-10. Expected output for nominal conditions.

The lighter gages, CF1 and CF2, have an uncertainty band that is spread almost equally about the true value. The heavier gages are likely to indicate a lower value of wall shear than is actually measured due to inertia. The expected output values are in Table 4-17.

Table 4-17. Output measurements to nominal load case.

	Low (Pa)	$\frac{2000 - Low}{2000}$	High (Pa)	$\frac{2000 - High}{2000}$	Mean (Pa)
CF1	1257	37 %	2700	-35 %	1979
CF2	1843	8 %	2116	-6 %	1979
CF3	1808	10 %	1830	9 %	1819
CF4	1831	8 %	2019	-1 %	1925

An experimentalist using one of these gages can limit uncertainty due to acceleration. This is accomplished by measuring acceleration during testing of the base model with an accelerometer. The most conservative approach is to multiply the maximum measured acceleration by the coefficient in Table 4-18. This provides the output (Pa) that should be added to the wall shear measured. As an example using CF3, a maximum 1 g acceleration of 9.8 m/s² is multiplied by the 19.74 kg/m² acceleration coefficient. This yields a 193.6 Pa correction that should be added to the raw wall shear measurement.

Table 4-18. Accelerometer employment with direct measure gages.

	CF1	CF2	CF3	CF4
Acceleration Coefficient (kg/m ²)	2.33	2.23	19.74	8.05
1g equivalent shear (Pa)	22.9	21.9	193.6	79.0

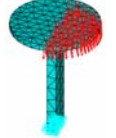
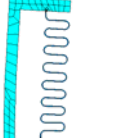
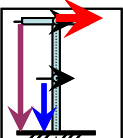
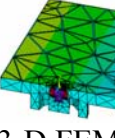
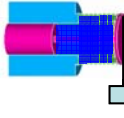
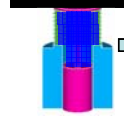
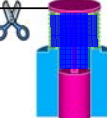
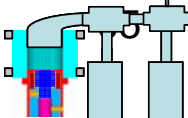
4.6 Gage Characterization Techniques

This section summarizes the selected gage characterization techniques. These are the simplest available modeling techniques that accurately predict gage response. In the case of displacement, simpler techniques could suffice, except this parameter is already available after examining the full 3-D FEM for corresponding strain. Table 4-19 shows the selected model techniques, output, and calibration method for verification.

This table captures the critical parameters for direct skin friction gage design. The five sources of strain are each examined: τ_w , M_o , ΔT , a , and P_w . Wall pressure is not modeled since through vacuum calibration, it has been eliminated as a source of output voltage. The final parameter to be determined for gage performance is settling time. If we assume a damping coefficient, we can estimate the gage dynamic response by applying a FEM predicted vibrational frequency.

The output parameters of interest are listed. There are five strains of interest: ϵ_τ , ϵ_{M_o} , ϵ_a , $\epsilon_{\Delta T}$, and ϵ_{P_w} . As with wall pressure, the corresponding strain is neglected. Normally, we would look at the corresponding displacements for each of these strains. However, we are only interested in displacement in terms of impact on gap size. Therefore, we ignore pressure and thermal induced displacements since they do not act in a way to impact gap sizing. Acceleration displacement is not considered for two reasons. First, wall shear effect on gap size is much greater than acceleration by design. This is because we want small relative displacement due to acceleration. Second, acceleration opposes wall shear, so it actually decreases the necessary gap. Thus our displacements of interest have been narrowed to just two: δ_τ and δ_{M_o} .

Table 4-19. Gage characterization summary.

Input	τ_w	M_o	1 st mode excitation	τ_a	\dot{q}_w	P_w
Model	 3-D FEM	 3-D FEM	 Axi FEM Estimate	 Mechanics	 3-D FEM	N/A
Output	ϵ_τ δ_τ	ϵ_{M_o} δ_{M_o}	ω_n ζ (Est.)	ϵ_a	$\epsilon_{\Delta T}$	0 V
Verification					T_{st}	

The last output parameters considered are necessary to determine the gage settling time. Since we are designing within a family of gages, all using oil-filled bellows and of similar dimensions, an estimate for damping coefficient is made from CF2 dynamic

calibration data. This estimated constant of $\zeta=0.043$ actually requires no further modeling. With this parameter established, we only need to determine expected vibrational frequency, ω_n .

Finally, the table shows the verification techniques for each model. The static wall shear, moment, and natural frequency calibrations showed good agreement with FEM for CF2. The vacuum test showed that wall pressure changes did not produce voltage output for CF2. Static temperature measurements during testing ensure correct heat flux modeling. This point will be thoroughly investigated in Chapter 6: Simulations and also shows good agreement for CF2 testing. The equivalent acceleration can be verified through a combination of static wall shear calibration and accelerometer measuring. For design purposes, we assume the solid mechanics model is accurate.

5 Optimization

During each design, the gage geometry and material properties were parametrically varied within constraints to achieve desired performance. The geometry and material properties made up the design variables. The output variables such as strains, frequencies, and displacements were state variables that could be cast as objective functions. An objective function is designed to be minimized. As an example, we would like to minimize the difference between our maximum strain output and the proportional strain limit while staying below this limit. Over several gage iterations, from CF1 through CF4, the number of state variables considered increased as well as the sophistication of the design approach. This reflected the understanding of the physical complexity of the environmental interaction of the flow, gage, and measurement devices. It also illustrated that load conditions substantially change the design of direct measure gages. The optimization applied in developing CF3 and CF4 fully constrained the design space and represents a true optimization scheme considering all design and state variables.

The robustness of the optimization approach developed in this chapter allows it to be applied to several design scenarios. Some nominal conditions for three very different test conditions are presented in Table 5-1. Here we see conditions for a high-enthalpy short duration test condition such as LENS. Next come the longer, lower wall shear blow-down facility conditions. Finally, the design conditions for a typical flight test are presented. The optimization approach will be applied to each of these conditions.

Table 5-1 Test regimes for gage optimization.

Test Conditions	Settle time	F (Hz)	τ_w (Pa)	a_x m/s ²	\dot{q}_w kW/m ²	M_o Nm
Shock (High Enthalpy)	10 ms	1000	2000	9.8	100	0.00722
Blow Down	1 s	10	85	0.098	-5	0.00118
Flight	1 s	10	2000	9.8	100	0.00118

5.1 Optimization for Short Duration High Enthalpy Testing

The first test condition to consider is the familiar nominal condition investigated in Chapter 4: Gage Characterization. One added complication is the possibility of trying to measure a lower wall shear of 1000 Pa. The optimization approach will be applied to develop an INVAR design, CF3, and an aluminum design, CF4.

5.1.1 CF3 Gage Design

After achieving a gage that detects shock impingement, CF2, there was a desire to greatly reduce the impact of thermal output from the upper half-bridge in the pure wall shear testing in the VT supersonic tunnel. As discussed in the modeling section, the thermal-strain effect was considered a possible source of error. By turning our attention to a material with low thermal expansion characteristics, we hoped to greatly reduce or eliminate this effect. Figure 5-1 shows some various configurations and the resulting temperature distribution for expected LENS heat flux. Although polyethersulfone was considered, the requirement to switch to semi-conductor strain gages made this material a poor candidate. Thermal strain is hard enough to deal with in the linear regime. Semi-conductor strain gages have expansion rates that are non-linearly related to the substrate. Therefore, we chose INVAR which has a low coefficient of thermal expansion.

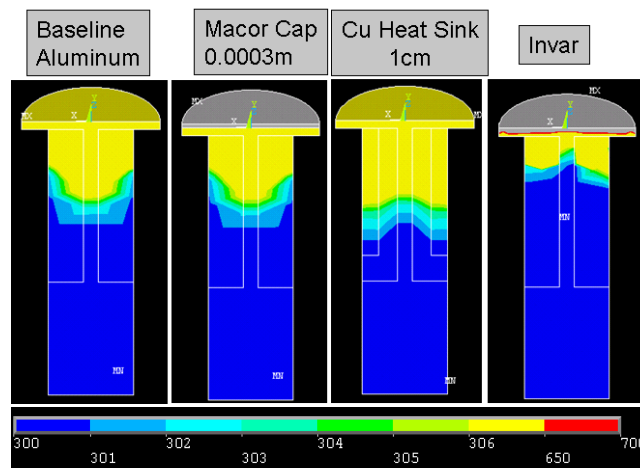


Figure 5-1. Thermal analysis for temperature gradient at LENS. FEM using 100 kW/m^2 for 0.1 s.

Along with the material change, an oil leak problem required a geometric change. Initially, we considered TIG welding or soldering the bellows to the head and base of the

gage. After further consultation with our machinists, we decided to enlarge the head and add a groove to seat the bellows in epoxy at the head and base. This increased the gage head thickness and diameter. This obviously penalizes us in terms of allowable inertial loading, but solving the thermal-mechanical problem has taken priority in this design.

Finally, we wanted the flexibility to use a full Wheatstone bridge configuration at both the “head” and root locations. As shown in the theoretical development, this allows for further temperature compensation at the “head” and root of the beam. Even using the smallest available commercial gages Vishay ® EA-00-015LA-120, we still limited the minimum design width to 0.12 in. Notice that the “head” location has been moved considerably further down the beam away from the flow in Figure 2-8. This is done to avoid thermal gradients, hence the quotes.

So in general the new design has many features to address the thermal-strain and leaking problems, but has greatly increased the overall size and weight of the gage and raised the CG. Table 5-2 shows the combined impact of the design changes prior to optimization. First, we see that the increased density will impact the head and beam weight. The beam width puts a 20% penalty on weight. The head of CF3 is nearly 9 times heavier than that of CF2. This also pushes the center of gravity higher. All of these design changes have a detrimental impact on acceptable inertial loading. All of these variations show the impact of designing with thermal-strain considerations at the forefront.

Table 5-2. Design feature impact on size. Comparison between CF2 and CF3.

	CF2	CF3	Change
Density (kg/m ³)	2700	8050	3 x increase
Beam width (in)	0.1	0.12	1.2x increase
Head thickness (in)	0.025	0.05	2 x increase
Head diameter (in)	0.375	0.4508	1.2x increase
Head volume (m ³)	4.53E-8	1.31E-7	2.9x increase
Head mass (kg)	1.22E-4	1.05E-3	8.6x increase

Despite the acceleration limitation, we can still design a CF3 gage that achieves all of our test design objectives. In order to determine those objectives, we need to settle on reasonable test conditions. This gage design is for LENS facilities. Unfortunately, the

variation in flow conditions across these facilities is rather extreme. These conditions considered are presented in Table 5-3. After discussion with the LENS personnel, we decided to build a gage that could meet all of the LENS I and LENS II requirements. This meant being able to settle within 10 ms and measure a 1000 Pa wall shear, without having problems under the higher load condition. This will be examined in considerable detail as we examine each state variable. This effectively means we are designing for three loading conditions: Case 1) $\tau_{wmin}=1000$ Pa Case 2) $\tau_{wmax}=2000$ Pa and Case 3) M=10 shock impingement. Although extreme, the shock impingement conditions are set with P1=500 Pa and normal shock acting at the center of the gage head. This way we know the gage will work under less stringent but more realistic impingement conditions.

Table 5-3. Test conditions for consideration for CF3.

	Time	τ_w	Max Acc (g's)	Max Mom
LENS I	10 ms	1000 Pa	1	M10 NS
LENS II	50 ms	2000 Pa	1	M10 NS
LENS 48 in.	5 ms	150 Pa	1	M10 NS
VT SST	12 s	85 Pa	0	M3.7 NS

Now that load conditions have been established, we can begin to narrow the design space. We start with the geometric constraints on the design variables. From the previous gages we see that the three design variables are beam length, thickness, and width. By choosing the FC-8 bellows and our full bridge gage configuration, we have effectively frozen the design width to 0.12 in. This has eliminated a design variable. The two remaining variables are constrained by the FC8 bellows, manufacturing, and a reasonable maximum on beam length. This has considerably narrowed our overall design space. These constrained conditions are presented in Table 5-4.

Table 5-4. CF3 design variable constraints.

	Min (m)	Min (in)		Max (in)	Max (m)	
Strain gages	0.003048	0.12	w	0.12	0.003048	FC8 Bellows ID
Manufacturing	0.000254	0.01	th	0.12	0.003048	FC8 Bellows ID
FC8 + Lee Plug	0.012065	0.475	L	2	0.0508	Model space

The physical design space can now be shown graphically. Figure 5-2 shows the range of possible designs in two ways. First, on the left, we see the four extremes. For example, the top left gage is the shortest-thinnest possible beam, while the bottom right shows the longest-thickest possible beam. This same space is expressed in a different way with the figure on the right. In this case, the largest, thickest beam is split in half. Then the range of geometrically allowable thickness and length are each divided into 25 steps. In other words, each of the 625 “pixels” represents a completely different gage design. As we look down the rows, the gages get longer. Going from left to right, the gages get thicker. The entire discretized space represents our geometrically constrained design space. This concept is very important and will be the driving picture to understanding the total optimization procedure.

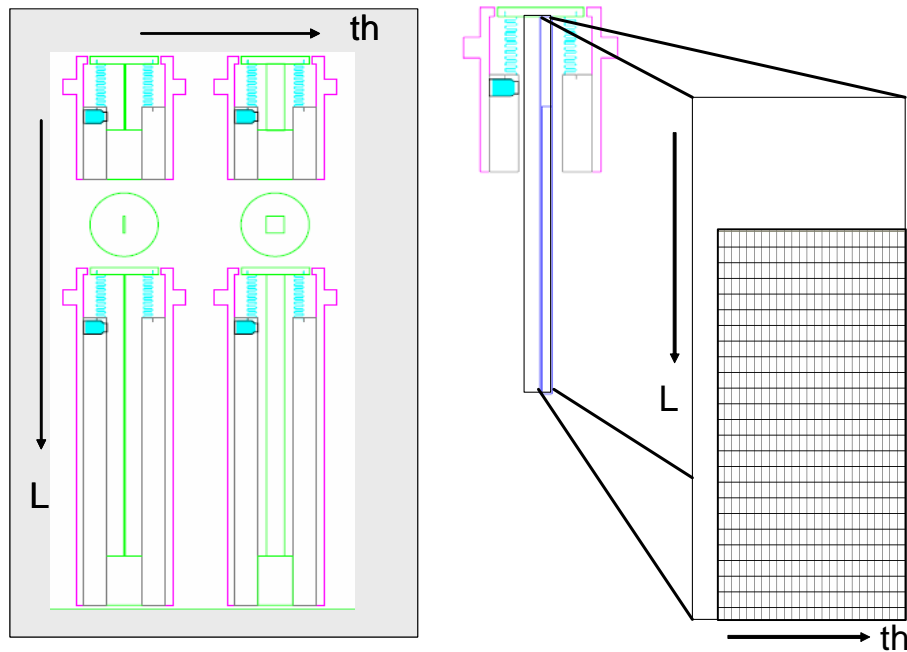


Figure 5-2. CF3 geometrically constrained design space.

Now that we have successfully constrained and discretized the design space, we need to constrain the state variables. We start with seven state variables: ω_n and ζ , ε , δ , m and cg , and ΔT . The first two make up the first mode shape response of the gage. Since we are still using an FC-8 oil-filled gage, we can reasonably assume that the damping coefficient should remain around 0.043. The output strain and displacement are self-explanatory. The mass and center of gravity of the gage help define how it will react

to inertia. Since we are interested in keeping the magnitude of this response low compared to the wall shear output, we will calculate an equivalent inertial shear based on maximum g-loading. Finally, the ΔT is the change in Celsius for the top set of strain gages. Thus, with these adjustments, we have simplified our problem to five state variables: f , ϵ , δ , τ_a , ΔT . Next we must constrain these variables.

We can start with the time constraint on minimum natural frequency required. Since our minimum run time is 10 ms, we must ensure that the gage will settle within that time. Figure 5-3 shows that a 1000 Hz gage will meet that requirement by settling within 8.5 ms. Thus we can safely design a gage with a minimum 1000 Hz natural frequency to overcome transient effects. There is no maximum on natural frequency, so we move to the next state variable.

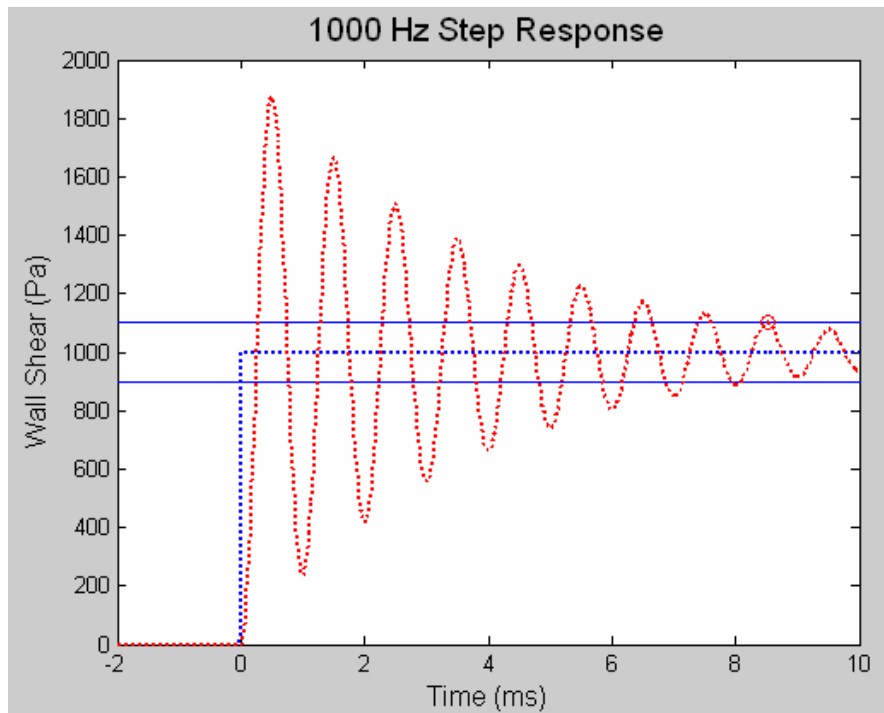


Figure 5-3. 8.5 ms settling time for 1000 Hz gage for 10 ms test run.

The next state variable for consideration, ϵ , must be examined against each of the three different load cases of interest. The gage must produce some minimal strain output even under the minimum wall shear of 1000 Pa. Therefore, we set that minimum to $0.5 \mu\epsilon$ for this condition. This is very low, but provides a reasonable start point. All of the analysis of the gage assumes that it operates within the proportional limit of the material.

For INVAR, that limit is about 1.18E11 Pa. Therefore, we cannot exceed this limit even during overshoot transient conditions for our worst load conditions, Case 2 and Case 3. Since the overshoot is just under twice the step response, we can safely check both conditions using twice the expected step load.

The displacement, δ , has no minimum. However, to keep the gap size to a minimum, we set this distance to a maximum of 0.005 in. To ensure that the head does not touch the housing even during the overshoot conditions of Cases 2 and 3, we must check the displacement under twice these load conditions.

Since each pixel represents a new gage design, there are 625 different total masses and center of gravity locations. These properties will be converted to calculate an equivalent wall shear based on a 1 g inertial loading. This technique was presented in gage characterization. This equivalent acceleration shear magnitude can be compared to our $\tau_{w \min} = 1000$ Pa. Since we have greatly increased the overall size and density of the gage, we set the maximum τ_a to 25% of $\tau_{w \min}$ or 250 Pa.

The final state variable for consideration is the temperature variation at the top set of strain gages, ΔT . Based on the resulting output from the VT testing, we decided that we wanted to keep the temperature change at this set of strain gages below 1 deg C. This particular variable requires longer FEM run times for analysis, so will be examined for the final design selected. Intuitively by making the beam length longer and thicker, more diffusion can be achieved. This will play in choosing the final design dimensions. The constrained state variables are presented in Table 5-5. Now we can begin the careful process of examining how each of the 625 gage designs responds to each of our load conditions.

The optimization process uses four separate sweeps of all 625 designs. First the axisymmetric bellows model is used to determine first mode natural frequency. Second, a 3-D model is used to determine the maximum ϵ_y and maximum δ_x due to a 2000 Pa load. Third, a 3-D model is used to determine the maximum ϵ_y and maximum δ_x due to the worst case moment load condition of a Mach 10 normal shock impinging on the center of the gage head. Notice that the load conditions for the wall shear and moment case are extreme. The beauty of ensuring that the output strains are below the proportional limit is linearity. In other words, once we have a strain output for the 2000

Pa case, as long as we stay within the proportional limit, the strain output for the 1000 Pa case is simply half. Finally, an equivalent inertial magnitude sweep is conducted.

Table 5-5. CF3 constrained state variables.

LOAD	min	SV	max	LOAD
0.85 Min t	1000 Hz	f	NA	
Min τ_w	0.5 $\mu\epsilon$	ϵ	ϵ pl	2 τ_w max
	0	ϵ	ϵ pl	2 Mo max
	0	τ_a	0.25 τ_{wmin}	Max acc
	0	δ	5 mil (gap)	2 τ_w max
	0	δ	5 mil (gap)	2 Mo max
	0	ΔT	1 deg C	$q_w(t) + t$

The first state variable considered is first mode natural frequency, f . Figure 5-4 shows how this state variable varies with the design space. The left figure shows unbound natural frequency in Hertz. The design space shows that the beam length increases from top to bottom, and beam thickness increases from left to right. We can tell as we choose designs that go up and right, or get shorter and thicker, we can achieve higher frequencies. In order to bind this design space, the figure to the right shows the effect of eliminating any gages that have frequencies less than 1000 Hz. The designs that do not meet this minimum requirement are removed as possible designs. Clearly the limit on this state variable has greatly reduced the number of possible designs and has effectively constrained us to a shorter thicker gage than would be demanded just due to geometric constraints.

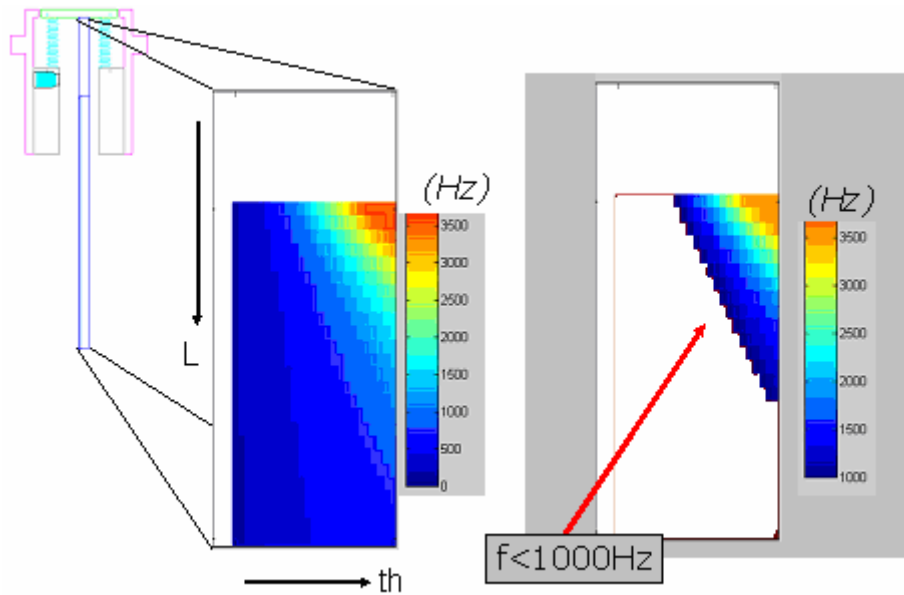


Figure 5-4. CF3 first mode natural frequency.

The next state variable examined is strain. Figure 5-5 shows how each design responds to the minimum expected wall shear, 1000 Pa. The unbound contour values of the left-hand figure propose ridiculous strain outputs where the material would really have failed. These impossible designs are eliminated in the right hand figure by applying the proportional limit criterion for an overshoot 2000 Pa load, i.e. 4000 Pa. This effectively eliminates extremely long and thin beam designs. Of course these were already eliminated by the minimum frequency requirement. However, by maintaining careful bookkeeping of each state variable we can confidently ensure we understand the gage output within these extreme load conditions. Additionally, the right hand figure shows the impact of eliminating low strain designs. In direct opposition to frequency requirements, this minimum strain has pushed the design space away from the shortest thickest available designs. The minimum strain requirement actually pushes the design space down and to the left, i.e. we desire longer thinner beams. This direct contrast to frequency considerations was introduced in the design of CF1 and continues to be a driver for designing direct measure gages.

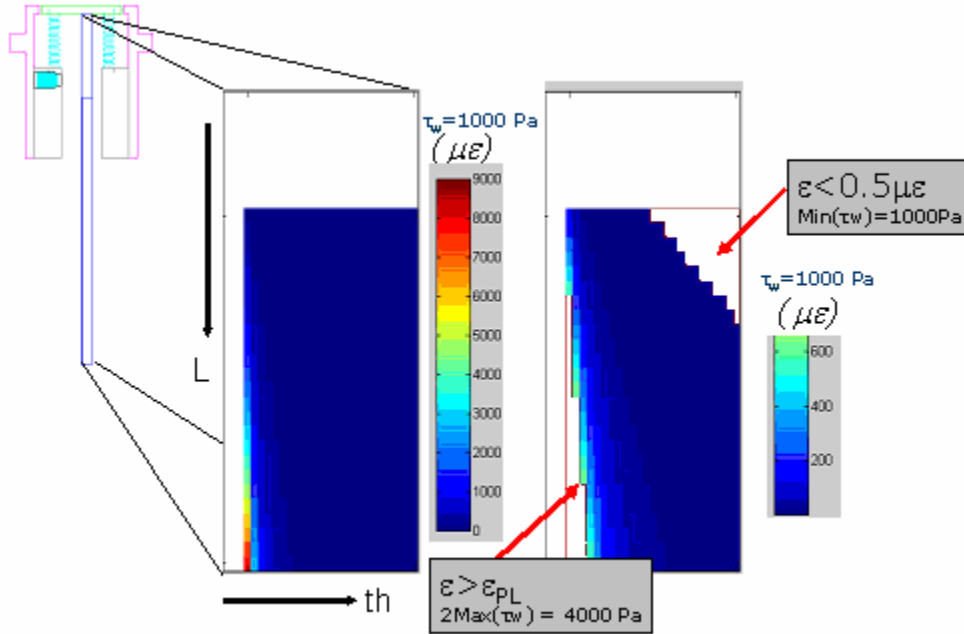


Figure 5-5. CF3 strain output due to 1000 Pa wall shear.

Displacement must be verified to ensure the intended 5 mil gap will suffice. Since the second optimization sweep allows us to predict the maximum δ_x for each design we can check the effects of geometry on this state variable. Figure 5-6 shows the expected displacements for our 2000 Pa case. In order to eliminate designs where overshoot loading would allow the head to hit the housing, we again remove unacceptable designs in the right hand figure. As with the strain proportional limit, the minimum natural frequency limit has already eliminated these potential designs.

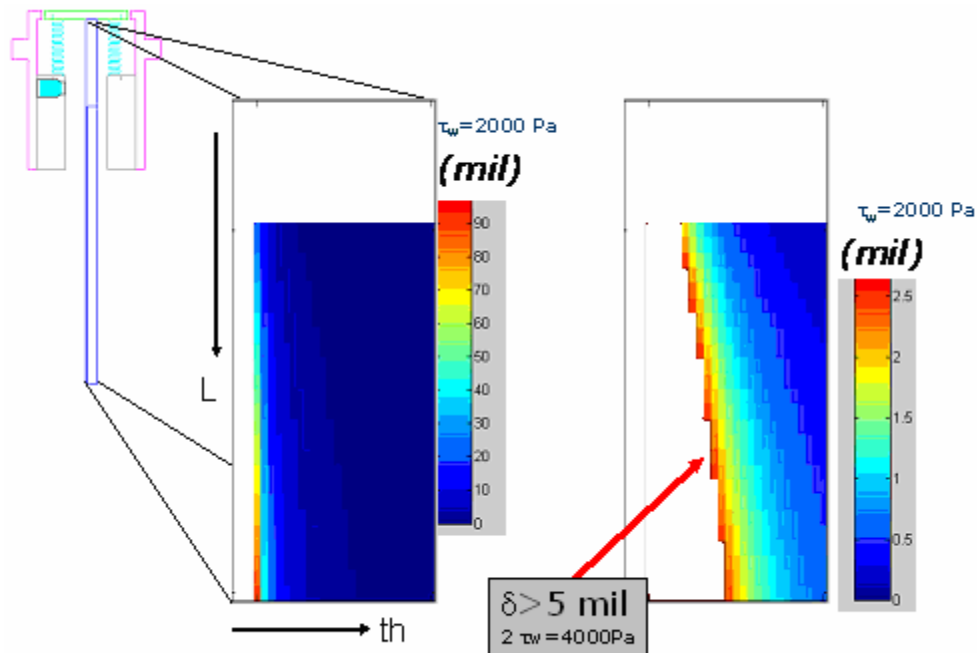


Figure 5-6. CF3 displacement due to 2000 Pa load.

Two of the previous state variables, ϵ and δ , must be checked against the moment loading condition. This moment sweep did not change the already constrained design space. Therefore, we will save the results from this sweep for further discussion after looking at inertial effects.

The final design sweep examines the relative effect of inertia to wall shear. This is done by calculating an equivalent inertial shear due to 1 g acceleration. Figure 4-4 shows this process. The effect of even a small 1 g load is pronounced with these INVAR designs due to the increased mass. Figure 5-7 shows that all of the 625 designs fall between 20-30% of the expected 1000 Pa wall shear. In order to keep our design within some reasonable range, the design was limited to provide at most 25% equivalent wall shear due to 1 g acceleration. Looking at the right hand image in Figure 5-7 we see the impact on the design space due to this limitation. Inertial requirements force the design space up and to the left. This is intuitively obvious since we want a thinner shorter beam in terms of this state variable.

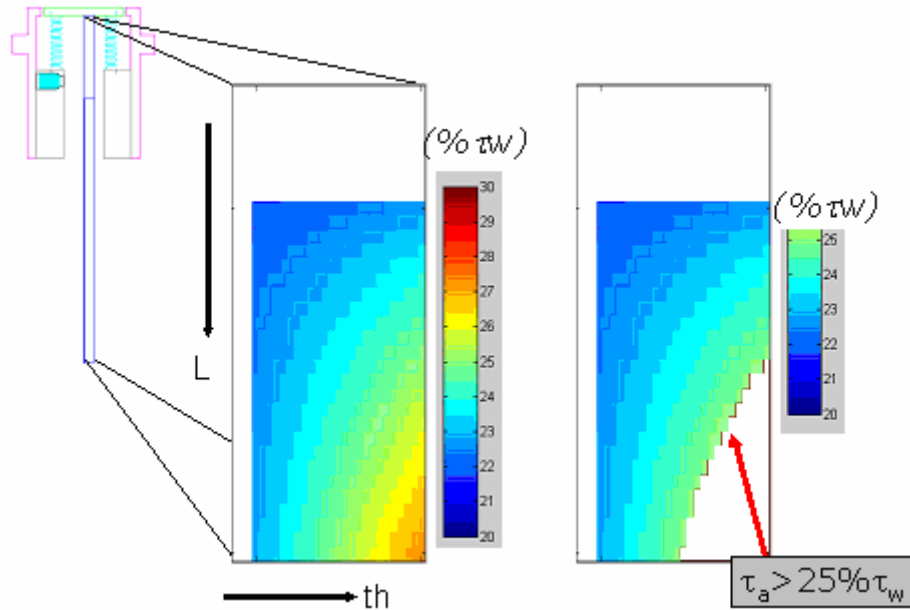


Figure 5-7. CF3 equivalent acceleration shear.

Now we can combine the total effect of all design and state variable constraints. Figure 5-8 shows each of the previously considered state variables and the contribution to limiting design space. Additionally, the effect of moment on strain and displacement is provided. From this we see that minimum natural frequency requirement, minimum strain output, and maximum inertia dominate for the LENS design cases. The culmination of this effort is to narrow the design to one that produces the most strain output with the smallest temperature gradient.

The final design and state variable constrained design space is shown in Figure 5-9. This is significantly smaller than the original space permitted due simply to geometrical constraints. This figure illustrates the impact of the major state variables on design. First, the natural frequency requirements push the design up and to the right. Second, minimum strain requirements counteract this by pushing down and left. The trade-off between these variables was already well understood. The addition of inertial impact and thermal considerations is interesting. The desire to make the beam longer and thicker to allow greater thermal diffusion is directly opposed by the desire to make the beam lighter. In total, these four design variables have contracted the design space to a small band of designs that will meet all of the design requirements imposed by LENS test

conditions. Since we would like to achieve the most strain possible with the smallest thermal gradients, the circled pixel represents the chosen configuration for the CF3 gage.

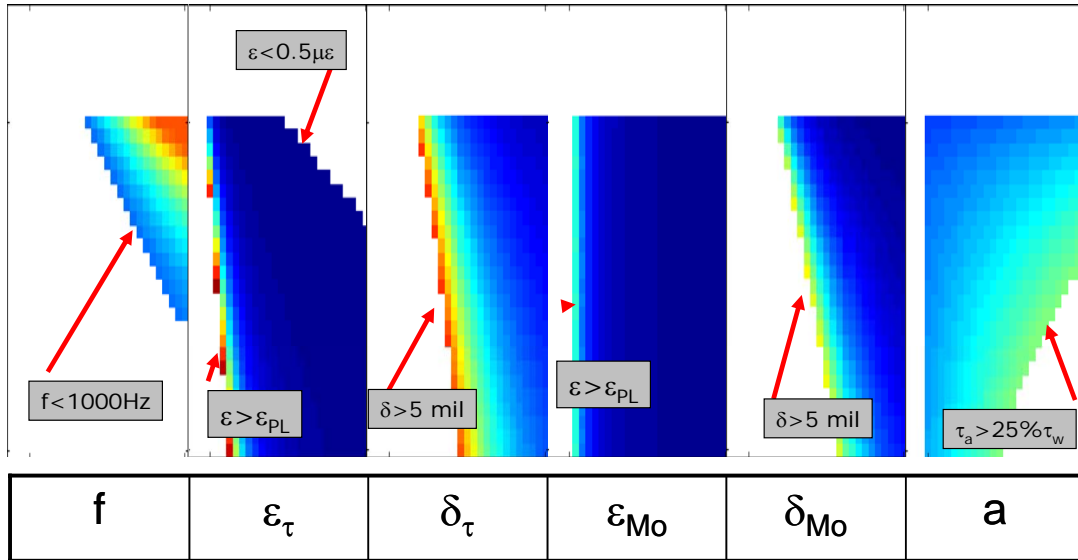


Figure 5-8. CF3 state variable constraints on design space.

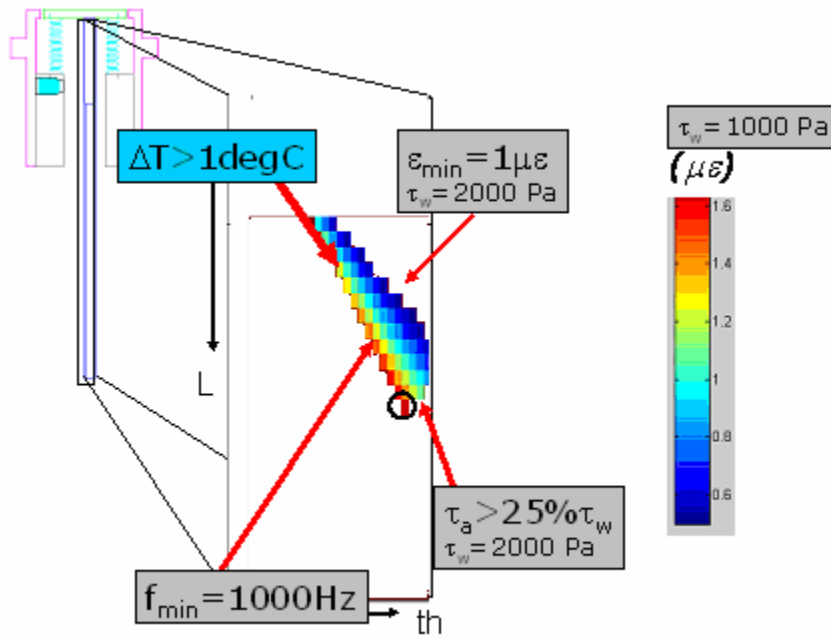


Figure 5-9. CF3 fully constrained design space with expected strain output.

5.1.2 CF4 Gage Design

After completing the design for the INVAR gage, we recognized the desire to reduce weight. The true driver for using INVAR was to avoid thermal problems associated with the long transient heat flux effects in the Virginia Tech supersonic tunnel. Therefore, we decided to make an aluminum gage that would meet all of the LENS requirements. Fortunately, the design optimization tools developed for CF3 could be readily employed to develop an aluminum gage. The same geometric and state variable constraints apply. These were presented in Table 5-4 and Table 5-5 respectively. The same four sweeps were conducted: 1) natural frequency 2) wall shear impact on ϵ and δ 3) moment impact on ϵ and δ and 4) equivalent acceleration shear. Using this process we can look directly at the effect of material choice on design space. Additionally, although all state variables are checked, we can limit the presentation of optimization to the four design space drivers shown in Figure 5-9.

Starting with the same minimum requirement for natural frequency, we can compare the aluminum design space to that of INVAR. This is shown in Figure 5-10. The major trend to push up and to the right remains the same. Additionally, the frequencies are in similar range for both materials. Also, there are more allowable configurations for aluminum.

The next state variable is the strain output. The greater ductility of aluminum significantly impacts the design here. Figure 5-11 shows that even with 10 times the required minimum strain output, the design space is still bigger than that of INVAR. We can expect much larger strain outputs from an optimized aluminum skin friction gage than from CF3. This is an additional advantage to limiting apparent strain due to inertia.

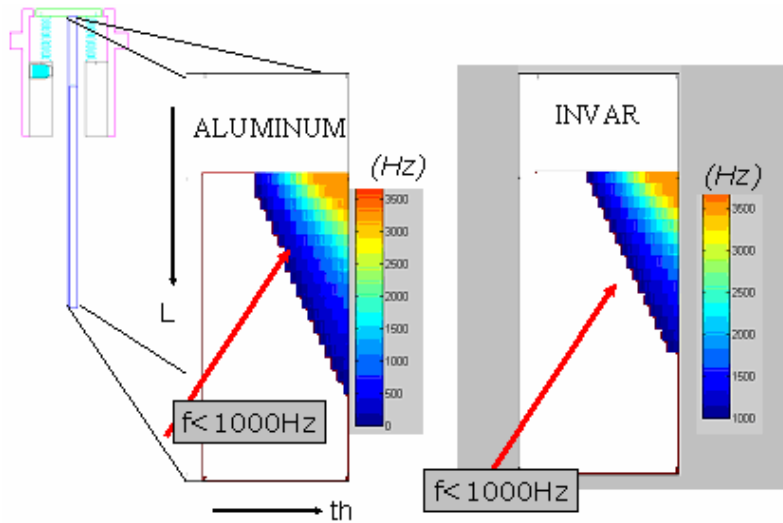


Figure 5-10. CF4 frequency impact on design space, aluminum vs. invar.

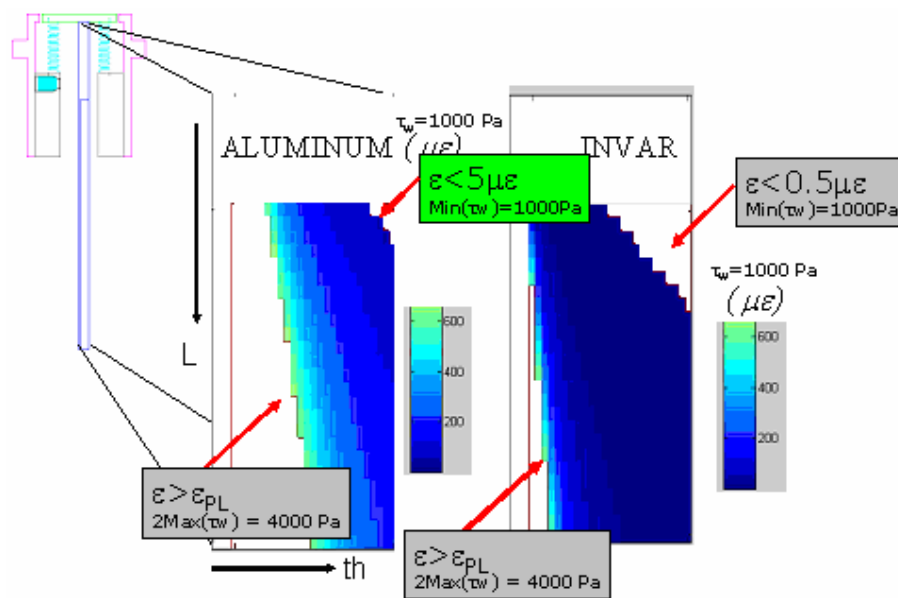


Figure 5-11. CF4 strain response to wall shear.

The last state variable for comparison is equivalent acceleration shear. This is the reason we switched from INVAR back to aluminum. Clearly the change is beneficial. Now the range of expected equivalent acceleration shear has decreased to 15-18% of 1000 Pa for a 1 g acceleration. In fact there is no limitation on design space based on our previous criteria for CF3.

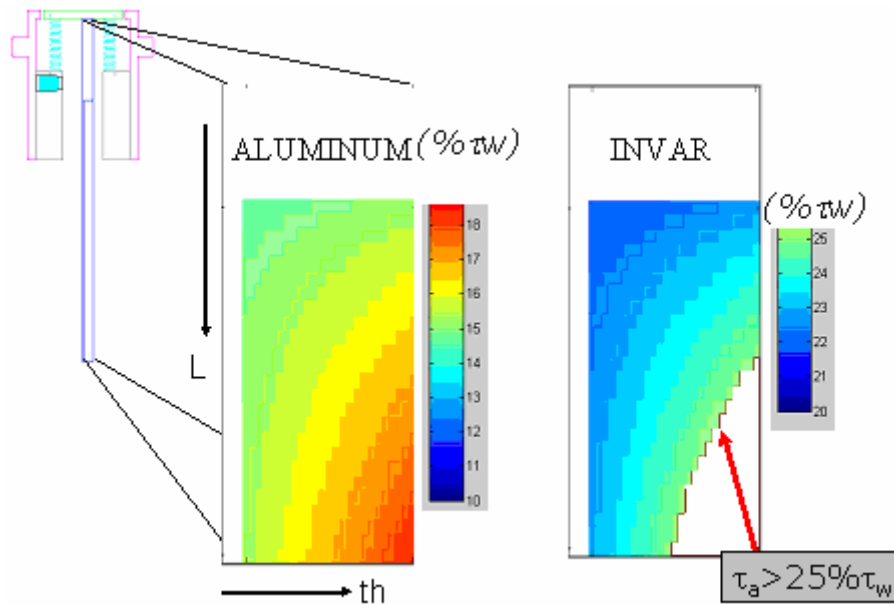


Figure 5-12. CF4 equivalent acceleration shear as percentage of wall shear.

Now we can combine the state variable impact on design space as previously performed for CF3. This is compared to the INVAR design space in Figure 5-13. Notice how many more possible solutions there are using aluminum. However, we must be careful to verify low thermal effects. This was accomplished in Chapter 4: Gage Characterization. At this point, we use engineering intuition to choose our design for CF4. Since the inertial effects are low, we can choose the thickest, longest available design. Aside from the expected thermal benefit, this skin friction gage could be outfitted for full 3-D measurements. In other words, we could place strain gages on all beam faces and measure both axial and spanwise shear with this design.

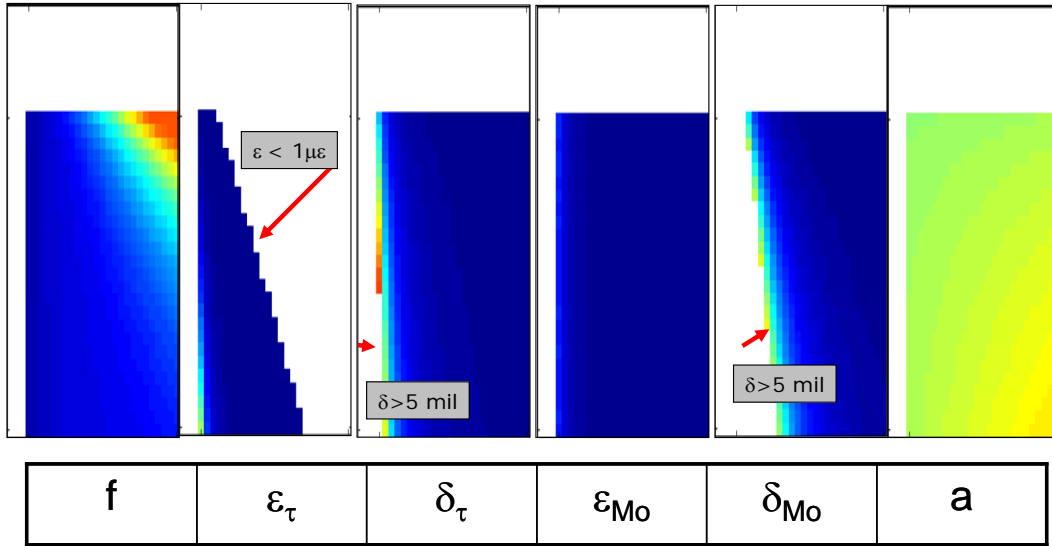


Figure 5-14. Blow down facility constraints on design space.

Now that we have seen how the design space has been affected by each state variable, we can combine the effects and look at the expected strain output for design space under an 85 Pa wall shear. Figure 5-15 shows that the design can be considerably longer and thinner than CF3. In fact, because of the less stringent requirement on vibrational frequency, even longer designs could be considered.

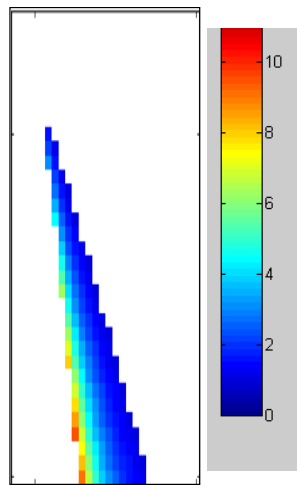


Figure 5-15. Blow down facility expected wall shear strain output.

5.3 Optimization for a Typical Flight Test

The next test condition for consideration is a flight test. As with the blow down facility, the long test time makes INVAR an attractive material choice. Figure 5-16 shows the overall impact of constraints on the state variables. As with the blow down facility, this test condition does not limit the design due to vibrational frequency. In this case however, the higher expected acceleration returns as a limiting factor. Figure 5-17 shows the total effect of all constraints on design space and the expected wall shear induced strain output.

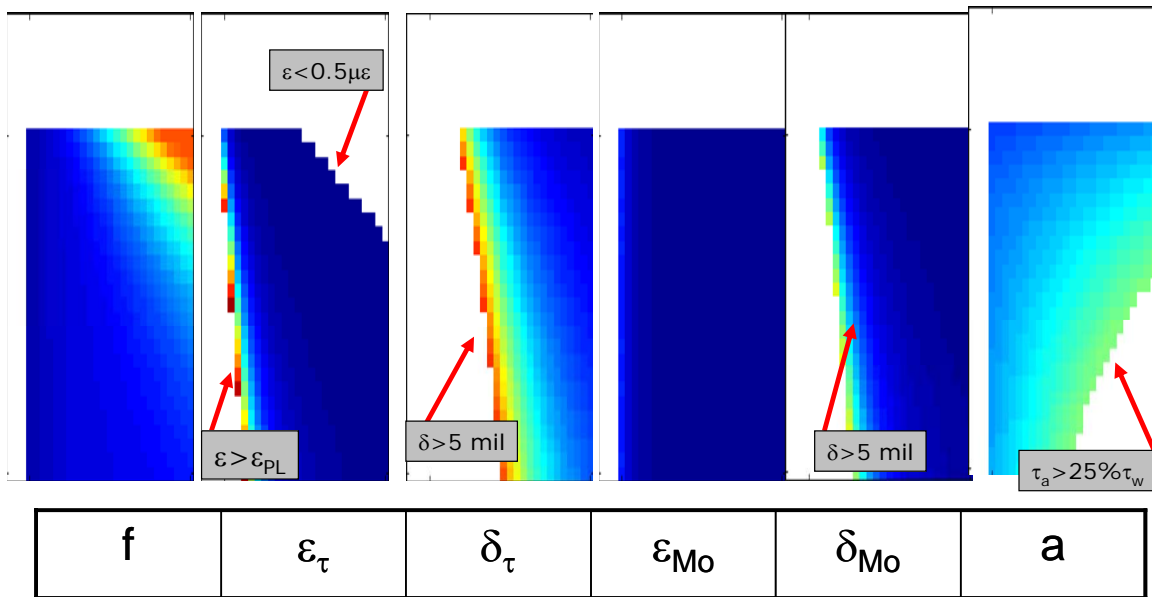


Figure 5-16 Flight test constraints on design space.

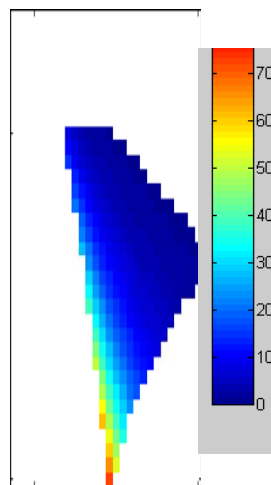


Figure 5-17 Flight condition expected wall shear strain output.

5.4 Optimization Summary

The optimization technique developed through this chapter is a straightforward parametric analysis. First, the material choice was made and the design variables were limited to a constrained length and thickness. Then, 625 different gages within that design space were virtually built and tested. Once we had the gage performance characteristics for every gage, we compared their performance to test facility specifications. Finally, a design that fit within those constraints and provided the desired performance was selected.

Figure 5-18 shows the inputs and corresponding state variables of interest as well as generalized impact on design space. Notice that the modeling techniques chosen in Chapter 4, Gage Characterization, have been applied 625 times for INVAR then another 625 times for aluminum. The only difference in making the design decision was how the gage met the performance constraints of each facility. The heat flux model is only applied after gage selection due to the long computational time required for this investigation.

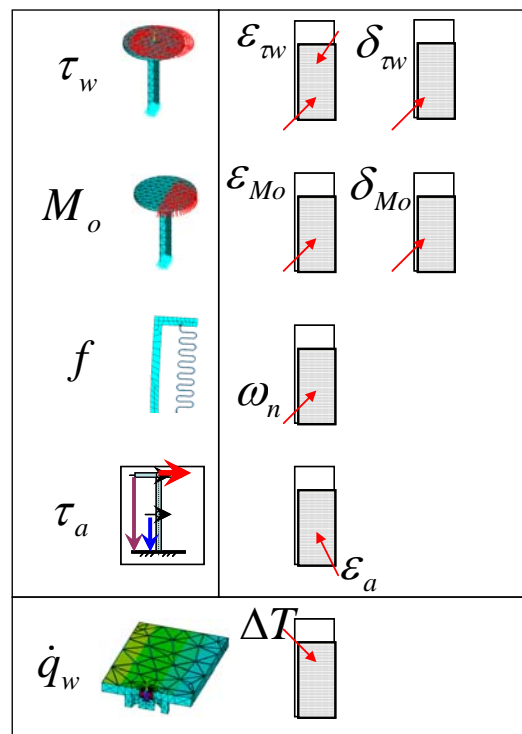


Figure 5-18. Optimization overview.

6 Simulations

The purpose of developing models was twofold: design optimization and virtual testing. A full simulation connects the flow, gage, and instrumentation models. Simulations can be either experimental or computation, and both approaches have been used in this work. The experiments were discussed in Chapter 3. Through simulation we can answer important questions. For example, the simulation developed in the Chapter 2 Theoretical Approach answered how to configure the Wheatstone bridges to separately measure wall shear and moment while being insensitive to other loads.

Several important questions required answering throughout this research. These were attacked through simulation. Each of the following sections poses an important physical question and the simulation solution. Unless noted the instrumentation is assumed ideal so that the gage output is exactly what is measured.

6.1 Instrumentation

The sources of apparent strain for this type of gage were discussed in Chapter 4: Gage Characterization. Additionally we must investigate other possible causes of error. Instrumentation provides the other most likely reason for measurement error. These sources come from strain gage manufacture and alignment, lead wire resistance, and amplifier resistances. Table 6-1 lists these error sources and maximum impact which will be applied to determine overall system error. All of these errors are quoted by the manufacturer except strain gage misalignment. These are conservatively high estimates based on FEM strain distribution.

Table 6-1. Instrumentation error sources.³⁷

	Maximum error
Strain gage R_G	+/- 0.2 % = 0.7 Ω
Strain gage vertical misalignment 1 mm offset	5% of total $\mu\epsilon$
Strain gage angular misalignment 5 deg	1% $\mu\epsilon$
Lead wire resistance 3 ft 0.35 Ω /m	0.32 Ω
Meter resistance 5 % of 100 k Ω	5 k Ω
Power supply resistance	0.1 Ω

As a worst case scenario, all of the strain gage errors were applied to one side of the half bridge to determine the maximum error impact on total voltage output. Accounting for this error and lead wire resistance we can find the expected real output voltage using Equation 6-1. Using the nominal output conditions for CF3 from Chapter 4, yields a 5.3 % variation of output voltage at the root.

$$\Delta V = V_{in} Gain \frac{R_1(R_2 + R_L) \frac{\Delta R_1}{R_1} - R_2(R_1 + R_L) \frac{\Delta R_2}{R_2}}{(R_1 + R_2 + 2R_L)^2 + (R_1 + R_2 + 2R_L)(\Delta R_1 + \Delta R_2)} \quad \text{Equation 6-1}^{38}$$

Now accounting for the additional error of impedance from power supply and meter, we can determine the total error output for the system. This is accomplished by multiplying Equation 6-1 by the following factor where R_s is supply resistance, R_m is meter resistance, and R_B is bridge resistance, calculated to be 350.175 Ω . The resulting total error on output voltage due to these maximum error conditions is 5.6 % at the root for CF3.

$$factor = \left[\frac{1}{1 + \frac{R_s}{R_B}} \right] \left[\frac{1}{1 + \frac{R_B}{R_m}} \right] \quad \text{Equation 6-2}$$

If there is no strain gage vertical or angular misalignment, the expected error is 1.7% from lead wire resistance alone and a total instrumentation error of 2.0%. This analysis has shown that the maximum expected instrumentation errors are relatively low. Most of the error comes from the high estimate of alignment error. Other instrumentation error is due to lead wire resistance, which is limited by keeping the wires short. In the sections that follow, instrumentation error is assumed zero unless noted.

6.2 Dynamic Response

The entire measurement process for these types of gages is dynamic. Even an ideal step load produces transient response. This aspect of the instrumentation brought up several issues that were resolved through simulation.

6.2.1 Minimum Natural Frequency

One of the first hurdles for this type of gage is to achieve fast enough settling time to provide accurate measurements even in the short run times encountered in LENS. The first question: What is the minimum natural vibration frequency necessary for a settling within a 10 ms test run? The conservative answer of 1000 Hz was presented in Figure 5-3. But this is only a part of our total simulation solution.

6.2.2 Filter Setting

This brought up another important question. What Butterworth filter should be used to provide the best signal output? If we assume a simple step load of 1000 Pa, and an exactly calibrated gage with ideal instrumentation, we can simulate the signal response for several different cut-off frequencies as in Figure 6-1. Here we see that the 100 Hz filter is the bare minimum to try and measure this gage reaction. A 1000 Hz or 10 kHz filter is preferable. As a note, wideband or raw signal response could be used. However it would produce aliasing if we wished to perform signal analysis in the frequency domain.

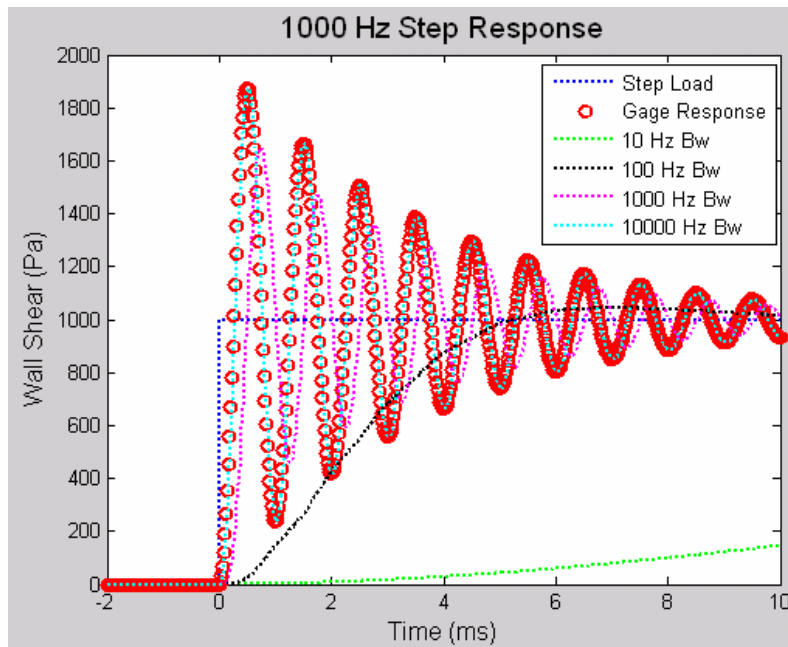


Figure 6-1. Expected signal output using several cut-off frequencies.

6.2.3 Gage Reaction to Heaviside load

We've seen how the gage should respond to a simple step load. But what about a load that is more representative of test conditions? Additionally, we have to consider the impact of imperfect instrumentation. So we have to answer two questions: 1) how does the gage response look given a realistic load? and 2) what kind of error can we expect with real instrumentation error?

A full simulation was developed. Figure 6-2 shows a simplified Heaviside forcing function approximation to the time varying wall shear measured in the blow-down facility at Virginia Tech. The beam model for displacement and strain is a cantilever. The voltage output comes from a realistic instrumentation system that accounts for strain gage vertical and angular misalignment, lead wire resistance, and power supply impedance.

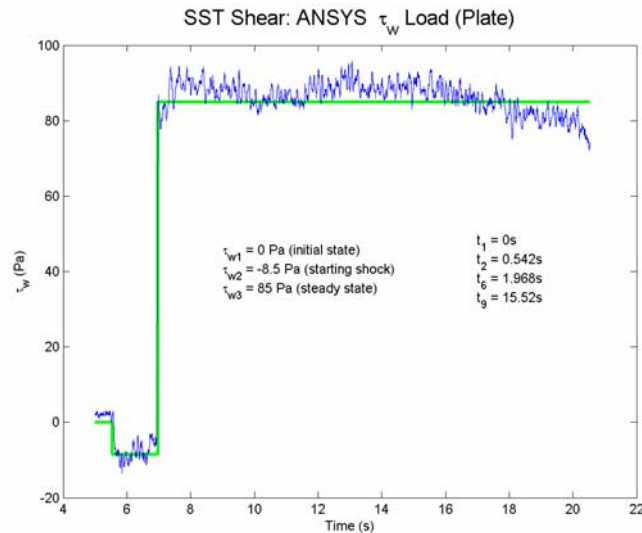


Figure 6-2. Heaviside approximation to Virginia Tech time varying wall shear.

A screen shot near the end of the steady load of this simulation is presented as Figure 6-3. In the top left image, we see the wall shear deck. In the top right is the gage displacement with strain gages slightly offset near the head. The bottom left shows the strain measurements at each strain gage location. Finally, the bottom right shows the resulting expected voltage output for this load condition.

In answer to our first question, the gage response to this single load input was as we expected. Notice that no filter was applied. This is evidenced by the rapid overshoot captured in the bottom left figure. So for long run times as in the VT supersonic tunnel, we can overcome the transient response by application of a low-pass filter.

In answer to the second question, the packaged instrumentation showed considerable robustness. The simulation showed that despite the introduction of multiple, but reasonable, error sources within the instrumentation, the overall system error excepting strain gage alignment was around 1%. The simulation also showed that even with slightly exaggerated misalignments of the strain gages, the measurements were within 5% of actual. This was good news since, such a large error in manufacturing would have had the gages offset by 1/2 gage length. Fortunately, none of our gages are offset to the extent that could be detected by the naked eye, which is much less than 1/10th of a gage length.

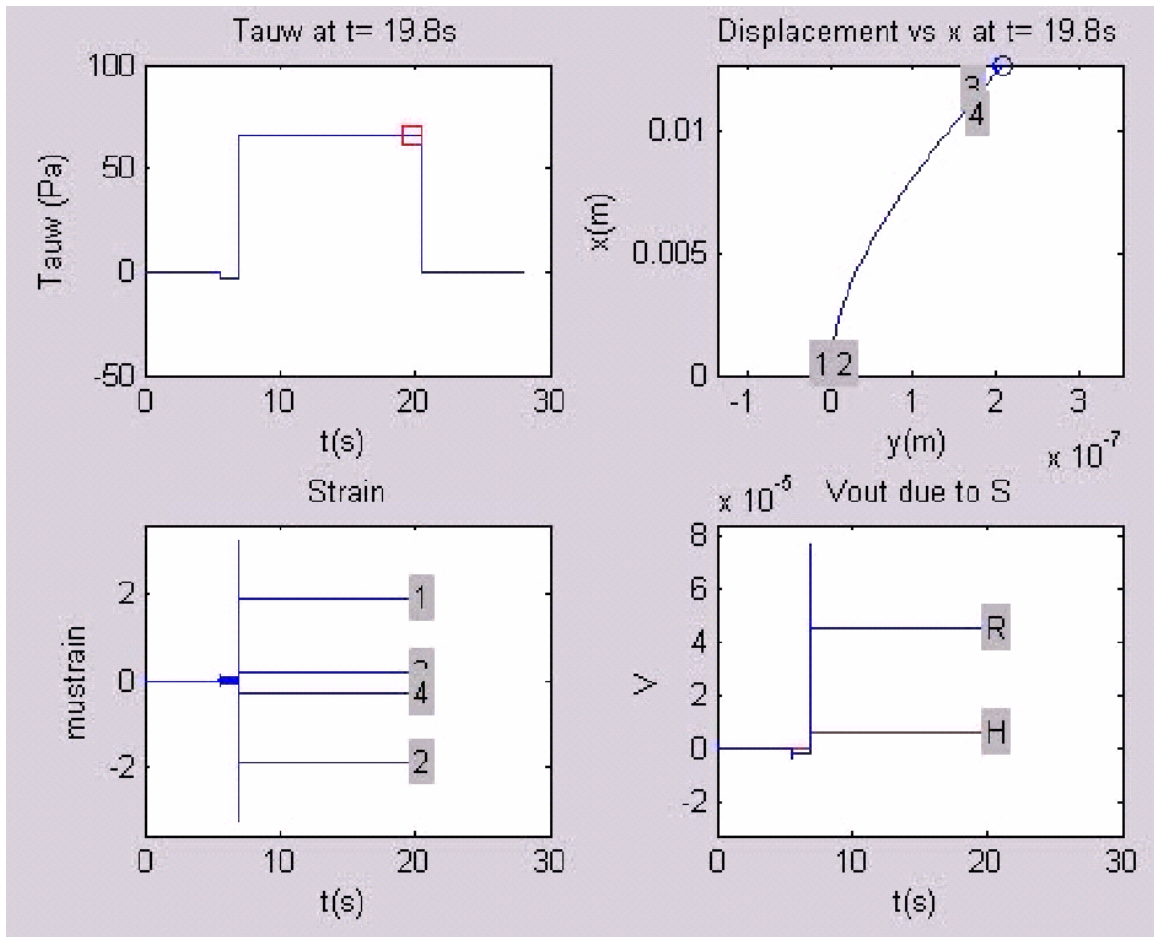


Figure 6-3. Simulation of Virginia Tech pure wall shear case.

6.2.4 Base Acceleration Response³⁹

The loads and initial conditions evaluated to this point were due to single input systems. Accelerometer measurements in the LENS facility showed that a multiple input simulation was necessary. In this case, we developed transfer functions to capture base acceleration and wall shear induced motion. The “base” in this case is the physical test specimen, for example a model of the NASA Aerospace plane. The plane would experience acceleration during the tunnel run similar to that shown in Figure 6-4. Using the trapezoidal rule, the velocity, and displacement of the base are also shown. Here we see that in just 25 ms, the base model has displaced over half a millimeter. This would in turn affect the skin friction gage. Figure 6-5 shows a simple uni-axial block model of the skin friction gage in this condition.

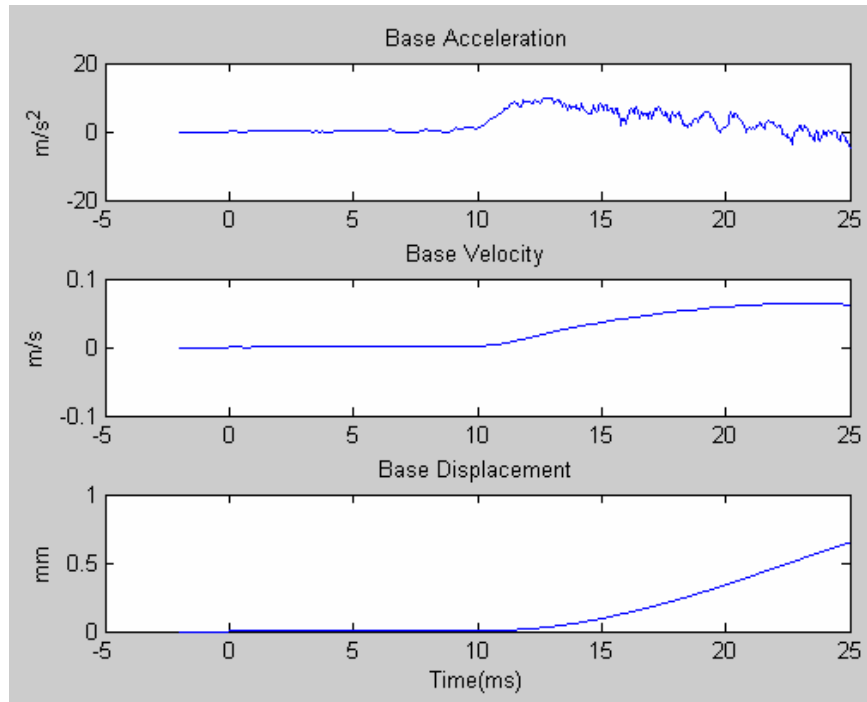


Figure 6-4. Acceleration, velocity, and displacement of base in LENS.

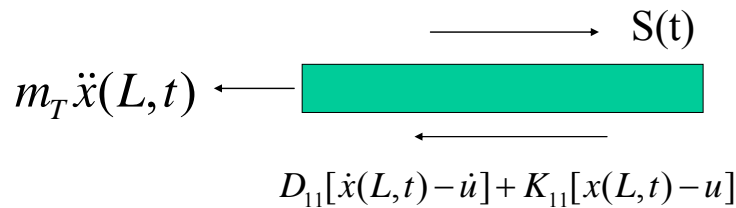


Figure 6-5. 1-D kinetics diagram.

This model can be broken down into two linearly independent systems where the total motion, x_L , is composed of the superposition of motion due to base acceleration, x_U , and the motion due to shear load, x_S . This is Equation 6-3. The first component of displacement considered is due to a step wall shear, $S(t)$. Equation 6-4 shows the corresponding ordinary differential equation (ODE). The coefficients D_{11} , K_{11} , and m_T are gage properties and L is length along the beam. The next component of displacement is due to the base motion shown in Figure 6-4. The ODE for this component is Equation 6-5.

$$x_L = x_S + x_u \quad \text{Equation 6-3}$$

$$m_T \ddot{x}_S + D_{11} \dot{x}_S + K_{11} x_S = S(t) \quad \text{Equation 6-4}$$

$$m_T \ddot{x}_u + D_{11} \dot{x}_u + K_{11} x_u = D_{11} \dot{u} + K_{11} u \quad \text{Equation 6-5}$$

We are interested in the relative motion of the gage from the base reference frame. Therefore, we have to recast Equation 6-5. Consider that the relative motion of the gage due to the base motion is $z = x_u - u$, where x_u is the total gage displacement due to base motion and u is the base displacement. Substituting this relative motion equation into Equation 6-5 and solving yields Equation 6-6.

$$m_T \ddot{z} + D_{11} \dot{z} + K_{11} z = -m_T \ddot{u} \quad \text{Equation 6-6}$$

The corresponding transfer functions for Equations 6-4 and 6-6 are Equations 6-7 and 6-8 respectively. Using the Matlab® control system toolbox for linear time invariant systems, we can simulate the system response to the wall shear and acceleration inputs. Figure 6-6 shows the result of this simulation. In the top left figure, the response to a pure wall shear of 2000 Pa acting on the CF3 gage is modeled. The predicted displacement of about 4.5 μm is of the right order of magnitude of the FEM predicted 3.1 μm . The top right figure shows base motion induced displacement. In this case, the dynamic model predicts a maximum absolute displacement of about 0.3 μm , corresponding to 1g acceleration. This matches the combined solid mechanics/ FEM prediction of 0.3 μm .

$$\frac{X_s}{S/m_T} = \frac{1}{s^2 + 2\zeta\omega_n s + \omega_n^2} \quad \text{Equation 6-7}$$

$$\frac{Z}{U} = \frac{-s^2}{s^2 + 2\zeta\omega_n s + \omega_n^2} \quad \text{Equation 6-8}$$

It is important to note that this 1-D dynamic response model is not intended to accurately predict displacement. The 1-D simplification causes this simulation to slightly overpredict the displacement due to wall shear. This simulation was intended to show a relative dynamic system response to two separate inputs. This is shown in the bottom image of Figure 6-6. This simulation of the total signal output provides several insights. First, the total response is not static. The real measurement signal is going to have expected oscillations. Second, if we look just at the average signal values over the test window, the pure shear output is not too different from the total signal output. In fact, the variation is just 1.2 % and that's with this simplified model.

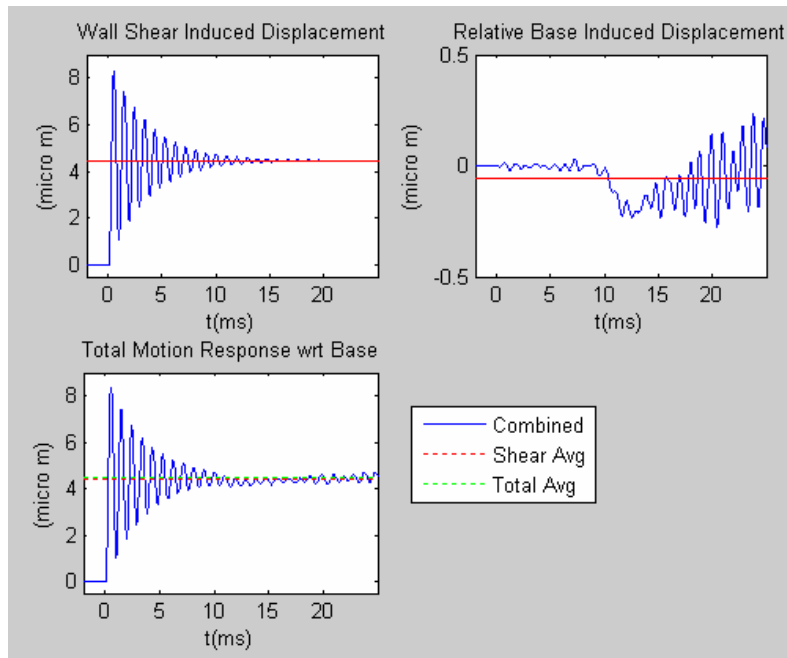


Figure 6-6. Simulated 1-D gage response to multiple inputs.

Thanks to this investigation, acceleration considerations could be justifiably simplified. Rather than trying to track the overall effect on the signal, we scaled back to looking at expected order of magnitude effects. Thus we developed the equivalent

acceleration shear. This quick approach allows a convenient method to design gages constrained by designer imposed inertial limits. Additionally, the simple solid mechanics model can more accurately predict the relative strain output.

6.3 Thermal response

The thermal issue uncovered during the Virginia Tech Shear test spawned several questions. Was there a direct relation between temperature and voltage output? This was eliminated as a possibility through calibration testing. This meant there was either something wrong with the instrumentation, thermal gradients were causing a problem, or the temperature distribution varied through the thickness of the beam. Each of these possibilities was examined carefully through simulation. The simulations started from a simple 1-D finite difference model (FDM), to 2-D FDM, to Axisymmetric FEM, and finally a full 3-D FEM. Additionally, the boundary conditions increased in complexity from a varying wall temperature to a time and spatially varying heat flux.

Starting with the 1-D case, we can examine expected thermal changes due to step loads. The method of verification is the semi-infinite body Gaussian error function distribution. Two types of analytical solutions are available. One is for a step temperature condition. The second is for a step heat flux. Both only consider 1-D axial changes, so for the purpose of this model “x” is used to describe this direction and denotes distance from the surface. This direction is negative y in our Cartesian flow frame.

6.3.1 Step Temperature Boundary Condition

The step boundary condition provides the basis for determining heat flux from static wall temperature. We verified our 1st order time 2nd order space forward time central space (FTCS) solution to the heat flux equation. An aluminum semi-half body, $\alpha=8.6E-5$ m²/s, initially at 290K has a step surface temperature change to 400 K. This step boundary condition, $T_{w0}=290$ K and $T_{w2}=400$ K, is applied for 9.0 s. Table 6-2 shows the governing equations for the model and analytic solutions. For the FTCS, n is time index, i, is the spatial index. The FTCS model met the stability criteria of $d \leq 0.5$. The model results were well matched. The final result at 9.0s is shown in Figure 6-7.

Table 6-2. Thermal step equations.

	Analytic Solution ⁴⁰	FTCS ⁴¹
Thermal Step Equations	$T(x, t) = erf\left(\frac{x}{2\sqrt{\alpha t}}\right)(T_{wo} - T_{w2}) + T_{w2}$	$T_i^{n+1} = T_i^n + d(T_{i+1}^n - 2T_i^n + T_{i-1}^n)$ $d = \alpha \frac{\Delta t}{\Delta x^2}$
Heat Flux Estimate	$\dot{q}_w = \frac{k}{\sqrt{\pi\alpha t}}$	$q^n = k \frac{T_w^n - T_w^{n+1}}{\sqrt{\pi\alpha t}} e^{-\frac{\Delta x}{4\alpha t}}$

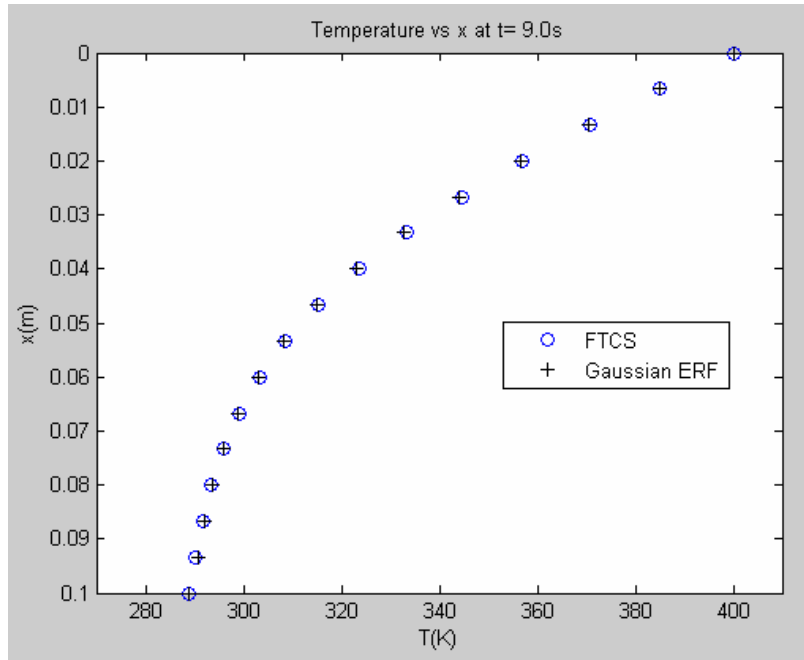


Figure 6-7. Gaussian analytic and 1-D FTCS thermal step solution at 9.0 s.

6.3.2 Step Heat Flux Boundary Condition

The step heat flux boundary condition is useful especially for a first estimate of thermal effects. For example, we have an estimate of the constant heat flux value in the LENS facility. This verification uses an aluminum semi-body initially at 287 K with a sudden heat flux of 100 kW/m². This condition is applied for 0.9s. The equation for this condition is presented in Table 6-3.

Table 6-3. Analytic solution for sudden heat flux.

	Analytic ⁴²
Heat flux step equation	$T = \frac{\dot{q}}{k} \left[2\sqrt{\frac{\alpha t}{\pi}} \exp(-z^2) - x(1 - \text{erf}(z)) \right] + T_o$ $z = \frac{x}{2\sqrt{\alpha t}}$

A comparison is made between the FTCS model and the analytic model. The temperature distributions for both solutions after 0.9 s are shown in Figure 6-8. As with the thermal step solution, the numerical approximation lies directly on top of the analytic solution.

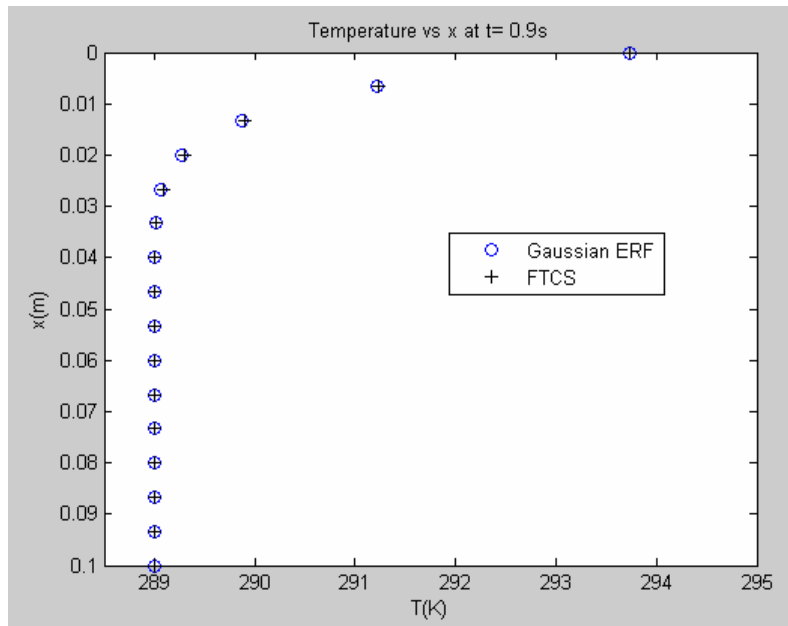


Figure 6-8. Gaussian analytic and 1-D FTCS heat flux step solution at 9.0 s.

Heat flux determines the temperature distribution. Since we only have a thermocouple measurement at a point on the surface, we need to use a method to approximate heat flux. Several techniques are available.⁴³ Unfortunately, none of these techniques were satisfactory. A new method was developed that emphasized the test run physics. We know the tunnel sees a 1) starting shock followed by 2) a transient state and finally 3) the steady state. So rather than trying to develop an exact time varying heat flux, we only seek three load step conditions that correspond to these three states.

The result of this technique is compared to the classic Cook-Felderman integration method in Figure 6-9. Clearly the new technique provides a “clean” approximation to the heat flux that is relatively simple to input as a surface flux in an ANSYS model.

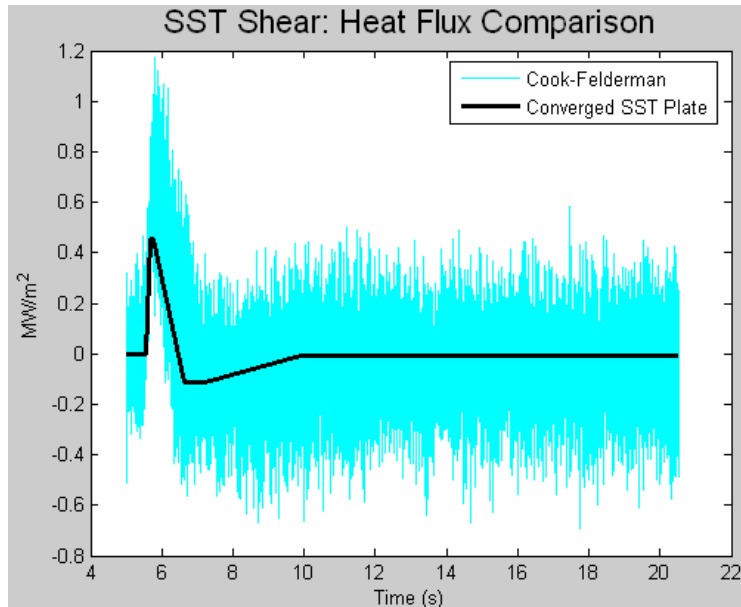


Figure 6-9. Heat flux development for Virginia Tech supersonic tunnel using thermocouple data.

The validation of this simplified heat flux step load uses an Axisymmetric FEM where a node at the thermocouple location tracks temperature. The result is shown in Figure 6-10. Even though the temperature output is slightly different than measured, the difference is negligible and worth the simplification of the load step approximation.

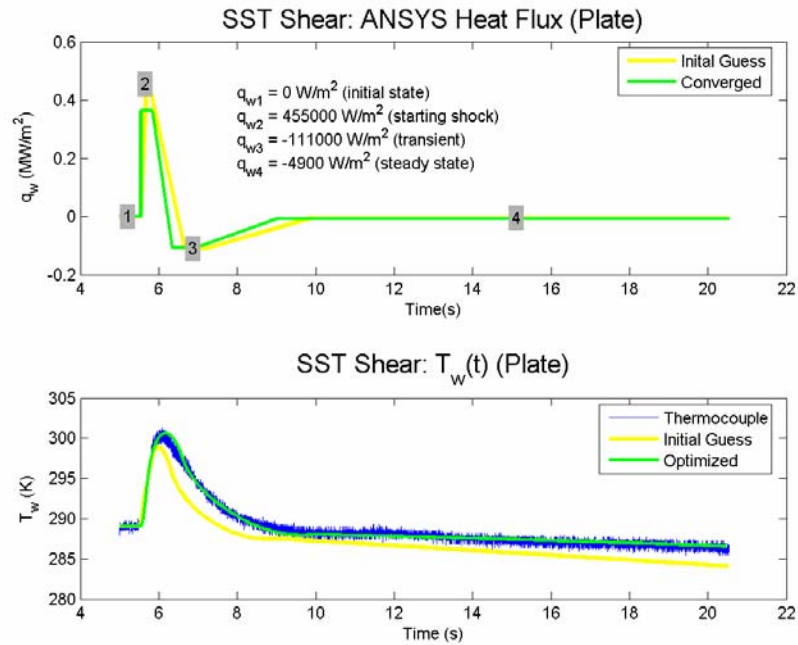


Figure 6-10. Validation of Axisymmetric FEM and approximated heat flux.

The combined approximate heat flux and wall shear are shown in Figure 6-11. It is important to notice that even these approximations require 10 separate load steps. However these load conditions provide a reasonable approximation to allow for determining gage response.

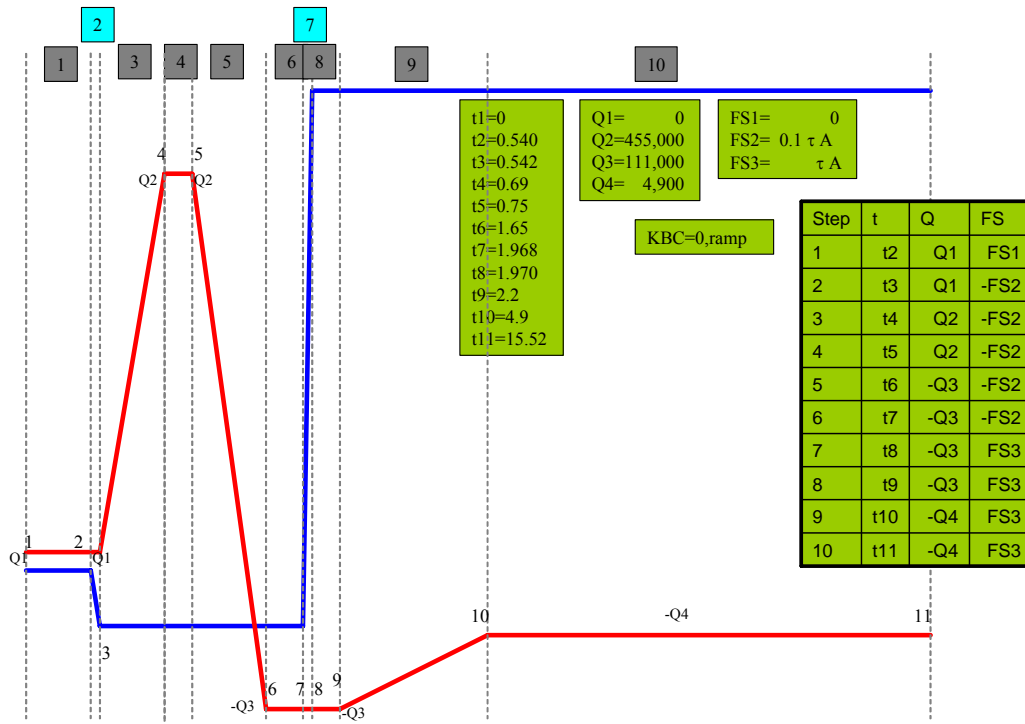


Figure 6-11. Load deck for Virginia Tech supersonic tunnel.

6.3.3 Thermal Distribution 2-D FDM

A 1-D model cannot capture the effects of thermal diffusion due to oil. What does the thermal distribution look like using a 2-D FDM? In this case we used the alternating direction implicit method. Again the measured static temperature was set as the surface boundary condition. Figure 6-12 shows the 2-D FDM results late in the supersonic shear run. On the left we see the measured thermocouple data. The figure on the right shows a slice of the gage. The bellows is prominently shown. The air cavity is on the left and the oil cavity is on the right.

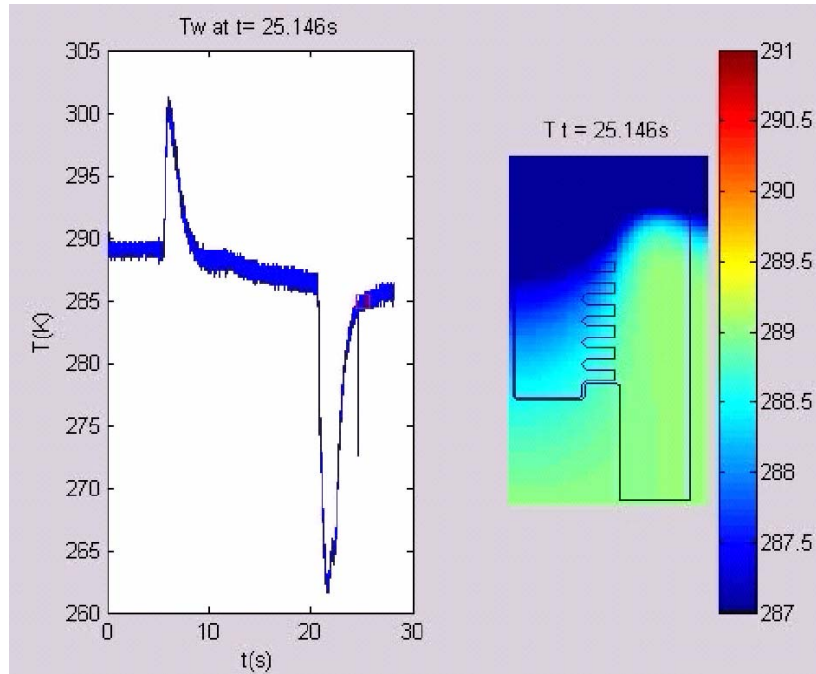


Figure 6-12. 2-D FDM temperature distribution.

Despite this being only a 2-D model using a simple boundary condition, it provides important visual benefit. Notice how the temperature distribution has diffused quickly through the air and is slowed by the oil. This shows that the oil provides some thermal protection at least from the air. Additionally, this figure shows how the temperature gradients near the head strain gage are much greater than at the root. This simulation has helped to provide some physical insight but raises other important questions.

6.3.4 2D FDM Result with Instrumentation Error

In for temperature to produce an output voltage, there has to be a difference between the temperature measured by the strain gage at the front and rear of the beam. The only way for this to occur in the 2D simulation would be from strain gage misalignment. Could an offset of the head strain gages measure enough strain difference to cause the voltage output shown during testing? The previous 2-D FDM solution to the heat equation was used to model the gage response. The surface boundary condition was held to measured thermocouple temperature for convenience. The strain gages were purposely offset in the model. The results are shown in Figure 6-13.

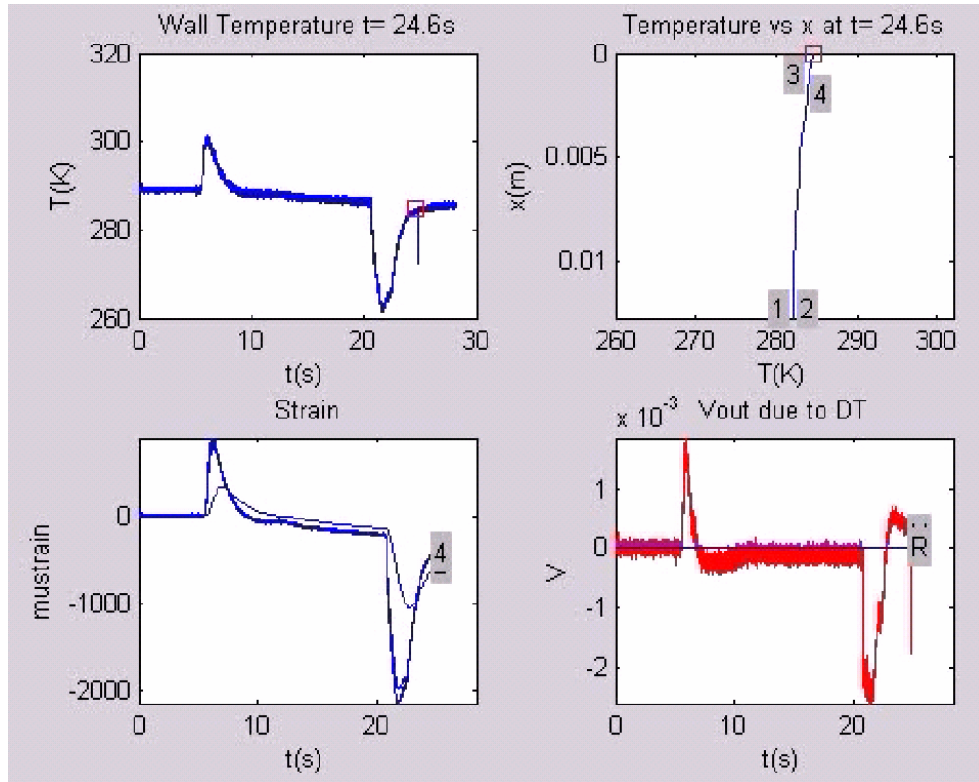


Figure 6-13. Thermal investigation of strain gage offset.

In this screen shot of the simulation video, the top left image shows the measured output for static temperature. The top right image shows the temperature distribution with offset strain gages at the head. The bottom left image shows the strain output due to this purely thermal load. The bottom right image shows the resulting voltage output.

This simulation showed that even with matching front and rear temperature distributions on the beam, an output voltage could occur with strain gage misalignment. The misalignment of this simulation was purposely exaggerated. This means the high voltage measurement from testing probably came from an additional source. This provided the impetus for an axially varying heat flux investigation.

6.3.5 Thermal Distribution Axisymmetric FEM $\dot{q}_w(t)$

The FDM showed some potentially interesting thermal gradient issues. In order to understand them better we need to increase the model fidelity. What happens when we incorporate fully 3-D effects and use a realistic heat flux boundary condition? In order to

answer that question, we started with an axisymmetric FEM model. Using heat flux that is only dependent on time as a boundary condition, we can look at a slice through the center of the gage.

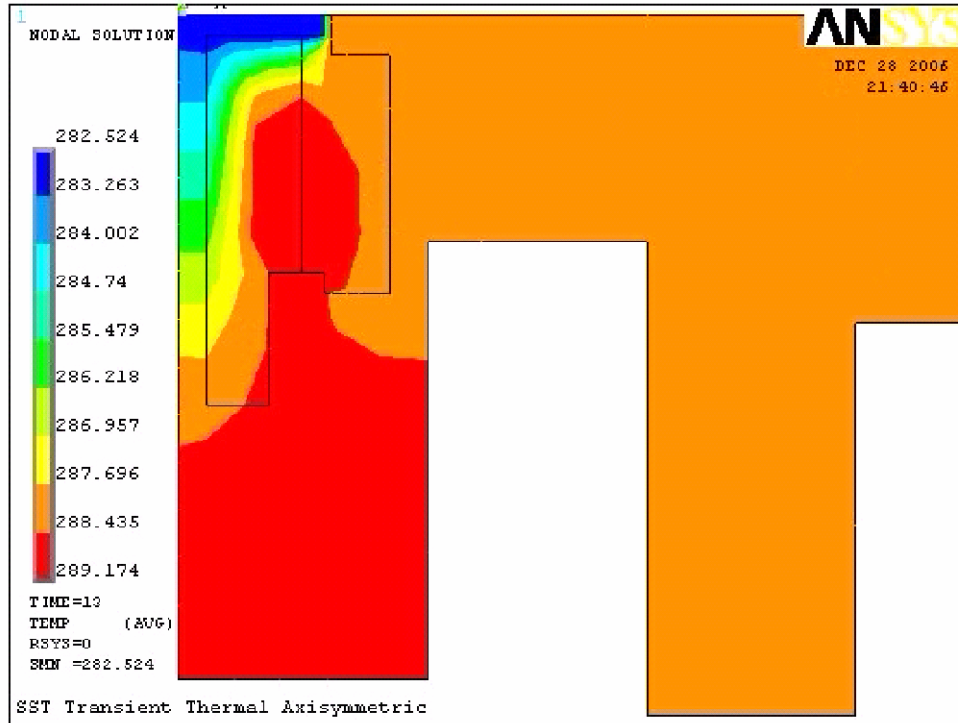


Figure 6-14. Axisymmetric FEM temperature distribution.

Figure 6-14 is a screen shot of the time varying temperature load. It shows that even with the oil available for diffusion, the temperature gradients along the beam are considerable. The temperature range is relatively small. The problem is that when the strain due to shear at the head is less than $1 \mu\epsilon$, any apparent strain due to thermal effect dominates.

6.3.6 Thermal Distribution 3-D $\dot{q}_w(x, t)$

The final thermal investigation considers our time and space varying heat flux. What kind of variation of temperature distribution is caused by spatially varying heat flux? To answer this question requires a full 3-D FEM. The heat flux loading is shown in Figure 6-15. Each of the main steady loads is highlighted clearly showing the heat flux variation with axial location.

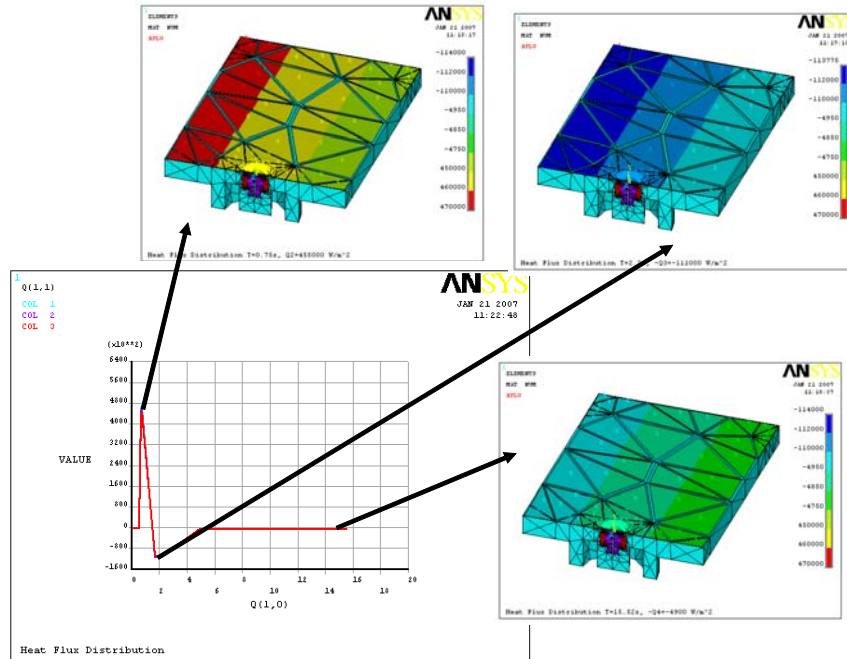


Figure 6-15. Time and space varying heat flux for Virginia Tech supersonic tunnel pure wall shear.

Next we can look at a full 3-D image of the real model and examine just the regions of interest. Although the 3-D FEM solves for temperature at every node, we are really only interested in the temperatures that effect our strain gages. In order to better see the thermal distribution at these important locations, we look at planar slices at the front and rear of the beam. This concept is displayed in Figure 6-16.

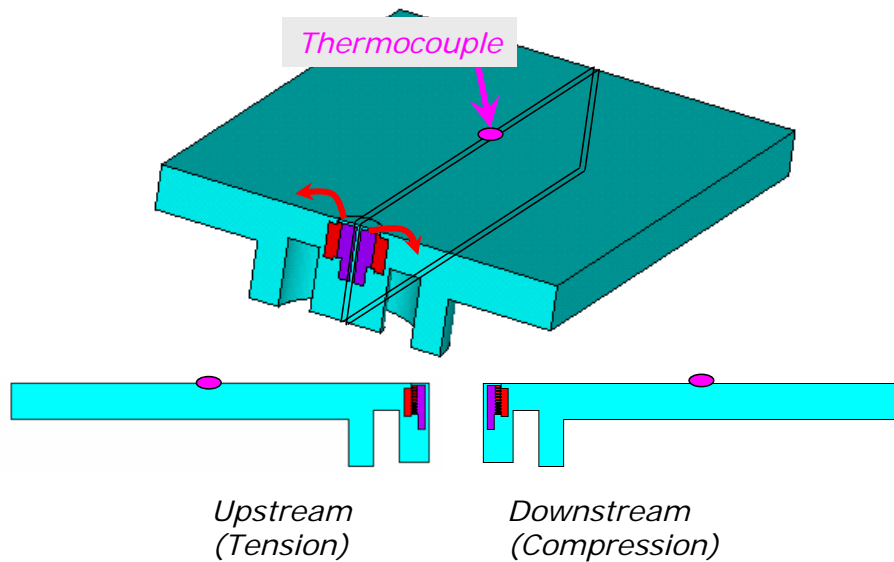


Figure 6-16. Planar slices of 3-D FEM.

Figure 6-17 shows a screen shot of this simulation. The top two images show the temperature distribution at the front and rear of the gage. Although these distributions are similar, there are differences. These temperature gradients through the thickness of the beam are examined in the bottom left panel. At this measurement point in time, the variation is relatively small, less than 0.1 K at any point. However, a time history of the maximum gradient through the thickness is shown on the bottom right. This image show that as the shock passed over the gage surface and for a small period of time afterward, the thermal gradient reached about 0.3 K at a maximum.

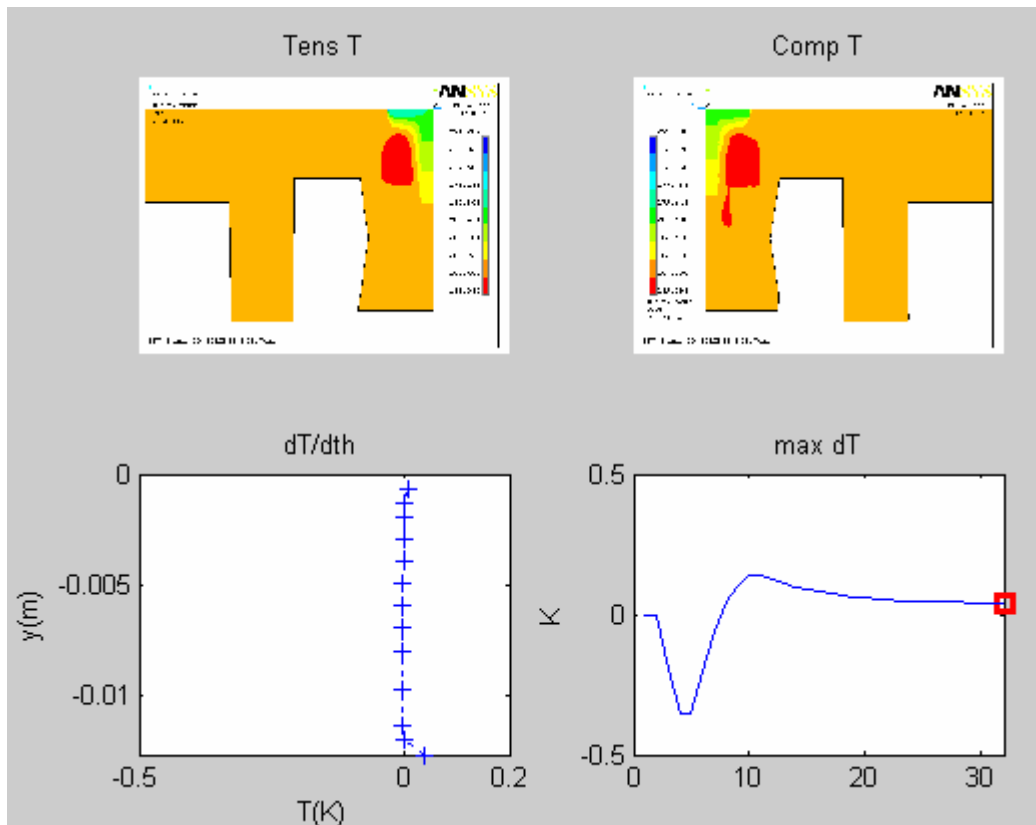


Figure 6-17. 3-D FEM time and space varying heat flux.

This simulation proves that spatially varying heat flux could have contributed to the thermal sensitivity noticed in the VT supersonic wall shear test. This combined with the possible instrumentation error would

7 Conclusions and Recommendations

This research provided several contributions in the area of the design of direct measure skin friction gages for turbulent compressible flows where shocks might be present. These contributions can be listed as:

1. Designed, built, and tested a gage that measures wall shear and moment (CF2)
2. Determined most suitable gage characterization techniques
3. Developed design optimization procedure for bellows-oil configuration gages
4. Designed gages for short-duration, high-enthalpy testing (CF3 and CF4) and examined effect on design space for blow-down facility and flight tests
5. Wrote multiple simulations for static, thermal, and dynamic analysis

The first objective was to build a gage to separately measure wall shear and moment. CF2 accomplished this. In a pure-shear environment, where voltage output from the head bridge was either small or showed signs of thermal strain, the root voltage output provided high-fidelity results for wall shear. In the case where a shock was present, CF2 captured the event. Additionally, the oil-filled configuration completely eliminated uniform wall pressure as a source of apparent strain.

The temperature effect seen during the Virginia Tech Mach 4 pure shear case was undesirable. This phenomenon is partially attributed to the long transient period experienced for tunnel start. In fact, it is possible that the CF2 configuration would have worked successfully in the short duration testing of the LENS facility. For example, the CF2 first order time constant was about 0.34 s, whereas a LENS test window might be 5 ms. Unfortunately, the CF2 gage leaked. This combined with the desire to attack the thermal issue led directly to a complete gage redesign.

The need to develop an encompassing design methodology first required the selection of tools for gage characterization. This objective was met through the careful examination of all sources of strain and dynamic response characteristics. As a test of the modeling techniques chosen, each of the four gages CF1-CF4 was carefully characterized. This also allowed us to compare the gage performance to the nominal conditions first proposed in Table 1-4. For convenience, the expected strain output is presented again in Figure 7-1. This shows that despite possible sources of apparent

strain, shear output dominates the signal for the CF2 through CF4 cases. Uniform wall pressure is not even a factor for these three gages. As shown during gage characterization, each of the other possible sources of apparent strain provide less than 10% of the overall signal output. Additionally, all of the gages have sufficient dynamic response to settle within the 10 ms steady load condition.

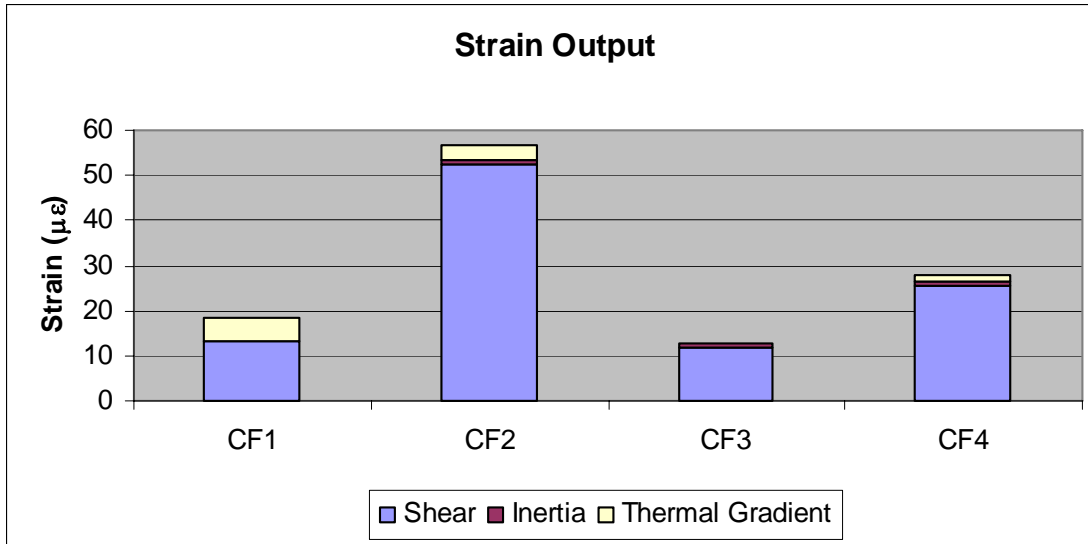
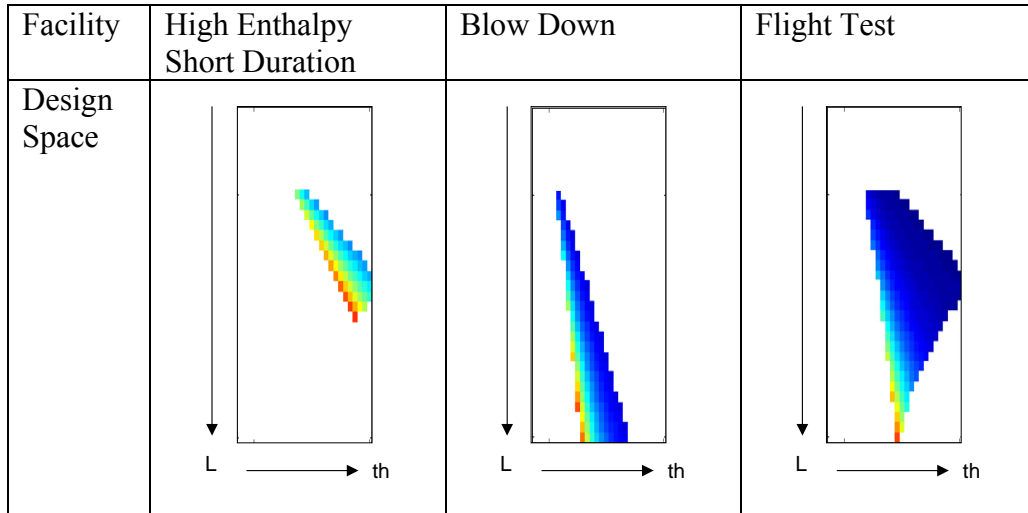


Figure 7-1. Expected strain output due to nominal load conditions.

With the needed modeling tools to accurately predict gage performance in hand, an optimization method could be developed. This objective was successfully met by constraining the design space, virtually building and testing potential gages, and comparing them to facility constraints. This process targeted three specific test environments and considered all of the physics expected in such tests. Direct skin friction gage design is no longer a matter of just balancing strain output with vibration frequency while considering inertial and temperature effects. It is now a full optimization of expected physical load conditions against desired output. This optimization aspect of the research may prove the most beneficial for future work. It condenses the design process to a set of state and design variables that can be specified for a particular test environment. This combined with the use of oil-filled bellows greatly constrains the design process and allows for a relatively quick turn around from test condition specification to gage design.

The impact of facility specification on design is clearly apparent in Table 7-1. This table shows the design space using INVAR for three very different test conditions. The high-enthalpy, short-duration facility is the most constrained, ignoring heat flux. Additionally, we see that for the blow down facility we can actually consider longer beam designs.

Table 7-1. Optimized design space for INVAR gages.



From our optimization research we came up with four drivers for the short duration test condition: heat flux, minimum frequency, minimum shear output, and maximum acceleration. But let's look at how test time affects those variables. In a short duration test, we need quick settling time and even high heat flux has little effect. Conversely, in a longer test, even small heat fluxes tend to provide thermal strain issues. Figure 7-2 takes a second rough look at what happens to design space for two very dissimilar test conditions.

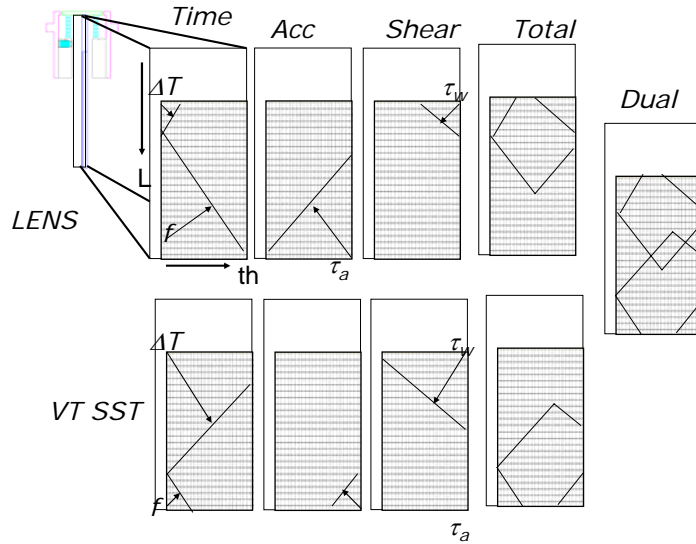


Figure 7-2. Design drivers and effective design space.

Our objective to design gages for application in LENS was met through the optimization process outlined in Chapter 5. Additionally, we have seen the expected output from these gages through Gage Characterization. Although these gages are currently in fabrication, the virtual testing by computation methods has shown they should meet all of the constraints expected at LENS.

The final objective was met through the multiple simulations presented in Chapter 6. This thorough investigation looked at dynamic response, thermal response, and instrumentation effects. Through these investigations we commented on possible sources of error. Additionally, we were able to perform virtual tests and look at expected gages response and instrumentation output.

7.1 Short-term recommendations

The design optimization section provided an INVAR and aluminum solution to the expected load conditions for a specific LENS test. These gages, CF3 and CF4 respectively, are currently being fabricated. In total, 4 INVAR CF3 and 6 aluminum CF4 gages will be built. This allows for several different strain gage configurations for each. The quantity and type of configuration being built is shown in Table 7-2.

Table 7-2. Gages currently being fabricated.

Gage Type	Quantity	Strain Gage	Bridge Type
CF3	2	EA-00-031CE-350	2 Half
CF3	1	EA-00-15LA-120	2 Full
CF3	1	EA-00-050-AH-350	2 Full
CF4	2	EA-13-031CE-350	2 Half
CF4	2	EA-13-015LA-120	2 Full
CF4 3-D	2	TBD	4 TBD

The different configurations are being built to test the thermal compensation proposed in the theoretical development. The half-bridge configurations work like the previous CF2 gage. The full-bridge configurations are intended to provide thermal compensation for an axially varying heat flux. Because the smallest available strain gages have lower resistance, a slightly larger gage is also being used in a full bridge configuration. This allows the comparison between the 120 Ω and the 350 Ω full bridges.

Though these gages have been designed to work in the LENS facility, validation testing will be conducted in the Virginia Tech supersonic tunnel. The test results using several configurations should verify if an axially varying heat flux is a source of apparent strain. The tests should also show if a full-bridge configuration can provide thermal compensation. Additionally, the testing should show whether a smaller resistance strain gage can provide the desired output.

The expectation is that the INVAR CF3 gages will perform better in the Virginia Tech facility due to thermal characteristics and low inertia. Depending on the accelerations in the LENS facility, the CF4 gages may actually perform better due to the lower weight. Also depending on the best performing CF4 configuration, two additional fully 3-D gages can be built.

7.2 Mid-term recommendations

The CF4 aluminum gage design provides a unique opportunity for additional strain gage configuration. Because the beam is of square cross section, a full 3-D shear measurement can be made. This would merely require the application of the desired

strain gage configuration on the opposing beam face. This is the intention of the last set of CF4 gages presented in Table 7-2.

7.3 Long-term recommendations

There are myriad approaches to attempting skin friction measurements. The long-term recommendations in this section provide incremental approaches using the gage-type developed through this research. The cantilever beam type direct measure gage cannot completely eliminate the effects of thermal gradient or inertia, at least not using strain gages. It is possible that with fiber-optic technology temperature effects could be eliminated. The inertial effects though small can also be greatly reduced for a cantilever beam type.

The thermal issue is important to consider since it cannot be avoided. This is an especially important consideration for flight testing where heat flux acts over long periods of time prior to measurement. Research using fiber optic measure of displacement might provide a suitable alternative to strain gages.

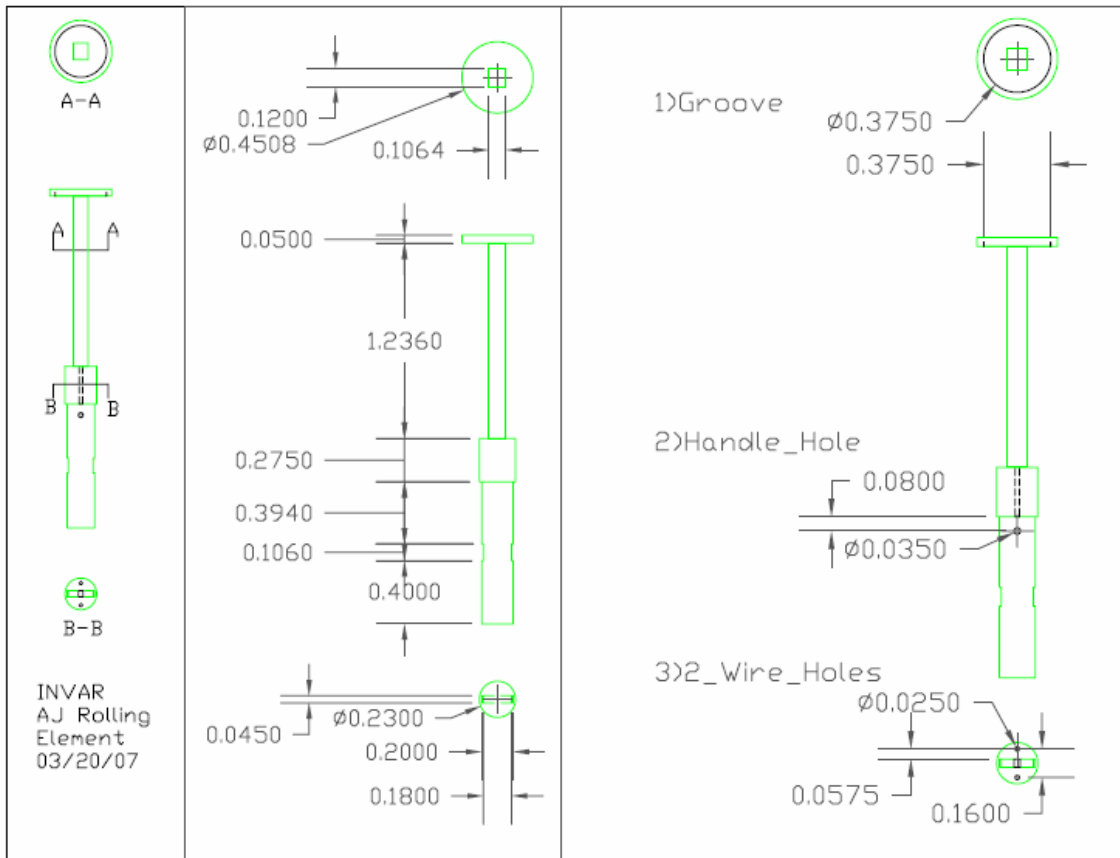
The evolution in size from the CF1 through the CF4 gages was driven partially by choosing the FC-8-L bellows. It is possible to return to a smaller bellows like the FC-3 in a new lightweight design. Though the assembly process would be more complicated, the reduction in weight would be significant.

References

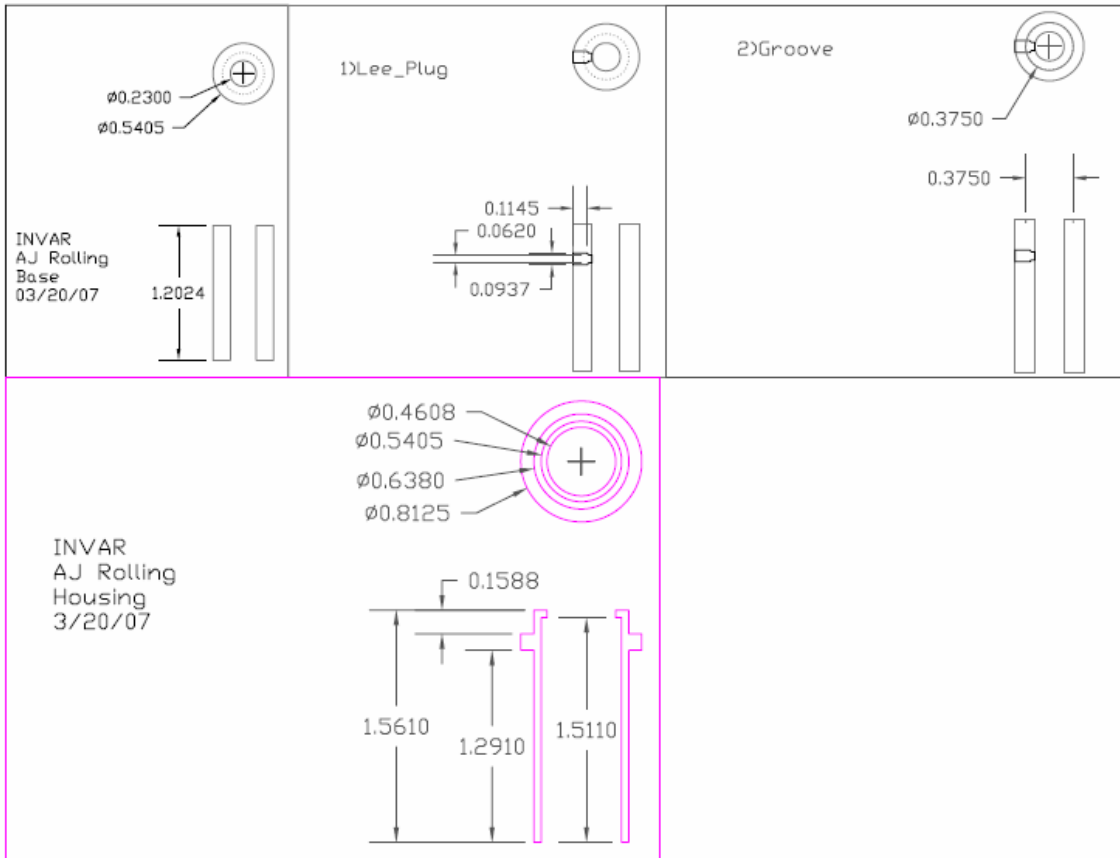
-
- ¹ Anderson, John D. Jr. Introduction to Flight, 3rd Edition. McGraw-Hill, Inc., New York, 1989, p. 6.
- ² Anderson, John D. Jr. Fundamentals of Aerodynamics, 2nd Edition. McGraw-Hill, Inc., New York, 1991, p. 16.
- ³ Van Wie, David M. and Ashish Nedungadi, "Plasma Aerodynamic Flow Control for Hypersonic Inlets", 40th AIAA Joint Propulsion Conference, AIAA 2004-4129.
- ⁴ Heiser, William H. and David T. Pratt, Hypersonic Airbreathing Propulsion. American Institute of Aeronautics and Astronautics, Inc., Washington, DC, 1994 p. 220.
- ⁵ Mattingly, Jack D., Elements of Gas Turbine Propulsion. McGraw-Hill, Inc. New York, 1996, pp. 372-378.
- ⁶ Heiser, pp. 173-192..
- ⁷ http://ipp.nasa.gov/innovation/Innovation_81/aex43.html
- ⁸ Heiser, pp. 173-192.
- ⁹ Heiser, p 189.
- ¹⁰ Schetz, Joseph A. Boundary Layer Analysis. Prentice Hall, Inc., Upper Saddle River, New Jersey, 1993, pp. 420-426.
- ¹¹ Schlichting, Hermann and Klaus Gersten, Boundary-Layer Theory 8th Edition. Springer, New York 2000, p. 620.
- ¹² Heiser, p. 487.
- ¹³ Holden, M.S. and R.P. Parker, "LENS Hypervelocity Tunnels and Application to Vehicle Testing at Duplicated Flight Conditions," Chp 4 of *Advanced Hypersonic Test Facilities*. Lu, F.K. and D.E. Marren Ed. AIAA Progress in Astronautics and Aeronautics Series: Vol 198. Chapter 4. Reston VA: American Institute of Aeronautics and Astronautics, 2002.
- ¹⁴ Heiser, p. 485.
- ¹⁵ Orr, Matthew W. Design, Analysis and Initial Testing of a Fiber-Optic Shear Gage for 3-D, High-Temperature Flows, Virginia Polytechnic Institute and State University, Dissertation 2004 pp. 1/9-1/13.
- ¹⁶ John, James A. Gas Dynamics 2nd Edition. Prentice Hall, Upper Saddle River, NJ, 1984, pp. 131-132.
- ¹⁷ Fogiel, M. The Strength of Materials & Mechanics of Solids Problem Solver. Research and Education Association, Piscataway, New Jersey, 1996, p. 1112.
- ¹⁸ Murray, William M. The Bonded Electrical Resistance Strain Gage. Oxford University Press, New York, 1992, p. 26.
- ¹⁹ Murray, p. 164.
- ²⁰ Hallauer, W.L., personal interview, May 2005.

-
- ²¹ Hallauer, W.L., personal interview, September 2005.
- ²² <http://www.aoe.vt.edu>
- ²³ <http://www.matweb.com/search/SearchSubcat.asp>
- ²⁴ <http://www.matweb.com/search/SearchSubcat.asp>
- ²⁵ Fogiel, pp. 1109-1112.
- ²⁶ <http://www.servometer.com/>
- ²⁷ <http://www.vishay.com/strain-gages/>
- ²⁸ Pilkey, p. 520-521.
- ²⁹ <http://www.ansys.com/>
- ³⁰ Figliola, p. 87-91.
- ³¹ Pilkey, p. 564.
- ³² Fogiel, p. 1112.
- ³³ Hibbeler, R.C. Engineering Mechanics Static and Dynamics 5th Edition. Macmillan Publishing Company, Inc., New York, 1989 pp. 486, 511.
- ³⁴ Hibbeler, pp. 486, 511.
- ³⁵ Figliola, p. 89.
- ³⁶ Fogiel, p. 258.
- ³⁷ Vishay Micro-Measurements, Precision Strain Gages Catalog 500. Vishay Micro-Measurements, Raleigh NC 2004, p. 15.
- ³⁸ Murray, p. 185.
- ³⁹ Hallauer, W.L., personal interview, September 2005.
- ⁴⁰ Fogiel, M. Heat Transfer Problem Solver. Research and Education Association, New Jersey, 1999, p. 211.
- ⁴¹ Hoffman, Klaus A. and Steve T. Chiang. Computational Fluid Dynamics Volume II 4th Edition. Engineering Education System, Wichita, 2000, pp. 4-9.
- ⁴² Fogiel, M. Heat Transfer Problem Solver. p. 216.
- ⁴³ Bezuidenhout, J.J. and J.A. Schetz, "Heat flux determination using surface and backface temperature histories and inverse methods," AIAA 2001-3530, 37th AIAA/ASME/SAI/ASEE Joint Propulsion Conference & Exhibit, 8-11 July 2001 Salt Lake City, Utah, p. 3.

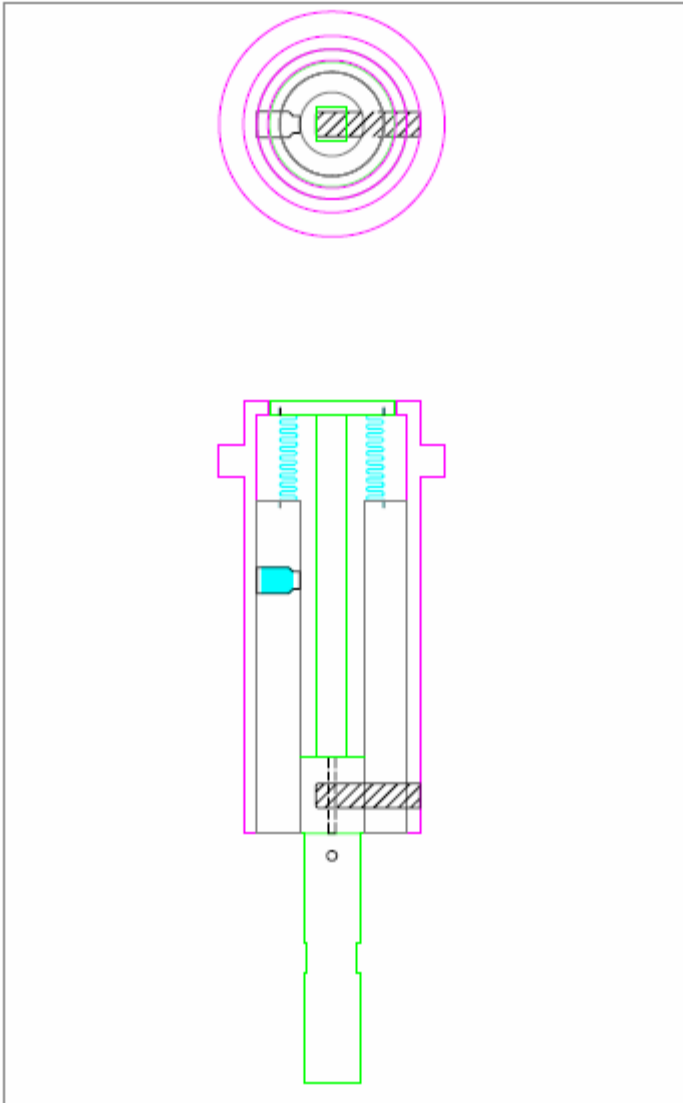
Appendix A Drawings



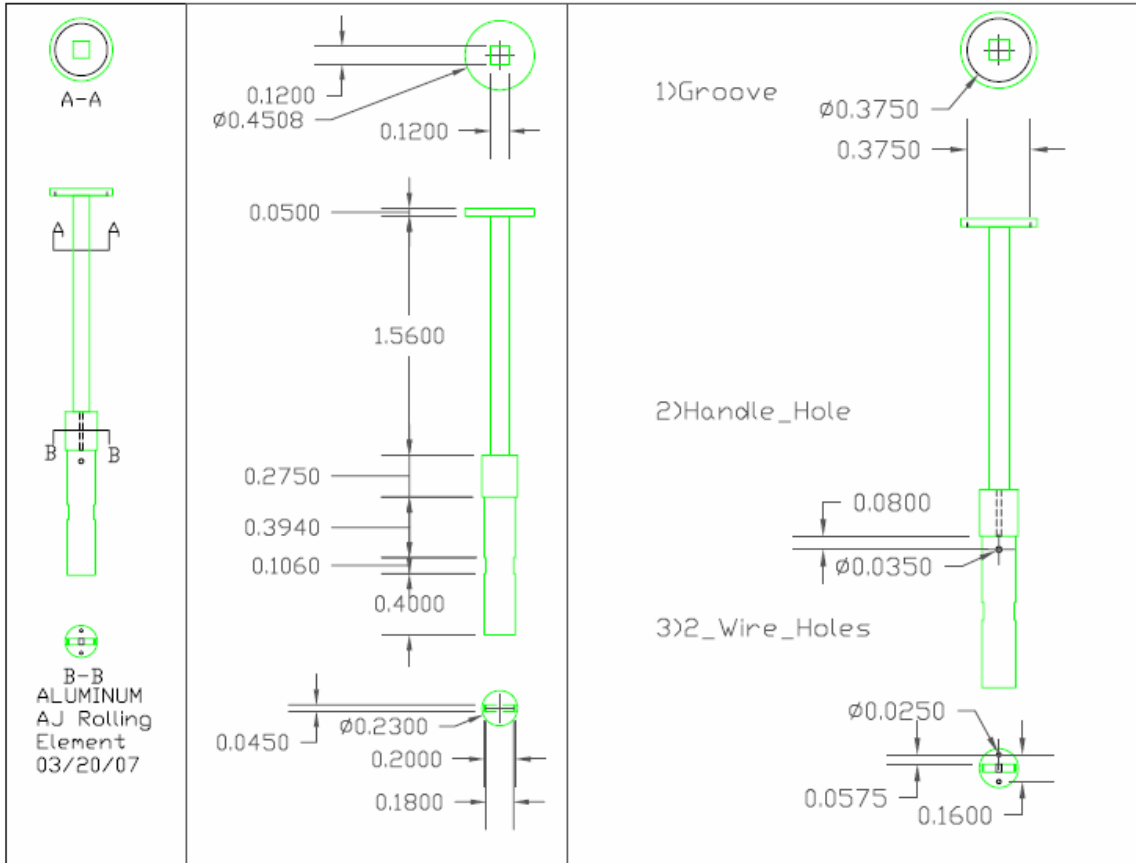
Drawing 1. CF3 element.



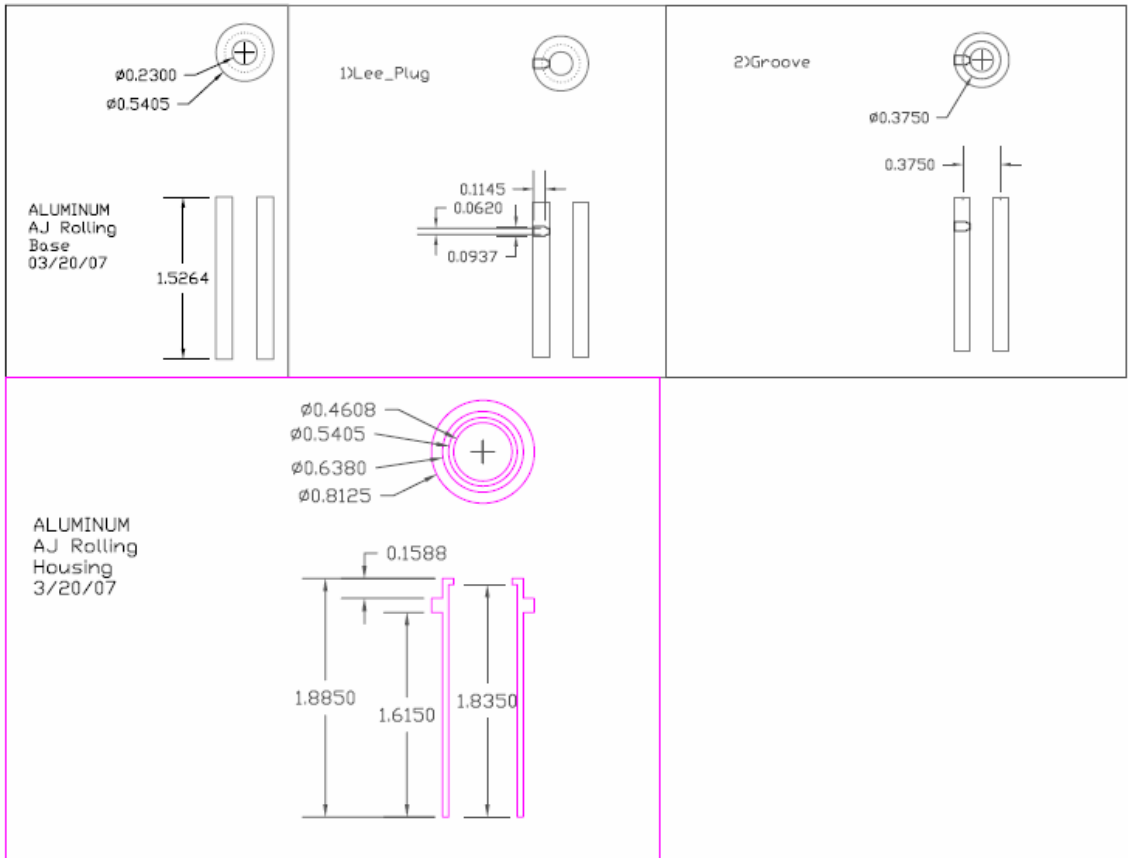
Drawing 2. CF3 base and housing.



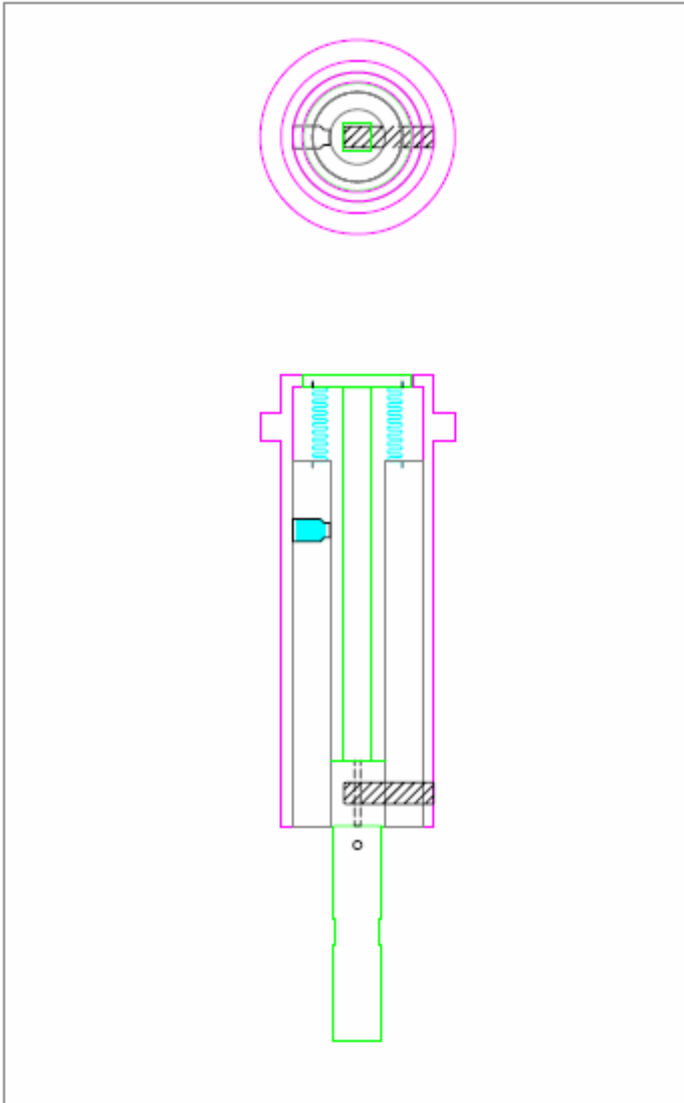
Drawing 3. CF3 assembled.



Drawing 4. CF4 element.



Drawing 5. CF4 base and housing



Drawing 6. CF4 assembled.

Vita

The author was born 4 May 1973 in Denver Colorado. He graduated from West Point and was commissioned into the Air Force June 1995. Over the next 10 years, he worked as an engineer on F-16's and C-17's and was the Air Weapon branch chief at the National Air and Space Intelligence Center. During this time, he also served 1 tour as Operations Officer for the Air Force Tops in Blue, playing keyboard for audiences in over 25 countries.. In 1999 he married Margaret and they had their first daughter Misty on August 15th. In May 2002, he earned a Master of Science in Aeronautical Engineering from the Air Force Institute of Technology. On June 4, 2007 his wife had their second child, Alison. Three days later, the author defended his dissertation in partial completion of the requirements for Doctorate in Aerospace Engineer from Virginia Tech. His next assignment is to teach Aeronautical Engineering at the United States Air Force Academy.